Alma Mater Studiorum · University of Bologna

School of Science
Department of Physics and Astronomy
Master Degree in Physics

Study of first thin LGAD prototypes for the ALICE 3 timing layers

Supervisor:
Prof. Andrea Alici

Co-supervisor:
Dr. Francesca Carnesecchi

Submitted by:
Sofia Strazzi

Academic Year 2020/2021

Abstract

The work here presented concerns the characterization and the performance study of very thin Low-Gain Avalanche Detector (LGAD) prototypes; the goal is to evaluate if such a sensor is suitable for the Time-Of-Flight (TOF) system of the ALICE 3 experiment, a next generation heavy ion experiment (LHC Run 5). A total of 18 sensors with a thickness of 25 μm and 35 μm were characterized; both single channel and matrices, with different inter-pad design and doping profile were compared to two 50 μm-prototypes. Preliminary tests with a laser setup allowed to evaluate the light-sensitive areas in terms of efficiency, uniformity of the response and edge effects. Finally, timing performances were analyzed. Promising results were found for the 25 μm-thick sensors, which showed a time resolution better than 16 ps for a gain 20 and reaching nearly 13 ps for a gain 30.

Contents

Introduction

The ALICE Collaboration has submitted the proposal of a next-generation heavy-ion experiment at the LHC as a follow-up to the present ALICE experiment, to be installed during the LHC Long Shutdown 4 ($\sim$ 2031), with the goal to provide excellent electron identification and secondary vertex finding, as well as reconstruction efficiency down to extremely low momenta and to collect data samples that are at least a factor 50 larger than those from Run 3 and 4 [3]. The experimental apparatus would consists of truly cylindrical layers based on curved wafer-scale ultra-thin silicon sensors with Monolithic Active Pixel Sensors (MAPS) technology, featuring an unprecedented low material budget of 0.05% X_0 per layer, with the innermost layers possibly positioned inside the beam-pipe. Besides excellent tracking and vertexing capabilities, the Particle Identification (PID) with silicon-based detectors for TOF measurements is of fundamental importance to achieve the expected physical goals; the compact size of the experiment and the need to provide electron-charged hadron separation up to momenta of the order of few hundreds of MeV/c imposes very stringent requirements to the TOF layers (called timing layers in the ALICE 3 nomenclature), including a time resolution of about 20 ps.

The LGAD (or UFSD) is a new kind of avalanche silicon detector optimized for timing. It has been proven that LGAD with a thickness of 50 μm combined with a gain G = 20-30 provides excellent performances, with a time resolution around 30 ps. At the moment this is indeed the best candidate for the ALICE 3 timing layer.

In this thesis, the characterization of the first very thin LGAD prototypes produced by the Fondazione Bruno Kessler (FBK, Italy) is reported. These prototypes have a sensor thickness of 25 μm and 35 μm and differ in terms of several characteristics like size and geometry. These measurements, performed initially also on the bare silicon, using a probe station at the INFN laboratories in Bologna, include the measurement of the Current-Voltage (I-V) curves, which are used to select the optimal working voltage and evaluate the different inter-pad configuration, and the Capacitance-Voltage (C-V) curves that allow to extract the gain layer and the full depletion voltages.

The characterization was done also on two 50 μm-thick prototypes in order to have a comparison with the thinner ones.

Following the characterization, preliminary studies were performed thanks to a laser

setup; the aim was to evaluate the uniformity of the light sensitive areas and the edge effects. Finally, the time resolution was studied with light conditions that simulates the passage of minimum ionizing particles.

Chapter 1

ALICE 3: a next-generation LHC heavy-ion experiment

ALICE (A Large Ion Collider Experiment) [1] is the experiment at the CERN Large Hadron Collider (LHC) designed to study the physics of strongly interacting matter at extreme energy densities and temperature, where a phase of matter called Quark-Gluon Plasma (QGP) forms. The experiment exploits collisions between heavy ions and protons delivered by the LHC. In particular, with ultra relativistic heavy-ion collisions it is possible to recreate conditions similar to those of the early universe.

Already during the LHC Run 1 (2009 - 2013) and Run 2 (2015 - 2018), ALICE was able to pursue a rich program of QCD physics with precision measurements, allowing a better understanding of the QGP properties and the discoveries of new phenomena, such as the evolution of strangeness enhancement from low-multiplicity pp to high-multiplicity Pb-Pb events, or the regeneration mechanism of the J/Ψ by formation via coalescence of independently produced charm and anti-charm quarks.

In order to fully exploit the scientific potential of the LHC upgrade scheduled for the Long Shutdown 2 (LS2), major upgrades of the detectors are currently undergoing, combined with a new continuous readout, in order to allow the experiment to cope with the high interaction rates foreseen for the forthcoming Run 3 and Run 4, in which the integrated luminosity for Pb-Pb will arrive to $\sim 13\,\mathrm{nb}^{-1}$ [2]. They comprise the new Inner Tracking System (ITS3) and Muon Forward Tracker, both based on Monolithic Active Pixel Sensors, new GEM-based readout chambers for the Time Projection Chamber (TPC), and the new Fast Interaction Trigger detectors.

In parallel to the installation and commissioning of the upgraded systems, preparations for further detector upgrades in the next Long Shutdown (2025 - 2027) are ongoing and R&D programs for the future detectors have already started.

The improvement of the ALICE detector will enable to tackle several key measurements in the context of heavy-ions collisions, concerning the production of multi-charmed

	$^{16}O^{8+}$	$^{40}Ar^{18+}$	$^{40}Ca^{20+}$	$^{78}Kr^{36+}$	$^{129}Xe^{54+}$	$^{208}Pb^{82+}$
$\langle L_{AA} \rangle$ cm^{-2}s^{-1}	4.54×10^{31}	2.45×10^{30}	1.69×10^{30}	1.68×10^{29}	2.95×10^{28}	3.8×10^{27}
$\langle L_{NN} \rangle$ cm^{-2}s^{-1}	1.16×10^{34}	3.93×10^{33}	2.71×10^{33}	1.02×10^{33}	4.91×10^{32}	1.64×10^{32}

Table 1.1: Instantaneous luminosities for different nuclei.

baryon, elliptic flow of electron-positron pairs and photon production at very low momentum, but the wide range capabilities of the upgraded apparatus still leave open physics questions to be addressed.

A promising opportunity to extend the heavy-ion programme is the large increase in nucleon–nucleon luminosity at the LHC after LS4, reached by colliding intermediate-mass nuclei as, for example, Ar–Ar or Kr–Kr (the istantaneous luminosities L_{NN} values are reported in table 1.1), that will give access to novel probes of the QGP and will open a precision era for probes which are still rare with the Pb–Pb system. Such luminosities would saturate the maximum interaction rate achievable to operate the current ALICE experiment, whose tracking is based on a large Time-Projection Chamber (TPC) detector. For this reason, the present TPC has to be replaced with new faster technologies.

In order to be able to profit of this kind of interaction rates, a compact next-generation heavy-ion experiment, ALICE 3 [3], has been proposed to be installed at the LHC Interaction Point 2 during the LHC Long Shutdown 4 (LS4), which will start around 2031, as shown in figure 1.1. It will be an all-silicon detector, based on technological advances of novel silicon technologies, with unprecedented low mass, that would allow reaching down to an ultra-soft region of phase space, to measure the production of very-low transverse momentum lepton pairs, photons and hadrons at the LHC.

1.1 Physics goals

ALICE 3, with its ability to measure the production of leptons, photons and identified hadrons down to p_T scales of the order of a few tens of MeV/c, would provide significant advances in several areas, enabling a rich physics program, ranging from measurements with electromagnetic probes at ultra-low transverse momenta to precision physics in the charm and beauty sector.

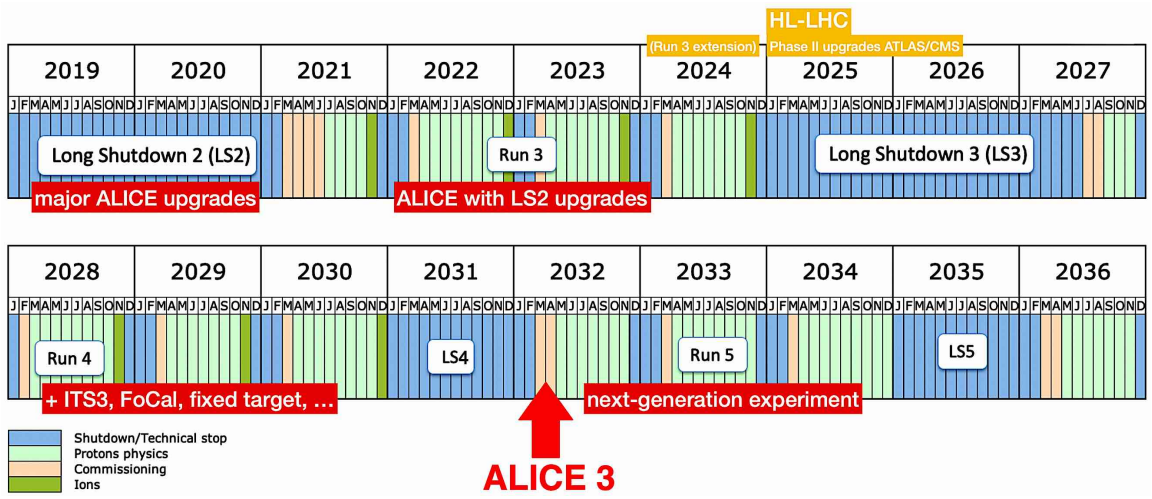

Figure 1.1: LHC schedule with the main foreseen upgrades. The red arrow indicates the scheduled ALICE 3 installation.

1.1.1 Heavy flavour and quarkonia: hadronization in high-density QCD systems

One of the most interesting physics topics that will be addressed by ALICE 3 concerns the Heavy Flavour (HF) measurements. The unique tracking and vertexing capabilities of the proposed apparatus, together with the high-luminosity provided by LHC after LS4, will open a new precision era for measurements of the production of open and hidden heavy flavour particles in nuclear collisions that will make it possible to quantify the properties of the QGP with heavy-flavour probes.

HF production in heavy-ion collisions provides a unique tool to investigate the mechanisms of in-medium energy loss and hadronization of heavy quarks from the QGP. In this respect, they are so essential because, due to their large masses, charm and beauty quarks are produced in hard scattering processes occurring in the early stages of heavy-ion collisions, with high transfer momentum, and cannot be created by inelastic scattering in the first hadronic phases. They subsequently traverse the QGP medium and in the view of the pQCD-based models, interact with its constituents via inelastic (gluon radiation) and elastic (or collisional) processes. These interactions may lead to the thermalization of low-momentum heavy quarks, which would thus take part in the expansion and hadronization of the medium. For these reasons, HF hadrons provide direct information on all stages of the system evolution [4, 5].

One of the main observables used to study the medium effects on HF hadron production is the nuclear modification factor (R_{AA}), defined as the ratio of the Pb–Pb yield to the pp cross-section scaled by the nuclear overlap function. While radiative interactions

only lead to energy loss, collisional ones can also result in an increase of the heavy-quark momentum. At high p_T, the nuclear modification factor is sensitive to the medium-induced radiative energy loss of heavy quarks via gluon emission. Precise measurements of the R_{AA} thus provide insights on the momentum dependence of heavy quark energy loss, and in particular on the suppression of high-p_T HF hadrons in nucleon-nucleon (AA) collisions with respect to pp collisions, but also provide important tests of QCD predictions regarding the expected flavour and mass dependence of the energy loss processes: in this regime a hierarchy in the energy loss is expected with higher-mass quarks loosing less energy with respect to lower-mass quarks. At low p_T, on the contrary the production rate of heavy-flavour mesons in heavy-ion collisions is dominated by the elastic energy loss by collisional processes of the heavy quarks in medium that diffuse with a brownian motion inside the QGP and the recombination of the heavy quark with light quarks at the hadronization stage. To access the properties of QGP at different scales is thus mandatory to be able to do measurements down to very low p_T.

The new detectors system will in addition be able to tackle another important topic, especially in light of recent measurements both in AA and pp collisions: HF hadronization. The hadronization mechanisms belong to the non-perturbative domain of QCD and a first-principle description of these processes is still missing, for both light and heavy flavours. In particular, in nucleon-nucleon collisions other hadronization mechanisms for the production of heavy-flavour hadrons, in addition to the fragmentation via single-string breaking, are presents and the main one is coalescence (also denoted as recombination). Fragmentation is one of the most common approaches for the calculation of inclusive hadron production and it is especially applied to high-momentum partons emerging from initial hard processes, where high-momentum quarks fragment directly and independently into high-momentum hadrons. On the other hand, coalescence is expected to dominate in the low-momentum regime in nucleus–nucleus collisions, where partons are abundant and heavy quarks can hadronize by recombination with light quarks [6]. In particular, hadronization via coalescence leads to a modification of the relative abundance of the heavy-flavour hadron species produced. The most striking effect is an enhancement of the baryon-to-meson ratios for heavy-flavour hadrons.

Recent measurements of Λ_c/D^0 ratio at the LHC indicate that fragmentation may not be sufficient to describe charm quark hadronization at low momentum in pp and p–Pb collisions, at least for what concerns baryon production [7, 8]. This value is also much larger than the prediction of the statistical hadronization model [9], in which the hadronization occurs by recombination of an equilibrated system of quarks and the hadron abundances are mainly determined by their masses. Since other mechanisms considered are expected to be important at low-intermediate p_T, the possibility to reach very low momentum measurements, given by the new apparatus, is of essential importance. In fact, to explain these experimental data, different models have been introduced including, for example, new topologies (like junctions) connecting quarks created

in different Multi-Parton Interaction (MPI) systems, or production with feed-down contribution from yet-unobserved charm-baryon states. At the moment Λ_c measurements are presently in agreement with more than one, and doesn't allow to validate or reject some of them.

Multi-charm baryons represent a tool that would allow pushing the sensitivity to hadronizations mechanism in order to provide more experimental constraints to models. In fact, multi-charm states production in same hard-scattering is very rare, so they can considered as "pure" coalescence particles and their production is expected to be highly enhanced with respect to pp collisions. Enhancement is expected by as much as a factor 10^2 for the recently discovered Ξ_{cc} baryon [10] and even by as much as a factor 10^3 for the as yet undiscovered Ω_{ccc} baryon [11]. The measurements allowed by ALICE 3 would open a crucial new window on hadron formation from deconfined matter, and impressive results on the reconstruction of complex cascades of weak decays, achievable only thanks to the capabilities of this apparatus and luminosities of the order of 1 fb^{-1} [12], would be in general expected for Multiply Heavy Flavoured (MHF) baryons. The precise quantification of their production enhancement in AA collisions w.r.t. pp ones, will allow for the first time the test of the coalescence and statistical hadronization models for this kind of particles, providing a key confirmation of the current interpretation of the LHC quarkonium results and offering additional knowledge on the properties of QGP.

The proposed detector would also significantly enhance the capability for quarkonium physics.

A remarkable discovery from Pb-Pb collisions at the LHC was the significantly reduced suppression of J/Ψ in comparison to lower energies [13] and that this reduction is much higher at low p_T [14]. These measurements are compatible with predictions of the presence of a significant contribution from a novel mechanism for quarkonium production called regeneration [15]. Alternatively, a mechanism of continuous creation and destruction of charmonia in the QGP was proposed at the phase boundary of QCD [16].

Disentangling the contributions of prompt J/Ψ, in particular the one originating from B decays and the production yields of low transverse momentum χ_c states, and non-prompt J/Ψ and considering path-length dependent energy loss is mandatory to understand the systematics of charmonium production. The separation of prompt charmonia from secondary one in the proposed apparatus will be excellent.

1.1.2 Low-mass dileptons: chiral symmetry restoration and temperature of QGP

While hadrons are produced mostly in the last, electromagnetic radiation is expected to be emitted during a significant part of its lifetime.

Photons and dileptons, i.e. lepton-antilepton pairs produced by internal conversion of virtual photons, are unique tools to study the space–time evolution of the hot and dense matter created in ultrarelativistic heavy-ion collisions. These electromagnetic probes are produced continuously by a variety of sources during the entire history of the QGP, they traverse the medium and couple directly to quarks, escaping the collision without being affected by the strong interaction, thus carrying undistorted information on their production source.

The different intervals of the dielectron invariant-mass spectrum are sensitive to different stages of the collision and their related physical processes. The nearly massless detector would allow pushing down transverse momentum very close to the natural scale determined by the inverse radius of the system (about 100 MeV/c in pp collisions and 10 MeV/c in Pb-Pb collisions), allowing an entirely new approach, based on a precision measurement of photons and thermal dileptons, providing a unique sensitivity to the early times of the deconfined system. The very low mass and p_T cutoff would allow to test theoretical predictions in the region of phase space, currently beyond reach, where most of the radiation is emitted.

This intermediate invariant mass region of the dielectron spectrum contains contributions from low-mass vector meson decays and thermal radiation from partonic and hadronic phases. In this mass range, the dielectron production is largely mediated by the ρ^0, ω and φ mesons. Among these, the ρ^0 is the most relevant source, due to its strong coupling to the $\pi^+\pi^-$ channel ($\pi^+\pi^- \rightarrow \rho^0 \rightarrow \gamma^* \rightarrow e^+e^-$). The study of the dielectron spectrum in Pb–Pb collisions, where higher energies are delivered, is interesting to further investigate the ρ^0 broadening effect near the phase transition connected to chiral symmetry restoration.

The expected dielectron mass distribution in heavy-ion collisions at the LHC is shown in figure 1.2. The solid black line shows the expected total dilepton mass spectrum. Two different processes are indicated in the plot: thermal production from both the plasma and from hadron gas and hadronic production via vector mesons. Since only the hadronic production channels are sensitive to chiral symmetry restoration, the comparison between this one and the production without medium effects, provides a crucial test for it in the hot and dense phase of the collision, for which no direct experimental evidence exists.

With the proposed nearly zero mass detector of ALICE 3, it is possible to make a very precise measurement of the thermal dilepton continuum, in the range that goes from the mass of the ρ meson to 1.6 GeV, in pp, p-Pb and Pb-Pb collisions. This will allow, for example, to test whether the minimum at 1.26 GeV, found in e^+e^- collisions, corresponding to the mass of the a_1 meson considered as the chiral partner the ρ fills in, going from minimum bias pp to central Pb-Pb collisions, testing chiral symmetry restoration in the $\rho - a_1$ sector.

Moreover, the study of the thermal dielectrons, thanks to the dramatic improvement of the apparatus will provide information also on the temperature of the system created

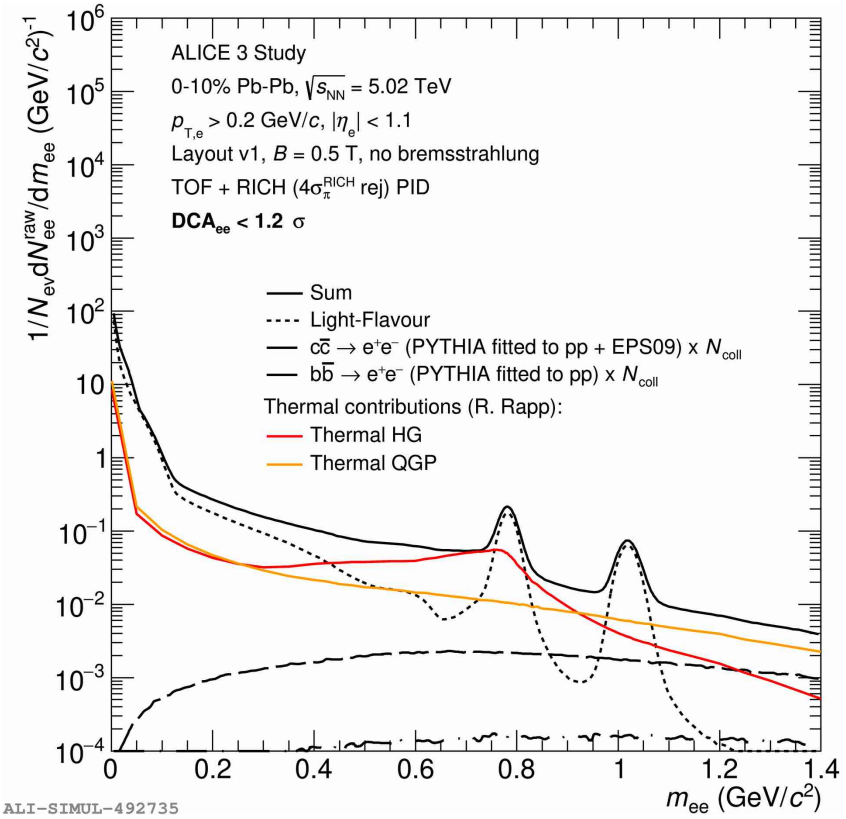

Figure 1.2: Expected raw dielectron yield after a maximum DCAee cut at 1.2 sigma as a function of the invariant mass for the TOF and RICH PID scenario in 0-10% Pb-Pb collisions with ALICE 3 Layout v1 setup and B = 0.5 T. The different contributions by thermal emission from the hadron gas (red line) and from the QGP (orange line) are shown separately and compared to the hadronic production. The solid black line shows the expected total dilepton mass spectrum

at an unprecedented precision in the 1.8 - 3 GeV region of the mass spectrum, offering a better understandings of its thermodynamic properties.

1.1.3 Soft and ultra-soft photons: Low's theorem

Photons are in general of particular interest to study the hot QCD medium, since, like the dileptons, they escape it without being affected, providing additional information. In particular, at low p_T values the direct photon spectrum is mainly fed by thermalization of the hadron gas following collisions and to a larger extent of the QGP expected in ultrarelativistic heavy-ion systems. The production of these thermal photons strongly depends on the hot medium properties, thus they carry information on its space expan-

sion and temperature, which are valuable to explore the hadron matter phase diagram.

In general, the study of real soft photons in the low-p_T region in a collider environment is really challenging due to the large contribution of background photons originating from hadron decays (mainly from π^0), from electron bremsstrahlung in the detector material and from ultraperipheral collisions. At the moment the measurements in heavy-ion collisions can only extend to 1 GeV [18].

The ultra-low mass tracker of ALICE 3, will extend the photon transverse momentum range into the region of 50 - 100 MeV/c, thereby allowing tests of current predictions for radiation from the QGP in completely uncharted regions of phase space. But the experiment will allow to push the boundaries at much lower p_T. A specifically designed, small spectrometer at forward rapidity in the range $3.5 < |\eta| < 5$, will reach the measurements in the range of 1 MeV/c $< p_T <$ 100 MeV/c.

The measurement of this very soft electromagnetic radiation in the p_T region below 100 MeV/c and approaching 1 MeV/c is of primary interest, in fact, a simple theory prediction based on very few assumptions is completely off. In quantum field theories, the production of these very low transverse momenta photons is linked to the charged final state through fundamental 'soft theorems' [19, 20]. In particular, according to the Low's theorem, it is possible to relate hadron momenta produced in a high energy collision to the number of soft photons produced. After the publication of the paper [21], the predictions from the resulting theorem have been repeatedly tested experimentally, but in most cases, significant discrepancies were found between predictions and experimental measurements, probably due to the difficultly of this measurement in this range.

The Low's theorem has now been intensively studied by many scientists derived in various ways. According to the predictions, the number of soft (real) photons actually diverges towards low p_T in a controlled manner that is central to the consistency of the underlying quantum field theory. It would be of primary importance to reach the experimental sensitivity to photons in this p_T region, in order to test these predictions or find any deviation in experimental results for soft photon spectrum that can indicate something fundamentally not understood.

1.2 Detector system

In order to achieve this experimental program, a nearly massless detector, tracking over a wide momentum range, with excellent decay vertex resolution, particle identification and high-speed capabilities, based on the technological advances for silicon pixel sensors, has been proposed. It would be installed during the LS4, at the IP2, where the ALICE experiment is currently installed. The detector has a very compact layout in both the radial and longitudinal dimensions and covers a pseudorapidity region of $|\eta| < 4$ over

the full azimuth.

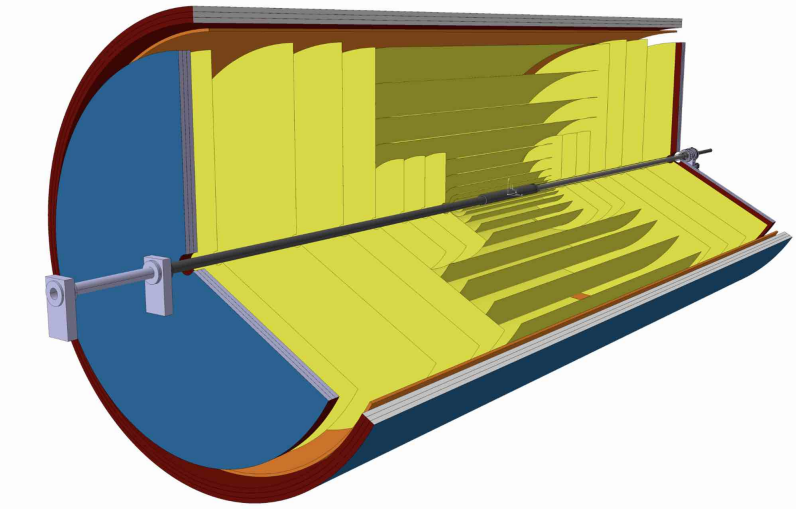

Figure 1.3: Representation of the experimental apparatus. The detector is embedded in a solenoid magnet (not shown in the figure). The central barrel, which covers the pseudorapidity region $|\eta| < 1.4$, is composed of the IT, inside the beampipe, the OT (yellow layers), the TOF (orange layer) and the SPD (outermost blue layers). Two endcaps, each consisting of a set of tracking disks and an SPD disk, extend the rapidity coverage to the region $|\eta| < 4$.

A schematic view of the experimental apparatus is represented in figure 1.3. It consists of a central barrel that covers the pseudorapidity region $|\eta| < 1.4$, composed of a Inner Tracker (IT), with 3 layers located inside the beam pipe, an Outer Tracker (OT), a Time-Of-Flight (TOF) detector and an electromagnetic Shower Pixel Detector (SPD) to identify low transverse momentum electrons and positrons down to a transverse momentum of about 500 MeV/c, completed by two endcaps, which extend the acceptance to the pseudorapidity region $1.4 < |\eta| < 4$, each of which containing 4 disks in the IT, 6 disks in the OT and one disk in the SPD. The system is embebbed in a solenoid magnet. The moderately weak solenoidal field (0.5 T) of the ALICE magnet seems adequate to meet the requirements. However, the option of a magnet with a larger magnetic field (1 T or larger) will also be considered.

1.2.1 Tracking System

The apparatus is centered on an ultra-low all-silicon tracker arranged in truly cylindrical layers in order to achieve the best possible impact parameter resolution for decay vertex reconstruction, combined with end-cap disks to cover a large pseudorapidity range. A possible configuration of the layers is shown in figure 1.4 (left).

The three innermost layers of the Inner Tracker made with curved wafer-scale ultra-thin Complementary Metal-Oxide-Silicon (CMOS) Monolithic Active Pixel Sensors (MAPS) technology, will be located inside the beam vacuum chamber, with the one closest to the interaction point positioned at only 5 mm radial distance from the beam line. This is possible thanks to the concept of the IRIS tracker, which allows the layers to be retracted from the nominal (physics) position during the injection of the beams into the LHC and at the end of every fill to protect them from possible damages caused by beam failures, keeping at the same time the surface of the vacuum chamber continuous and homogeneous to avoid perturbations on the beam particles' motion, as shown in figures 1.4 (right down). The central barrel is completed by four end-cap disks on each side.

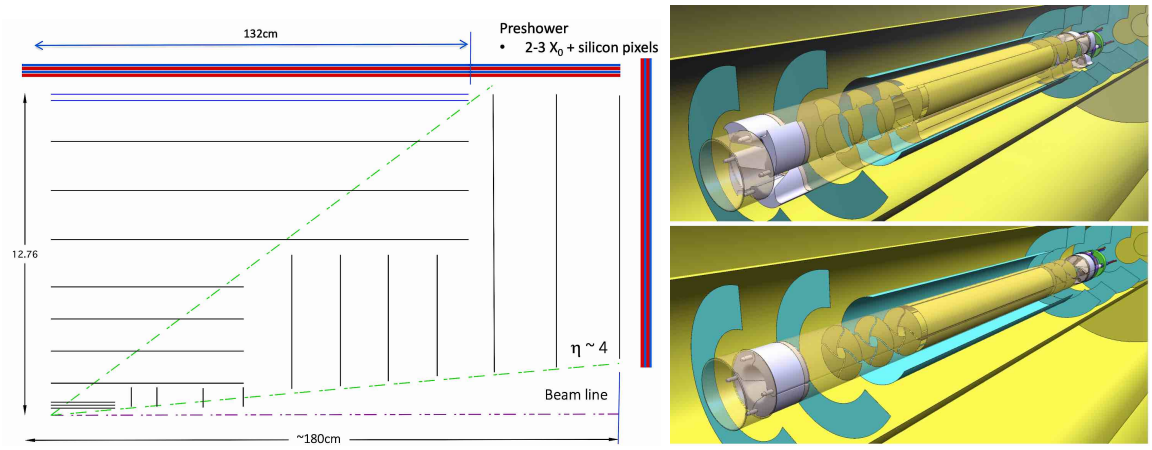

Figure 1.4: Left: possible configuration of the tracking system, with 12 layers. Right: 3 layers are situated inside the beam pipe thanks to the movable IRIS tracker, that can be opened (up) during the switch on of the accelerator and closed (down) during the operations.

Thanks also to the unprecedented low material budget of 0.05% X_0 per layer that it features and pixels of about 5 μm $\times$ 5 μm, this ultra low mass movable vertex tracker provides very impressive vertexing performance.

The tracking performances of the detector, taking into account multiple scattering, detector occupancy and deterministic energy loss, are really spectacular.

The most important one is the track impact parameter resolution, which defines the capability of a vertex detector to separate secondary vertices from the interaction vertex. It is defined as the dispersion of the distribution of the Distance of Closest Approach (DCA) of the reconstructed (primary) tracks to the interaction vertex.

A comparison of the impact-parameter resolution of ITS2, ITS3 and ALICE 3 tracking system, considering a magnetic field of 0.5 T, is shown in figure 1.5. As it can be seen, the resolution is improved by a factor 10 w.r.t. ITS3 performance. Thanks to

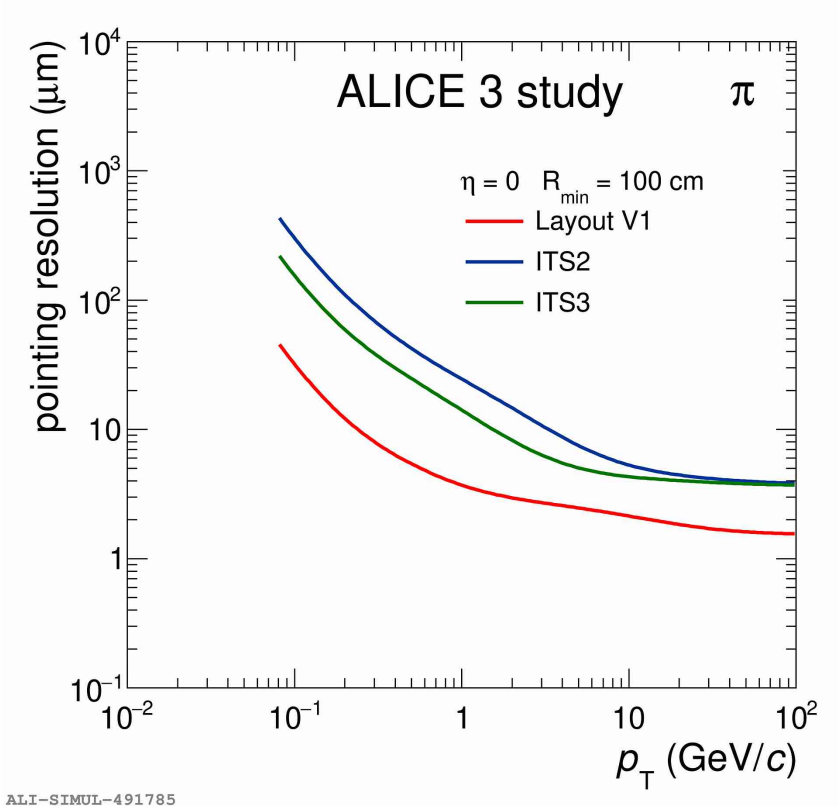

Figure 1.5: Pointing resolution for charged pions as a function of the transverse momentum for the IT of the ALICE 3 (layout V1) compared to the ITS2 and ITS3 expected values extracted with the same technique considering a magnetic field of 0.5 T. A minimum track length of 1 meter is requested.

the nearly zero mass, the detector can achieve resolutions of less than 10 μm down to $p_T \simeq 200$ MeV/c and remains below 100 μm down to $p_T \simeq 0.1$ GeV/c, as shown in figure 1.5.

The OT instead will be probably composed by a system of 9 barrel layers and 7 end-cap disks, with a much larger pixel size of about 30 μm $\times$ 30 μm, based on the same technology of the IT. For these outer layers the material budget will be about 0.5% X_0 and the spatial resolution will be 5 μm.

The improved vertex resolution will be beneficial for the measurement at low transverse momentum of many of the observables that ALICE 3 plans to measure. This kind of resolutions and the material budget of the proposed layout will, for example, significantly extend the physics capability for the study of heavy-flavour production.

1.2.2 Time-Of-Flight detector

The central tracker is surrounded by a silicon-based Time-Of-Flight (TOF) detector that provides particle identification, using one dedicated timing layer and time measurements in the tracking system. The proposed next-generation heavy-ion experiment at the LHC will be equipped with a 20 ps timing layer located at approximately 1 m from the beam line.

This 20 ps resolution is required to separate pions and electrons up to transverse momentum of $\sim$ 300 MeV/c, because of the 1 m radius and the magnetic field of B = 0.5 T. According to the TOF-PID technique, a better time resolution allows to separate electron and pions up to higher momenta, as shown in the plot in figure 1.6. As visible, a resolution of 20 ps grants a separation up to transverse momenta of $p_T \sim 750$ MeV/c. In order to keep the fake match probability <1% and e/π misidentification $<10^{-3}$, the pixel pitch of 5-6 mm is considered.

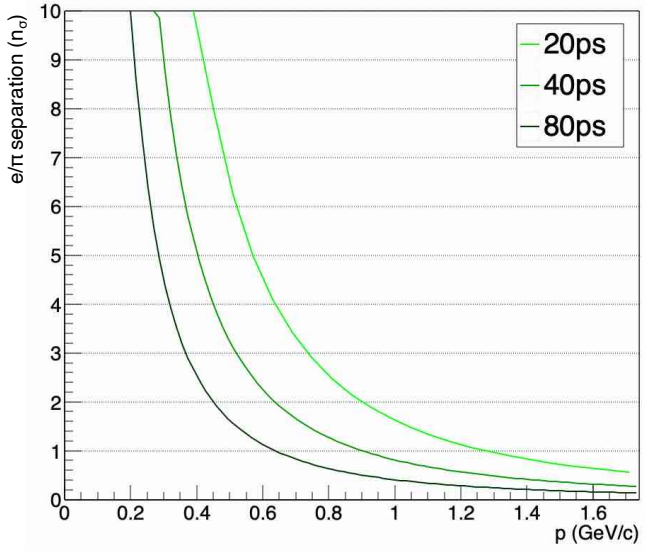

Figure 1.6: Electron and pion separation, expressed in number of standard deviations n_σ, as a function of the momentum, for three different resolutions of a TOF layer located at R = 1 m from the beam axis.

Furthermore, to extend the separation power towards low transverse momentum, down to $\sim$ 20 MeV/c, a second TOF layer, at a distance of 20 cm from the beam line, with a pixel pitch of 1 mm, is being considered.

Taking into account the relatively low radiation load expected on the timing layer of the new experiment and the requirements of 20 and 50 ps of resolution, respectively for the layers at 100 and 20 cm of distance, different new technologies are being explored:

Low Gain Avalanche Detector (LGAD), Silicon PhotonMultiplier (SiPM) or his based element SPAD (Single Photon Avalanche Detector) and MAPS.

1.2.2.1 TOF particle identification performances

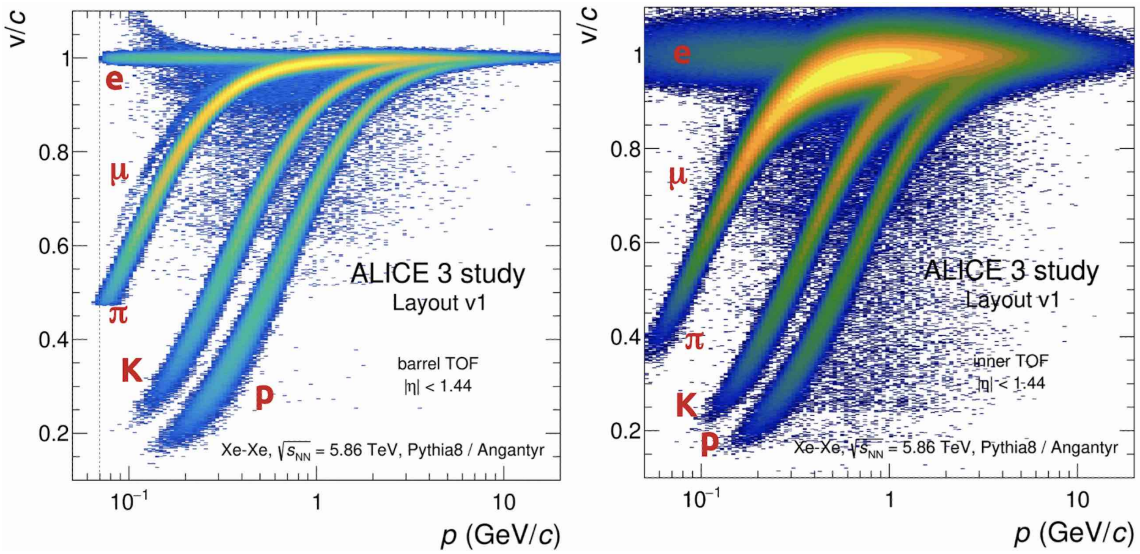

Figure 1.7: Simulated TOF response: measured particle velocity as a function of the reconstructed momentum with the timing layer placed at a distance of 1 m from the beam (left) and with the innermost layer (right) considering a magnetic field B of 0.5 T, Xe-Xe collisions with a center of mass energy equal to 5.86 TeV.

A preliminary analysis on the performances using a fast simulation Monte Carlo approach, taking into account the configuration and layout of the different detectors, including the material effects is already available, providing a reliable estimate on how the full system would perform.

In particular looking at the separation power in terms of the number of standard deviations n_σ, defined as

$$n_\sigma = \frac{\Delta t}{\sigma_{TOF}}$$

and considering a timing layer located at 1 m from the beam line with 20 ps of time resolution, it is possible to see from the figure 1.7 (left) at midrapidity ($\eta = 0$) that a separation power better than 3σ is provided up to $p_T = 750$ MeV/c for e/π, up to $p_T = 2.5$ GeV/c for K/π and up to $p_T \sim 4$ GeV/c for p/K.

1.2.2.2 Considered technologies

The development of precision timing detectors has always been of primary importance in improving the PID capability of particle physics experiments. One of the most promising development for the timing layers of ALICE 3 is represented by detectors based on CMOS technology. Their capability of integrating the sensing diode into the wafer hosting the front-end electronics, that can directly collect the signal, allows for higher sensitivity and reduced noise.

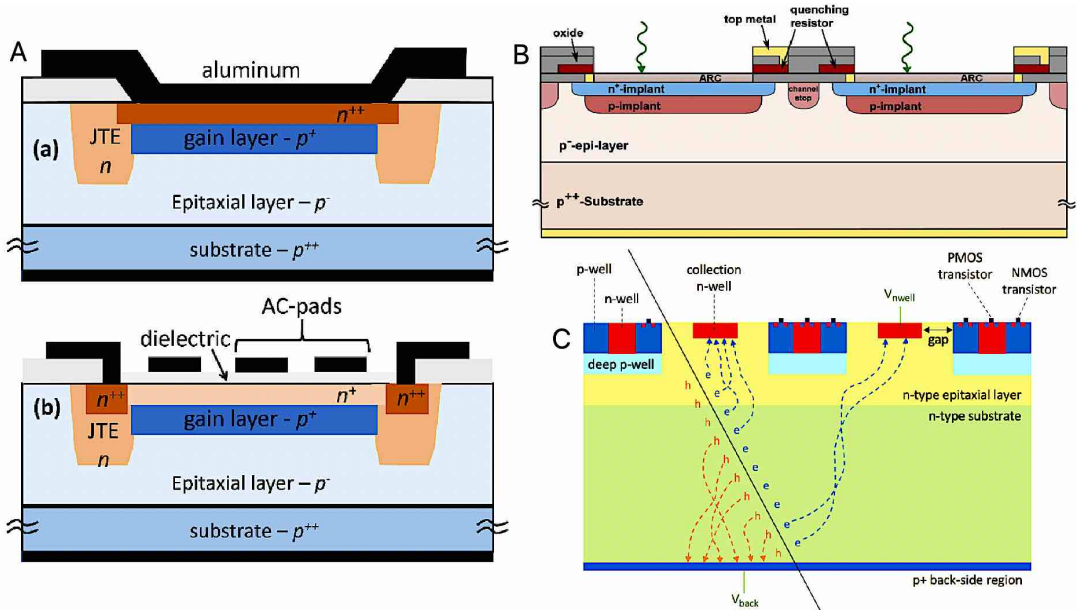

Figure 1.8: (A, a) Sketch of a section of a single-pad standard LGAD; (A, b)sketch of a section of a segmented AC-LGAD. (B) SiPM cross-section (n-on-p technology) showing the structure of the cells. The deep implant defines cell's active area. (C) Simplified structure of deep N-well MAPS.

They are suitable for the radiation environment expected in the experiment, due to the high resistivity substrate and in addition, the use of a CMOS commercial fabrication process, leads to their cost reduction and allows faster construction of large area detectors. In fact, this kind of option is becoming promising also outside the High Energy Physics (HEP) realm, revolutionizing, for example, the field of 3D imaging, which has become a key sensing technology in a wide range of LiDAR (Light Detection And Ranging) applications in the field of robotic, automotive, medical and spacecraft systems. Moreover, the application of CMOS sensors with high timing resolution in the medical field [22, 23] has attracted a growing interest in the last years. These applications has stimulated a huge effort in the development of dedicated sensors and associated

electronics by investigating different approaches.

To meet the requirement of high Signal-to-Noise Ratio (SNR), speed and spatial response uniformity, thin silicon sensors with a gain layer have been recently introduced. LGADs [see section 2.2], also known as Ultra Fast Silicon Detectors (UFSD), featuring a charge gain of 10-30, exhibit excellent timing performance, of 30-35 ps for 50 μm-thick sensors up to fluences of (1-2)10^{15} cm^{-2} [24]. To achieve a 100% fill factor, AC-LGADs, shown in figure 1.8 (A, b), characterized by a different signal formation, were introduced, with the benefit of an excellent space resolution, while maintaining a time resolution comparable to the traditional's one.

SPADs are then being studied, together with their integration in an array, i.e. the SiPM, shown in figure 1.8 (B). They can reach a time resolution of 30 ps for single photon measurement [25]. At the moment, there are no results for charged particles measurements, so it is necessary to investigate if they can reach such a resolution through a beam test. The weakness is the high primary and secondary noise.

Finally, a promising technology in terms of low material budget, high SNR, and limited diffusion of the charge carriers originated by the impinging particle, is a fully depleted MAPS, where the sensing layer and its readout are integrated in a single circuit, as shown in figure 1.8 (C), under development in the frame of the ARCADIA project. This kind of sensors is already present in the new ALICE Inner Tracking System [26], but the whole potentiality concerning the size of the active area, the power consumption and the timing capabilities is not yet reached [27]. At the moment the expected features have been experimentally confirmed for a pixel thickness between 25 and 300 μm [28] and the sensors show to be able to work in an environment with ionizing dose up to many thousands of Grays [29].

The proposed experiment can open extraordinary physics prospects in the scenario of heavy-ion collisions during LHC Run 5 and beyond. Comprehensive studies and simulations are being carried out in order to fully exploit the physics areas that this experiment could reach, also outside the topics examined before, and prepare the physics program for ALICE 3. In parallel, very intense R&D programs have started on the innovative technology options for the detectors, to demonstrate the feasibility.

Chapter 2

Solid state detectors

Solide state detectors, in particular the silicon based ones, have been used in HEP since about 25 years. They have been continuously improved to meet new requirements and challenges and, always based on a simple detection principle, many different types of silicon sensors have been developed, reaching spectacular performances that attracts the interest in many physics experiments and in a number of external applications. An introduction on semiconductor materials and on how the particles interact with them is reported in appendices A and B. In this chapter an overview of the basic properties of these detectors and their main features is presented with a focus on the time resolution, together with the description of a relatively new kind of silicon detector (Low Gain Avalanche Detector) and their main applications.

2.1 Silicon detectors for timing applications

The development of silicon detectors brought these devices to have a very good time resolution. Thanks to their features, they are being more and more used for timing applications, both inside and outside the HEP realm.

2.1.1 Time resolution

The basic elements used to perform time measurements are shown in figure 2.1. The detector ("sensor" in the scheme) can be seen as a capacitance (C_d) in parallel to a generator (I_{in}). The signal generated by the detector is then amplified, before to be compared to a reference voltage level (V_{th}) in the discriminator, which converts it in a logical signal and finally enter in a Time to Digital Converter (TDC), that measure the time interval between the particle trigger (Also its time resolution must be considered), coming from a different detector or an external source sensible to the passage of the particle and the crossing of the threshold level V_{th}.

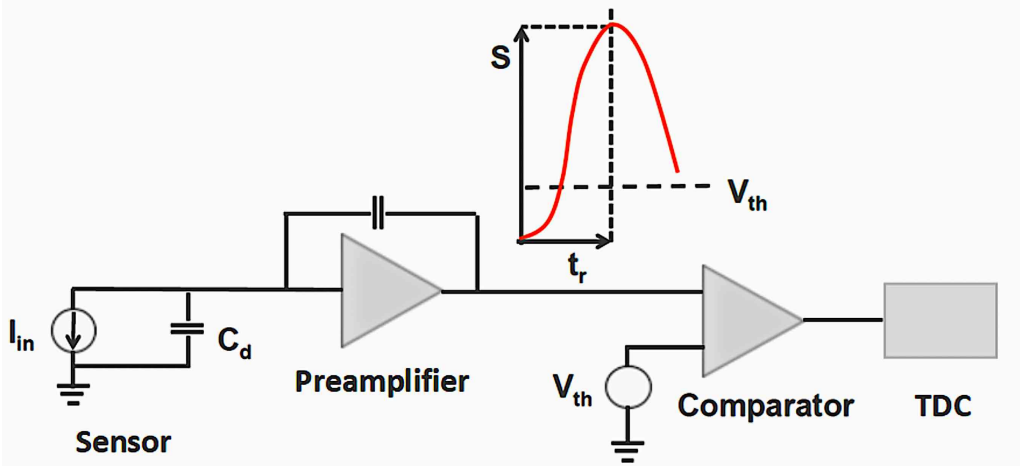

Figure 2.1: Basic elements of timing detector. Particle arrival time is defined as the time t_0 at which the signal exceeds the threshold voltage V_{th} [30].

Considering this measurement chain the total time resolution can be written as the quadratic sum of the contributions related to each element:

$$\sigma^2_{tot} = \sigma^2_{Current} + \sigma^2_{TimeSlewing} + \sigma^2_{Jitter} + \sigma^2_{TDC} \tag{2.1}$$

- **Current** contribution is related to the Shockley-Ramo theorem (B.18). As shown, the induced current depends on many factors and a small variation in i(t) reflects on a variation of the signal shape, that as a consequence spoils the time resolution. This term is the sum of two different effects:

  $$\sigma^2_{Current} = \sigma^2_{LandauNoise} + \sigma^2_{Distortion} \tag{2.2}$$

  the first, related to the stochastic nature of the energy deposition and number of pairs produced (see section B.1) and the second, due to a non-uniform weighting field and carrier drift velocity.

- **Time slewing** (or time walk) is linked to the analog to digital conversion of the signals and to the comparison with a fixed threshold V_{th}.

  As shown in the figure 2.2, two signals with different amplitudes cross the threshold at different times. The instant t_d in which a signal with amplitude S overcome the V_{th} is in fact proportional to

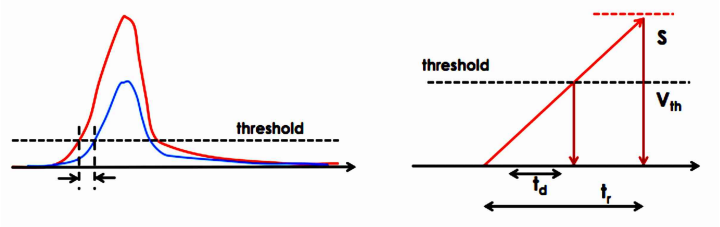

Figure 2.2: (Left) Signals of different amplitude cross a fixed threshold at different times, generating a delay on the discriminator response proportional to the amplitude of the signal. (Right) A linear signal, with amplitude S and rise time t_r crosses the threshold V_{th} with a delay t_d.

$$t_d \propto \frac{t_r V_{th}}{S} = \frac{V_{th}}{dV/dt} \tag{2.3}$$

where t_r is the rising time. The time resolution due to this effect is then the RMS of the t_d distribution:

$$\sigma_{TimeSlewing} = [t_d]_{RMS} \propto \left[\frac{N}{dV/dt}\right]_{RMS} \tag{2.4}$$

being N, the noise amplitude.

- **Jitter** contribution can be written as

$$\sigma_{Jitter} = \frac{N}{|dV/dt|_{V_{th}}} = \frac{t_r}{S/N} \tag{2.5}$$

where N is the RMS of the noise voltage. The signal level in fact, also for a fixed amplitude is affected by the the detector and electronic noise. As a consequence the crossing threshold time fluctuates, as shown in figure 2.3.

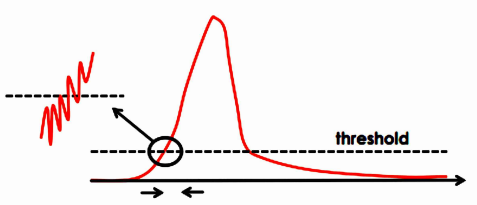

Figure 2.3: Noise causes an uncertainty on the crossing time of the threshold value.

- **TDC** contribution is related to digitalization of the time of the digital signal's edges by the Time to Digital Converter. In particular the time delay between the start and the end of the signal is given by the number n of clock cycles (each one with a duration Δt) between the two events counter of internal clock cycles: nΔt. Being n an integer number, the time resolution related to the TDC results

$$\sigma_{TDC} = \frac{\Delta t}{\sqrt{12}} \tag{2.6}$$

2.1.2 Thickness

As shown in the previous paragraph, in order to have the best possible time resolution, a large signal to noise ratio (S/N) is needed. This may suggest to prefer a thicker detector, in which the number of generated charges is higher. In particular, for the silicon, where the mean number of pairs created for unity thickness is n = 73, the total charge is proportional to

$$Q_{tot} = Nqd = 73\,qd \tag{2.7}$$

where d is the thickness of the considered detector. However, from the Shockley-Ramo theorem (B.18), each charge generates a lower initial current (since the weighting field is inversely proportional to the sensor thickness d):

$$i(t) \propto qv\frac{1}{d} \tag{2.8}$$

Resulting in a maximum current I_{max} that is independent on the thickness:

$$I_{max} \propto= Ndqv_{sat}\frac{1}{d} = Nqv_{sat} = 73qv_{sat} \tag{2.9}$$

being v_{sat}, the saturation velocity of the carriers, expected for large weighting electric field. Considering the limit of this velocity, as shown in figure 2.4, a thicker detector reflects on a longer collection time, that as a consequence worsen the time resolution.

2.1.3 Gain

As described, at high applied bias, the velocity of the carriers saturates; if the electric field is increased above, a multiplication process starts. If kept under control below a certain threshold or stopped after a while, this process doesn't damage the detector and rather can be exploit to improve the time resolution (see section 2.2).

When the electric field is strong enough, the primary electrons or holes are accelerated to high enough energies to knock other bound electrons free, creating secondary electron-hole pairs which are in turn accelerated and free additional electrons, giving origin to an avalanche multiplication. This process is called impact ionization mechanism.

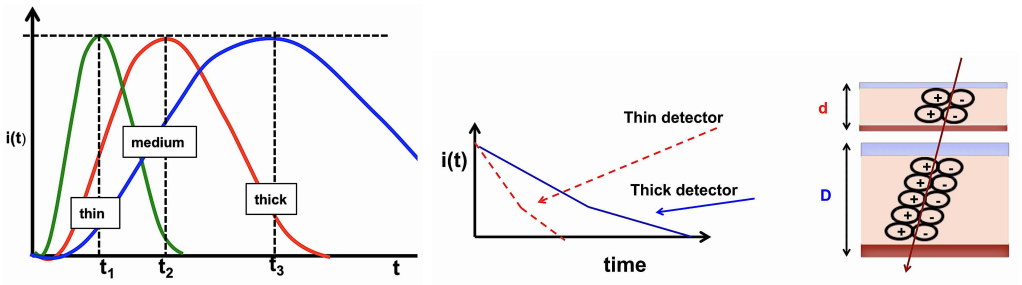

Figure 2.4: The initial signal amplitude in silicon sensors does not depend on their thickness: thin and thick detectors have the same maximum current, but thick detectors have longer signals.

The most commonly used local avalanche generation model is based on the empirical expression of Chynoweth [31], that put in relation the ionization rates, i.e. the number of electron-hole pairs n generated by a carrier per unit distance travelled ($\alpha_{n,p}$ respectively for electrons and holes) with the electric field:

$$\alpha_{n,p} = \alpha_{n,p,\infty} e^{-\frac{\beta_{n,p}}{|E|}} \tag{2.10}$$

where $\alpha_{n,p,\infty}$ and $\beta_{n,p}$ are constants of different values for electrons and holes.

If we consider the number of e-h pairs produced in silicon per cm^3 per unit time, called generation rate U_{av}, we have that for a uniform electric field the increased number of charges of one type is

$$U_{av} = \frac{dn}{dt} = \frac{dp}{dt} = \alpha_n n v_n + \alpha_p p v_p \tag{2.11}$$

with $v_{n,p}$ the carrier velocity of electron and holes, respectively.

So that the charge multiplication factor, called gain G, can be defined for both electrons and holes as:

$$G = e^{\alpha x} \tag{2.12}$$

As long as the gain remains finite, the detectors works in linear mode, but at a certain point, for values of the electric field greater than $\sim$ 400-500 kV/cm, the gain tend to infinite and the detector goes in a condition of uncontrolled multiplication called breakdown.

2.2 Low Gain Avalanche Detector (LGAD)

Low Gain Avalanche Detectors, also known as Ultra Fast Silicon Detectors (UFSD), are an evolution of the n-on-p planar silicon sensors, optimized to provide both good spatial resolution and high timing performance and based on an internal, low multiplication mechanism, obtained by implanting a heavily doped layer below the p-n junction. The key points of LGADs optimized for timing are: signals large and fast enough to assure excellent timing performance while maintaining almost unchanged levels of noise, reduced Landau fluctuations and a very uniform weighting field.

2.2.1 LGAD design

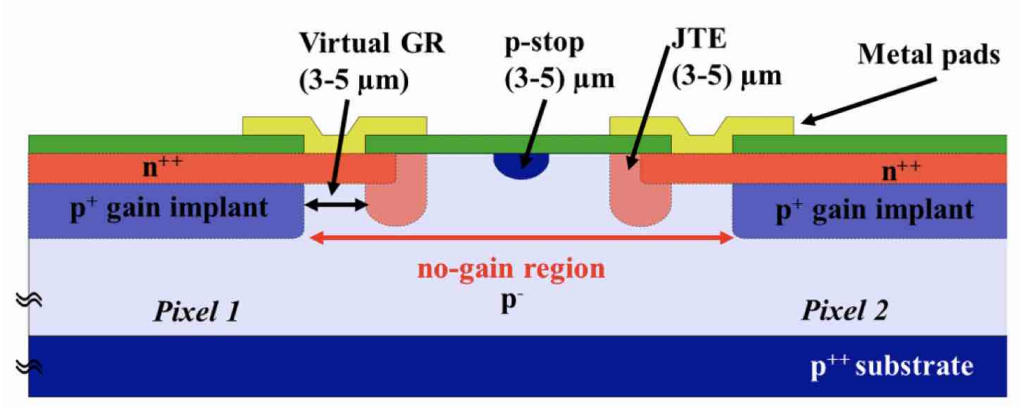

Figure 2.5: LGAD design, with an additional p^+-layer right below the n^{++}- type silicon.

The figure 2.5 shows the typical base elements of an LGAD. The one that is reported is an $n^{++}/p^+/p^-/p^{++}$ junction scheme, where the p^+ implant below the n^{++} electrode, called gain layer, usually doped with Boron atoms, is the region in which the impact ionization process (see subsection 2.1.3) takes place. At the pixel (or pad) edge, an additional virtual Guard Ring (vGR) and a Junction Termination Extension (JTE) are implemented in order to prevent premature breakdown (BD) at the pads border and to ensure the uniformity of the electric field [32] .The Guard Ring consists of a gap between the end of the gain layer and the n^{++} edges, while JTE is a deep low-concentration n-type region at the junction edge. These termination structures use some of the sensor's area and, as a consequence, introduce an inter-pad region in which the gain is completely suppressed. This is the so-called no-gain region, defined as the distance between two adjacent gain regions. Neighboring pads are electrically isolated by a narrow p^+ ring, called p-stop, which separates the n^{++} electrodes stopping the diffusion of electrons

through adjacent pads. Usually at the top also layers of silicon nitride and silicon dioxide are present as antireflective and insulator coating.

2.2.2 Main features

Local high electric field

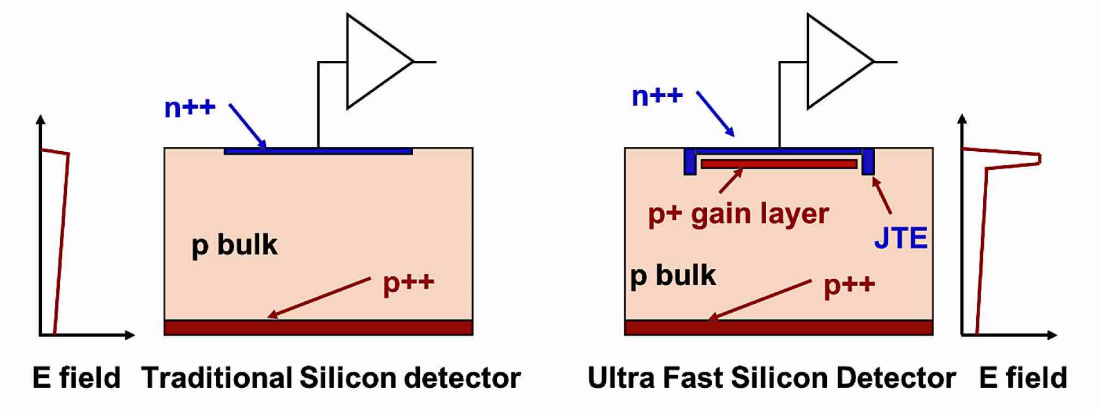

Figure 2.6: Cross-section diagrams comparing a standard silicon detector and an LGAD with an additional with an additional p^+ layer implant, right below the n^{++}-type silicon, providing the larger electric field needed for charge multiplication.

Figure 2.6 shows the difference between the electric field generated inside a traditional silicon internal structure (left) and the one in an n-in-p LGAD (right). In both, the two highly doped electrodes n^{++} and p^{++} are shown in blue and red, respectively, and the p-bulk in light red. The main difference regards the additional p^+-doped thin layer near the p-n junction in the LGAD design. The introduction of this layer creates a high electric field which accelerates the electrons enough to start multiplication. The gain mechanism should happen when the reverse bias on the sensor exceeds the depletion voltage value, but far from the breakdown voltage limit. In standard silicon sensors, to have impact ionization is necessary to apply a very high external bias voltage, which inevitably causes the breakdown of the device; on the other hand, in LGADs, the p^+ layer locally generates an electric field high enough to activate the charge multiplication process in the volume between the gain layer and the n^{++} electrode. So, as shown in this case the electric field is divided in two parts: a very high electric field ($E \sim 300$ kV/cm) situated along the p-n junction in which the multiplications happens, and a lower electric field in the rest of the depletion zone, of the order of 30 kV/cm, that allows the charges to saturate their drift velocity, without starts the multiplication.

Low gain and small thickness

LGADs are especially used to detect charged particles. In particular MIPs, creating in one micron of silicon $n_{pairs} \sim 73$ electron-hole pairs, give rise to a signal high enough to permit the usage of low gain, avoiding a number of problems, such the increase in sensor noise, the difficulties in sensor segmentation (due to the very high fields), and the high power consumption after irradiation. The underlying idea of the LGAD design is to use the lowest gain that is sufficient to perform accurate single particle time measurements. The value of the current di_G generated by a gain G inside the multiplication layer can be estimated using the Ramo's theorem (B.18). Considering a number of electrons entering in the gain region in a time interval dt equal to $n_{pairs} v_{sat} dt$, which generate $dN_G \propto n_{pairs} v_{sat} dt G$ new pairs, the induced current results:

$$di_G = dN_G q v \frac{1}{d} \propto \frac{G}{d} dt \tag{2.13}$$

which leads to the expression:

$$\frac{di_G}{dt} \propto \frac{G}{d} \tag{2.14}$$

so the increase in signal current derivative due to the gain mechanism is proportional to the ratio of the gain value over the sensor thickness (G/d). Indeed, from (2.14) the thickness of the detector is the other important variable. This last one has instead an effect on the rise time (slew rate) that is determined by the electrons drift time. In particular, thin sensors have a much faster rising edge (2.4), which in turn improves the time resolution, since jitter and time walk are minimized, as shown in figure 2.7. However if we want to keep a gain of 10-20, the detector can't be too thin, otherwise the capacitance arises and the signal becomes too low to be readable from the readout electronics.

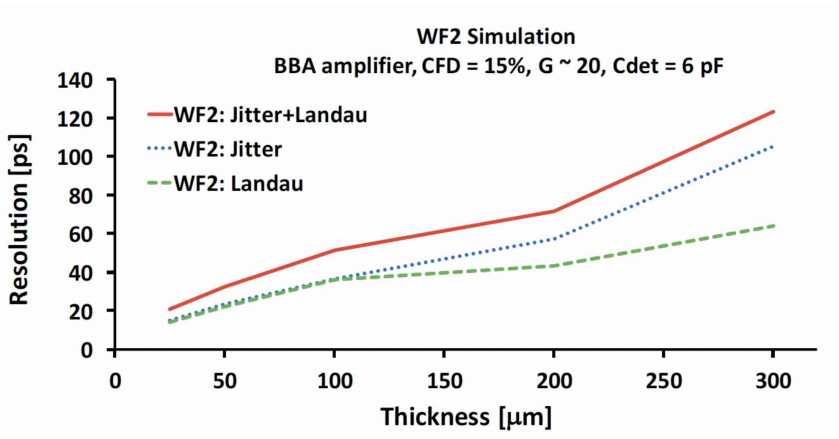

Figure 2.7: Time resolution as a function of the LGAD thickness [33] simulated with Weightfield2 (WF2) [35].

Noise contributions to time resolution

Plot concerning simulations on jitter and Landau noise as a function of the Constant Fraction Discriminator (CFD) are shown in figure 2.8 (top) and 2.8 (bottom) for different gains and thicknesses, respectively. As shown, the jitter contribution is higher in the beginning and in the end of the signal, where the signal shape is less steep and is dominant for lower gain. Landau fluctuations are minimized using a low threshold and for thinner detectors, but they are independent of the gain because beyond a certain number of carriers the process seems to be more deterministic [36].

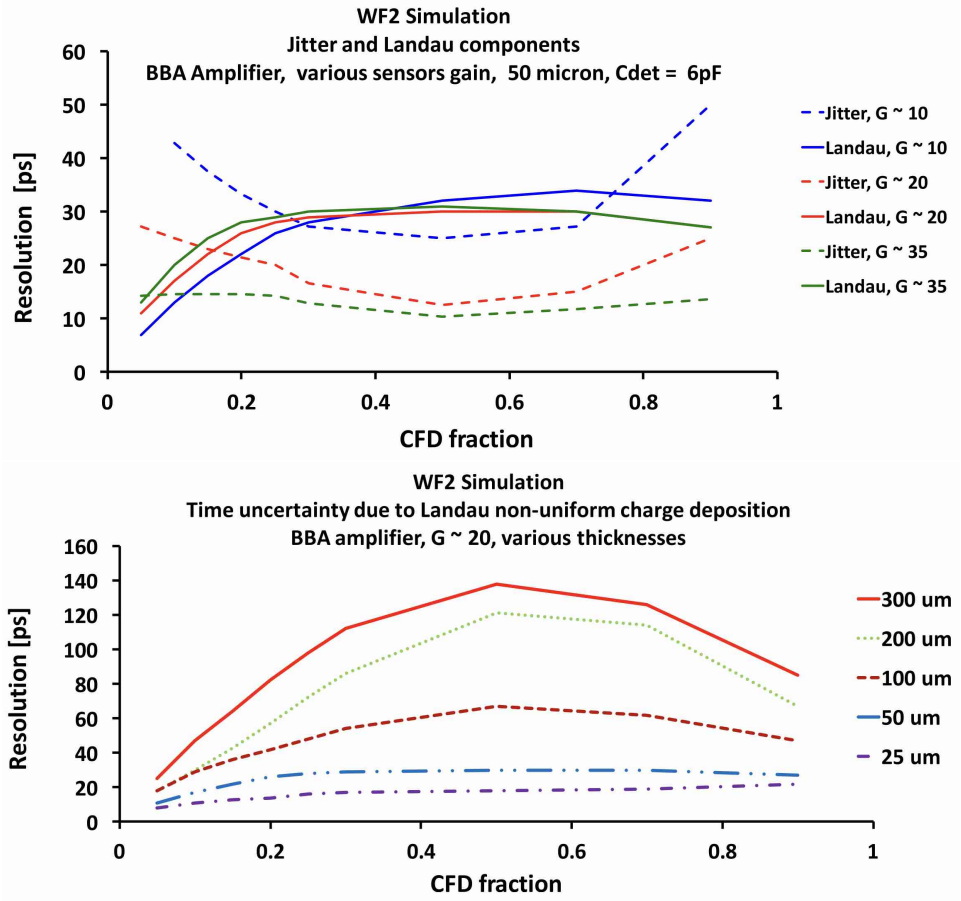

Figure 2.8: Jitter and Landau noise contributions to the total time resolution as a function of the CFD value for different gains (top); Landau noise contribution to the time resolution as a function of the CFD value for different detector thicknesses (bottom). [34]

2.2.3 Applications

In the last years there has been a growing interest for the application of silicon detectors with very good timing resolution in both physics experiments and outside the HEP realm. The combined spatial and timing precision offered by LGADs will represent a breakthrough and will open up a range of new opportunities for applications that benefit from the combination of position and timing information, in a whole array of different fields.

TOF PID in physics experiments

The main application of timing detectors in physics experiments is connected to the particle identification. The Time-Of-Flight (TOF) technique is used to separate particles with momenta below few GeV/c and is based on the measurement of the time interval of the travel along a known fight path L, so that the particle velocity v = L/t can be obtained. The velocity, together with the measurement of the momentum, gives the value of the particle mass:

$$m = \frac{p}{c}\sqrt{\frac{c^2t^2}{L^2} - 1} \tag{2.15}$$

with a resolution

$$\left(\frac{\delta m}{m}\right)^2 = \left(\frac{\delta p}{p}\right)^2 + \left(\gamma^2\frac{\delta L}{L}\right)^2 + \left(\gamma^2\frac{\delta t}{t}\right)^2 \tag{2.16}$$

The TOF difference for two particles of different masses m_1 and m_2 having the same momentum p and travelling along the same track length L is

$$\Delta t = t_1 - t_2 \simeq \frac{Lc}{2p^2}(m_1^2 - m_2^2) \tag{2.17}$$

Starting from this equation, the separation power n_σ is defined as

$$n_\sigma = \frac{\Delta t}{\sigma_{TOF}} \tag{2.18}$$

For high momenta, the dominant factor in the mass resolution and therefore in the separation power is the time resolution of the detector. This is the reason why timing detectors with a very good resolution are needed. A better better time resolution corresponds to a smaller error on the value of the masses and an higher separation power (see figure 1.6).

4D tracking

Due to the huge increasing of the accelerators' luminosity, that brings to the presence of very high pile-up rate, in the past few years there has been growing interest in the development of this kind of detectors also for tracking purposes. In physics experiments,

the ability to simultaneously measure accurately the time of passage and the position of impinging charged particles, the 4D tracking, is of fundamental importance to reduce the background. An example can be the future upgrade of the Large Hadron Collider, HL-LHC [37] number of events per bunch crossing will be of the order of 150-200, with an average distance between vertexes of 500 micron, in a time window of 150 ps, which will bring to a 10-15% [38] of vertexes composed by two overlapping events. The inclusion of timing information allows to separate events with overlapping vertices, enabling exploiting the full potential of the future colliders luminosity capability. In order to retain the full power of timing information, it is actually sufficient to assign a time to each track and not to every hit. This requires the implementation of a dedicated timing layer, either inside or outside the main silicon tracker volume. A schematic representation of how the time measurement allows to disentangle two overlapping events is shown in figure 2.9.

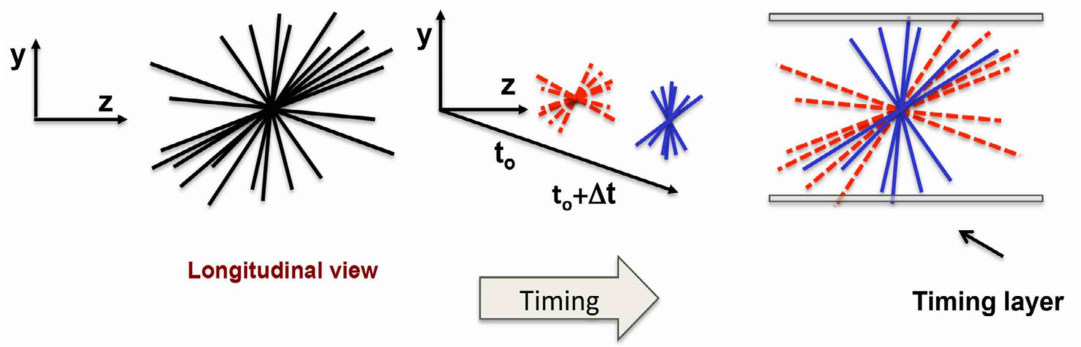

Figure 2.9: Schematic representation of the power of timing information in distinguishing overlapping events using a timing layer.

Other applications

The R&D of thin silicon sensors with excellent tracking and timing resolution, capable to cover large areas, will be extremely beneficial also in the medical field and in many industrial applications.

- **Positron Emission Tomography (PET):** PET is based on the injection inside the body of a radionuclide, which is absorbed by the diseased tissue or organ. The radionuclide, subsequently, through β^+ decay, creates an electron-positron pair and, in particular, the positron annihilates after about 10-9 s and, produces a pair of 0.511 MeV back-to-back photons. This annihilation vertex can be reconstructed through the use of very precise timing detectors, giving information on the point in which the radionuclides have been accumulated. Improving the time resolution, gives the possibility to reduce the background present in the measurement by increasing the precision on the arrival time of the photons and thus reducing the

number of spurious events. Position resolution of an LGAD based system is more than a factor 10 better than that of a more recent PET systems that use very fast silicon photomultipliers (SiPM) [39] yet with comparable time resolution. This will considerably enhance the image quality and or reduce the dose to the patient.

- **Particle counting and hadrotherapy:** LGAD features are also beneficial for what concerns single particle counting applications allowing to reach unprecedented rate capabilities. In hadrotherapy they are very suitable to monitor therapeutic beams, measuring the particles range and the dose profile with millimeter resolution during clinical treatments [40], by directly counting the number of hadrons, giving a very precise control on the energy delivered to the patient, or exploiting the emission of prompt gammas (PG) [41]. In this case, the time-of-flight measurement can be used either to derive indirect information on ion-ranges [42] [43]or to reduce neutron-induced background.

- **3D and Robotic Vision:** finally, the possibility to perform precise measurement of light pulses reflected by objects at unknown distance also allow the precise reconstruction of 3D images, fundamental in many different LiDAR (Light Detection And Ranging) applications, as well as in imaging and robotic vision.

Chapter 3

Measurements on first very thin LGAD prototypes

3.1 Detectors used

LGADs of three different thickness was studied: 50 μm, 35 μm and 25 μm. These last two designs in particular were the very first production from FBK (Fondazione Bruno Kessler, Italy) of such thin LGADs. A total of 18 sensors from these production was characterized, both single channel and matrices, with different inter-pad design, and compared with sensor with the same design but without a gain layer (PIN).

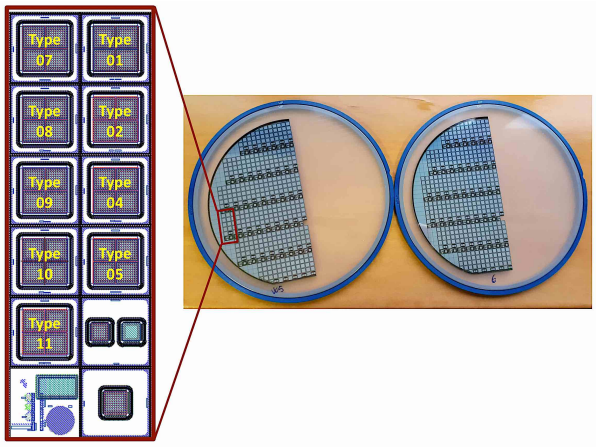

Figure 3.1: Left part of the UFSD3.2 production reticle for wafer 5 and wafer 6, made of 9 types of matrices, PIN-LGAD pairs and single pads.

50 μm LGADs from two different manufacturers were studied, both from FBK and HPK (Hamamatsu Photonics K.K., Japan), and compared with the thinner design.

3.1.1 25 and 35 μm-thick prototypes

The tested detectors belong to the UFSD3.2 production, characterized by an extremely thin thickness exploration, arriving to 25 μm-thick wafers. Basic reticle and wafer layouts are shown in figure 3.1. The sensors have a different thickness and doping concentration of both the bulk and the multiplication layer. In addition, different types of pads insulation approaches are applied to the 2×2 matrices, which were produced with various inter-pad configurations of the gain layer distance and p-stop design. All the sensors have an n-in-p structure, with a p^+ doped gain layer.

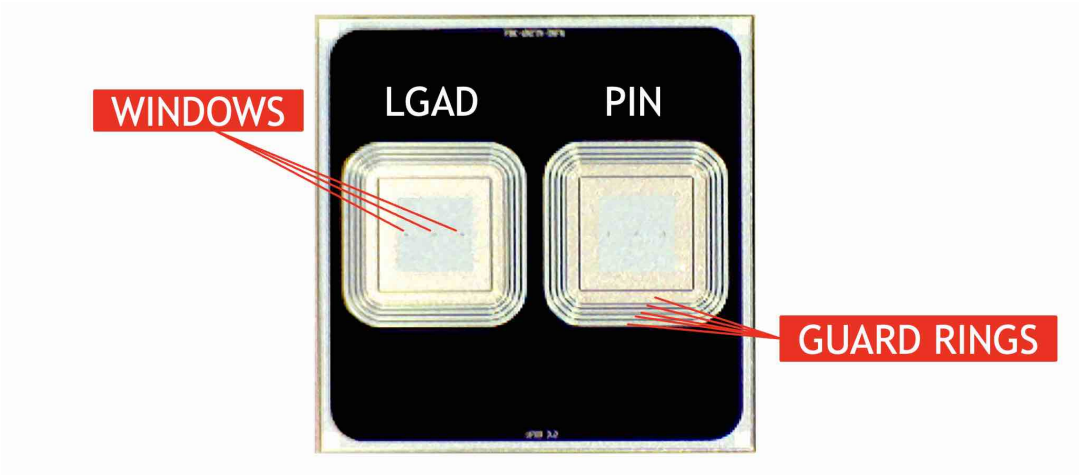

Figure 3.2: PIN-LGAD structure. On the left a single LGAD and on the right, the equivalent PIN with the same structure, but without the gain layer. Five concentric guard rings surrounding each of the two 1×1 mm^2 pads and three non-metallized areas (windows) are visible.

Among the eighteen structures analyzed, nine belong to wafer W5, with a thickness of 25 μm and nine to wafer W6, with a thickness of 35 μm. Some difficulties in the production of such thin sensors brought to a difference in the doping concentration of the two wafers. In particular, W5 has highly doped bulk and gain layer, while in the W6 a type inversion occurred (due to oxygen diffusion from wafer to the bulk: oxygen defects in silicon behave like n defects), resulting in a n-doped bulk. For each wafer, three PIN-LGAD structures and six matrices, were tested. A list of the different sensors with the corresponding labels is reported in table 3.1.

The PIN-LGAD structures are shown in figure 3.2. The LGAD (left) has an area of 1×1 mm^2 and is surrounded by five concentric guard rings (GR), where the inner one is the biasing ring. The whole surface of the sensor is covered by a metallization, except for three 20.5×20.5 μm^2 (see section 3.3.2.2) non-covered areas (windows), to perform the tests with a laser setup. The PIN (right) has the same design of the LGAD, but without the gain layer.

STRUCTURE		AREA	WAFER	PROTOTYPES (COLUMN-ROW OF THE RETICLE)	LABEL
PIN-LGAD	Structure with a single LGAD and the relative PIN with the same design but without the gain layer	1x1 mm^2	W6 (35 µm)	8-3 9-3 10-3	W6_8-3_35µm W6_9-3_35µm W6_10-3_35µm
			W5 (25 µm)	8-3 9-3 10-3	W5_8-3_25µm W5_9-3_25µm W5_10-3_25µm
TYPE4 MATRICES 2X2	Biasing ring external to the pads	1.3x1.3 mm^2	W6 (35 µm)	8-3 9-3 10-3	W6_8-3_T4_35µm W6_9-3_T4_35µm W6_10-3_T4 35µm
			W5 (25 µm)	8-3 9-3 10-3	W5_8-3_T4_25µm W5_9-3_T4_25µm W5_10-3_T4_25µm
TYPE10 MATRICES 2X2	Extension of the biasing ring between the pads	1.3x1.3 mm^2	W6 (35 µm)	8-3 9-3 10-3	W6_8-3_T10_35µm W6_9-3_T10_35µm W6_10-3_T10_35µm
			W5 (25 µm)	8-3 9-3 10-3	W5_8-3_T10_25µm W5_9-3_T10_25µm W5_10-3_T10_25µm

Table 3.1: List of the tested thin LGAD sensors with their characteristics and the corresponding labels used in the analysis.

The two types of matrices tested (type4 and type10), characterized by different inter-pad design, are shown in figure 3.3. Four 1.3×1.3 mm^2 pads with the same characteristics are present, each one with three internal windows. Two additionally non-covered areas, one between the two pads on the top and one between the two pads on the bottom (inter-pad windows), are visible; these are needed to investigate the edge effects. The pads are surrounded by five guard rings, of which the most internal one is the biasing ring. The type4 matrix is characterized by a biasing ring that is external to the pads, which in this case are near to each other, while in type10 matrix, an extension of the biasing ring is present between the pads.

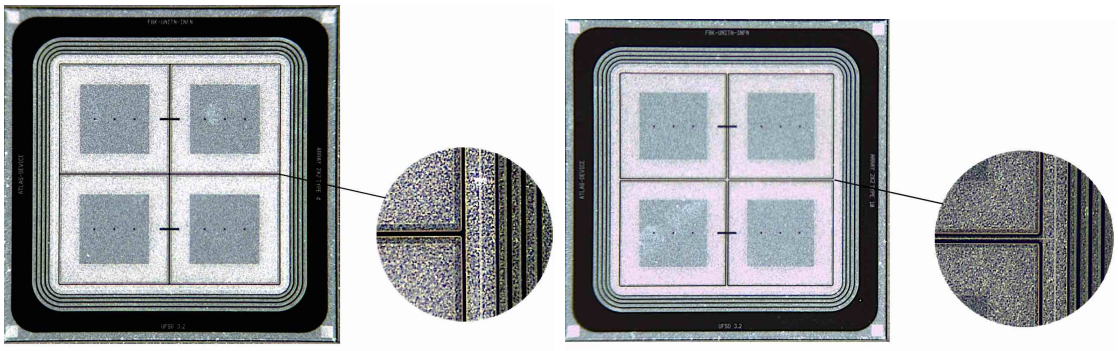

Figure 3.3: Type4 matrix on the left and type10 on the right, with a zoom on the inter-pad area. In the type10 one, an extension of the biasing guard ring is present between the four pads.

3.1.2 50 μm-thick prototypes

Two different LGADs with a thickness of 50 μm were tested, to have a comparison with the thinner ones:

- 4S (figure 3.4) is a matrix with four 1x3 mm^2 pads, produced by HPK. Also in this case a metallization covers the pads, and two 25.2×25.2 μm^2 (see section 3.3.2.2) window, one on the left-up and the other on the right-down are present, with two additional ones crossing the neighbors pads edges. A corresponding PIN (5S) with the same layout, but without the gain layer, was used for the evaluation of the gain.

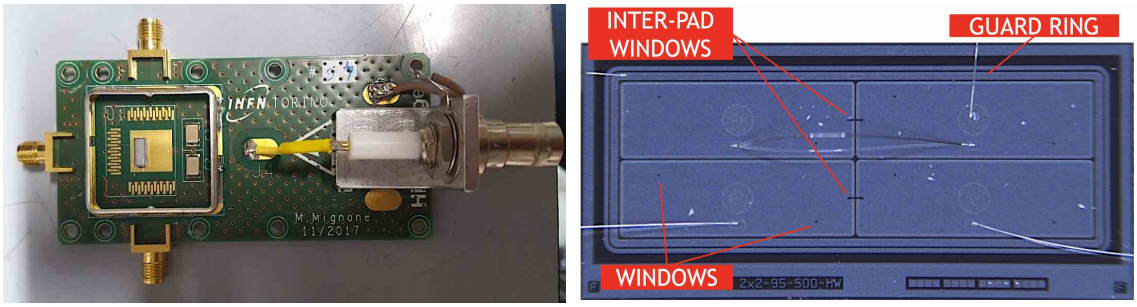

Figure 3.4: 4S connected to the board, with a zoom on the matrix on the right. In the right photo, the pad and inter-pad windows are visible, as well as the connections to the board and a bonding between the two top pads.

- SAMPLE2, produced by FBK, is a single pad LGAD with a dimension of 1×1 mm^2. In this case the metallization is present only in a corona near the edges, so the laser measurements can be done on the whole central area. In figure 3.5 the LGAD is on the right and the correspondent PIN is visible on the left.

While in the previous case the tests were made firstly on bare silicon, in this case all the measurements are performed with the sensors connected to a board.

3.2 Preliminary measurements

A fully electrical characterization of an LGAD sensor can be done performing current and capacitance measurements at different bias voltages. In particular, two main measurements are needed: current-voltage (IV) and capacitance-voltage characteristic (CV). In this section, the IV and CV curves of the sensors listed above are reported, together with the experimental setups and an analysis of the results.

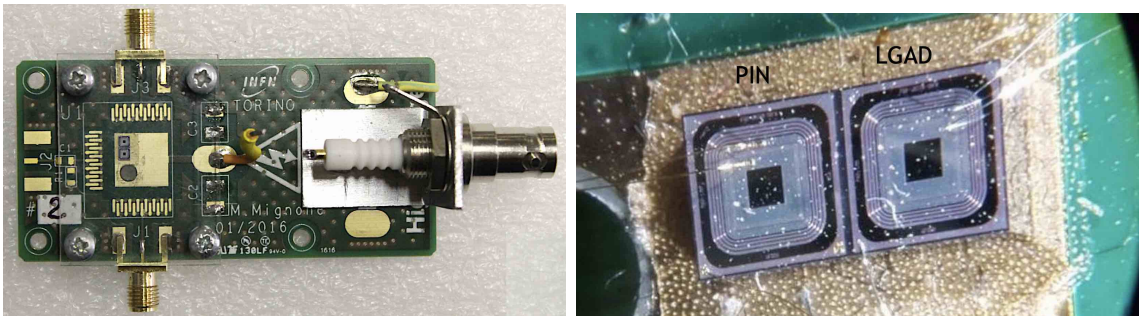

Figure 3.5: SAMPLE2 connected to the board, with a zoom on the PIN-LGAD couple on the right. In the photo, the connections to the board are visible.

3.2.1 IV characteristic

The current as a function of the reversed voltage applied (IV) has been measured. The primary goal of IV characteristic is to evaluate the breakdown voltage V_{BD}. This measurement also gives information on the voltage interval in which the sensor can be operated. Moreover, the IV characteristics helps to evaluate the different inter-pad configuration indeed some aggressive designs can lead to a premature breakdown of the pads.

3.2.1.1 Experimental setup

The characterization of all the 25 μm and 35 μm-thick prototypes was initially done on bare silicon and then repeated for one of them after the connection to the board, before the tests with the laser. The measurements on bare silicon were performed using a probe station. The bare sensors were positioned on the golden plate, called chuck. With the help of some markers, thin needles can be put precisely in contact with the sensors' surface in some useful points. A negative high voltage was applied to the chuck on which the p-type backplane of the sensors was positioned, so that, having the needles on the top at ground potential, the sensors result in reverse bias condition.

The whole setup is shown in figure 3.6. The negative HV on the chuck is provided by a CAEN power supply [44]. Needles, at ground potential, can be in contact with pads and the guard ring, but just one of them (the one with the red corocodile in the figure) is connected to the Keithley 6487 picoammeter [45], that is used to perform the current measurements. All the instruments are controlled by a LabVIEW [46] program, from which all the parameters can be set and controlled in real time during the measurements. All the tests were done maintaining the probe station in a dark environment and the values of temperature and humidity were registered for each curve through a sensor placed near the plate, since they can affect the parameters of the IV characteristics.

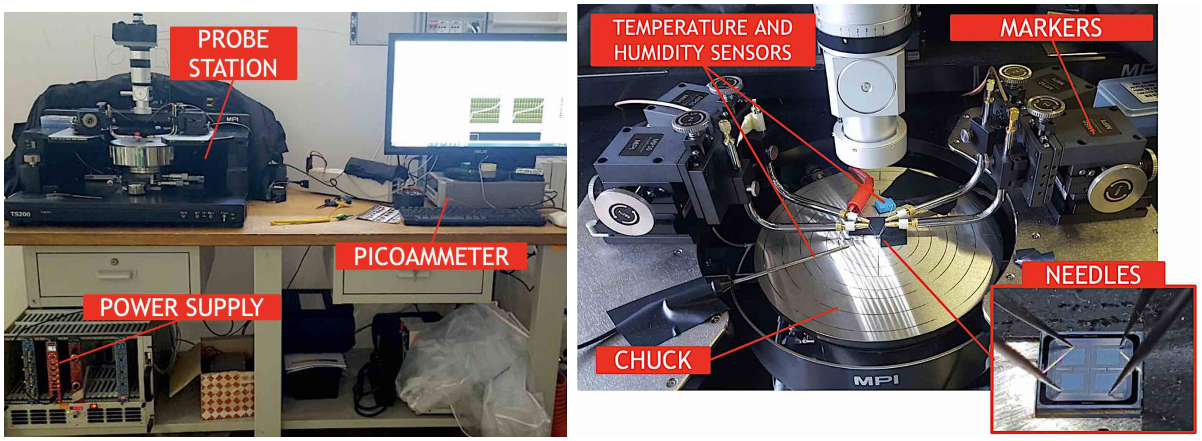

Figure 3.6: Experimental setup for the measurement of the IV characteristics, composed by the probe station, a power supply, a picoammeter and the computer, from which, through a LabView program, all the instruments are controlled (left). Sensor positioned on the chuck of the probe station, with four needles (since a matrix is under test in this specific case) connected to the different elements (right). The needle to which the red crocodile is attached is the one connected to the picoammeter that performs the current measurement. A sensor for the temperature and one for the humidity measurements are visible in the photo.

In particular, the measurements on the PIN-LGAD structures are performed with two needles, one in contact with the internal pad and the other in contact with guard ring, to have a more uniform electric field inside the depletion region of the sensor and work in a condition similar to the one of a sensor attached to a board. This configuration in the analysis part is referred to as 2-needles setup. The measurement is repeated two times, the first one with the picoammeter connected to the needle in touch with the internal pad, and the second time connecting the picoammeter to the guard ring.

A similar configuration of the setup was adopted with the matrices. In this case, having just four markers in the probe station, 1 needle was placed on the GR and three on the pads in a way in which the floating pad (the one not directly powered) was the one opposite to the measured one. The 4-needles setup is shown in figure 3.8.

A similar setup was used for the LGADs bonded to the boards, except for the use of the probe station, which in this case was not necessary, since the powering and the read-out of the signal can be done through specific channels on the boards. The sensor was connected to power supply, picoammeter and computer in the same configuration as before and all the measurements were done in a dark environment, with sensor inside a small box, as shown in figure 3.9. The analogous configuration of the 4-needles setup for the LGAD matrices was created by connecting the pads that were not under measurement to ground.

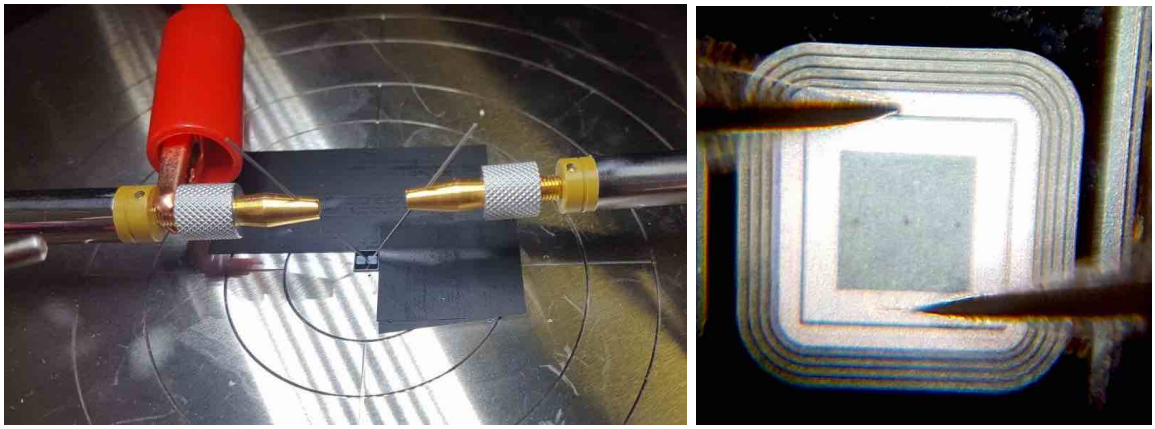

Figure 3.7: 2-needles setup: the measuring pin (connected to the picoammeter) is placed in touch with the element (LGAD pad or guard ring) on which the current measurement is performed, while the other one powers up the second element (left). Photo taken by the microscope of the probe station (right).

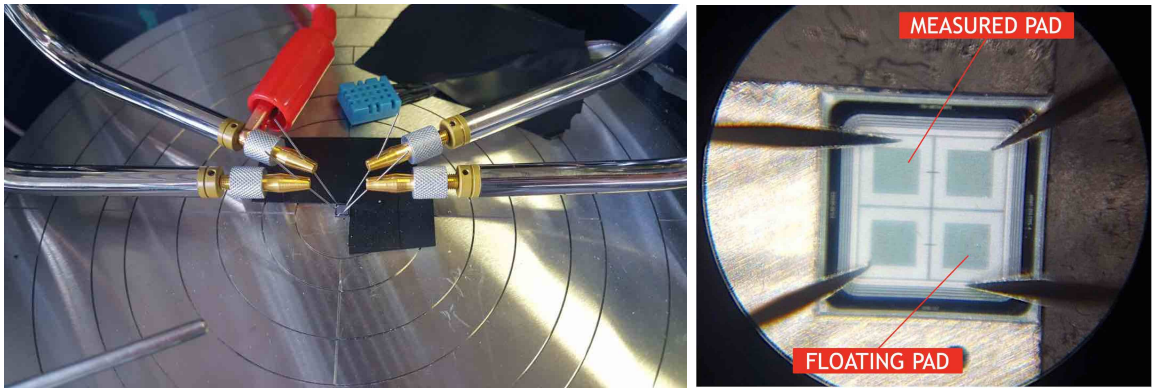

Figure 3.8: 4-needles setup: the measuring needle (connected to the picoammeter) is placed in touch with the pad on which the current measurement is performed, while the other ones are needed to power up the two neighboring pads and the guard ring (left). Photo taken by the microscope of the probe station (right).

3.2.1.2 Analysis of the results

PIN-LGAD structures

An example of IV curves performed on the bare PIN-LGAD structures, for the two thicknesses, is shown in figure 3.10. The curves in red and pink corresponds to the LGAD and its guard ring respectively, and analogously the blue and the light blue ones to the PIN and the relative guard ring. The behavior of IV characteristics of the LGAD

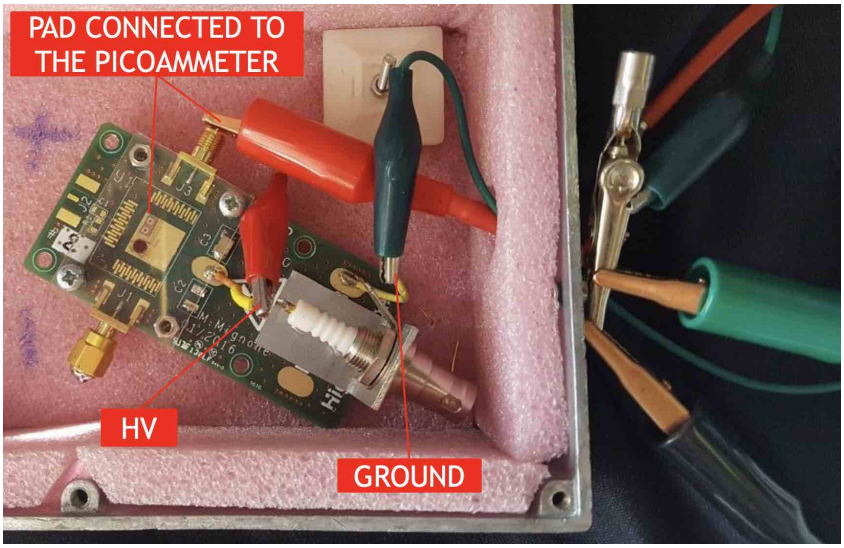

Figure 3.9: Part of the experimental setup used for the measurements of sensor connected to a board. The sensor is inside a box that during the measurements is closed and covered with a black cloth.

and the PIN are quite different as expected. For the PIN (blue) the leakage current remains low, until reaching the junction breakdown (BD) (not visible in the image for the W6 due to an imposed limitation on the voltage) in which the current starts to increase without control. On the contrary, for the LGAD (red), two main changes in the behavior are clearly visible: the first one due to the presence of the gain layer and in particular to its depletion (at $\sim$ 22V) and the second one correspond, as for the PIN, to the BD condition. The other main difference between W5 and W6, concerns the position of the pad and the guard ring curves (for both the PIN and LGAD). Guard rings for the W6, have an higher current, due to the type inversion of the wafer. The type inversion is not a problem in itself, since it doesn't affect the electric field inside the depletion region making the sensor working with the usual principles, however some side effects are present, in particular one of these is this increase in the GR leakage current, due to the fact that the GR in in this case is an n-implants inside an n-doped bulk, collecting, as consequence, charges generated from the whole bulk.

All the measurements were performed with a 2-needles setup, as explained before. Each measurement was done firstly on the LGAD, while biasing the GR and subsequently on the GR, while biasing the LGAD. The same was done on the PIN. In this setup configuration the internal pad and the GR are in parallel, so the total current that passes in the sensor is the sum of the current passing in the pad and the one passing in the guard ring. Through the LabView program a maximum limitation was imposed on this total current, to avoid silicon damages. This limitation causes a stop of the measurement in

the moment in which one of the two elements reaches the breakdown voltage, preventing the other one to reach it. As a consequence, the only breakdown that is visible in the curves is the one of the first of the two elements that reaches this condition. For what concerns the LGAD, is always the internal pad to stop the measurement, while for the PIN also the GR can arrive first to this condition.

A comparison between two LGAD with a thickness of 25 μm (blue and light blue curves) and two sensors with a thickness of 35 μm (red and pink curves) is shown in figure 3.11. In general the behavior of sensors that belong to the same wafer are similar, except for the value of the leakage current, due to the different condition of dark, that in the setup with the probe station is difficult to keep under control. More reliable considerations on the current will be done once the sensors will be connected to a board. Otherwise, two important values can be extracted from these curves. In particular, the value in which the gain layer depletes, corresponding to the first flex on the curve, is well visible and is around 22 V for both the thicknesses.

The second important value is the BD voltage. A table with a rough value of the breakdown voltages for all the LGAD is reported in table 3.2. A little dispersion of the values is present. Due to uncertainties in the sensor production process, the parameters always exhibit a distribution and in addition, also the different measurement conditions, i.e. temperature, humidity and light exposition, can have an influence on this values. However, as a general observation, all the BD voltages are around the same value for the same wafer thickness and as expected, the one for the 25 μm thickness is always lower then the one of 35 μm-thick sensors.

The BD voltage value can be extracted from the IV curve using two different methods [47]: Logarithmic Derivative (LD) and Inverse Logarithmic Derivative (ILD). LD consists on calculating the derivative of the logarithm of the IV curve, while ILD is just the inverse of the LD function:

$$LD = \frac{dln(|I|)}{dV} \tag{3.1}$$

$$ILD = \left(\frac{dln(|I|)}{dV}\right)^{-1} \tag{3.2}$$

The application of these two methods is shown in figure 3.12 for one of the analyzed sensors. Below the breakdown voltage, LD (blue dots) shows a linear voltage dependence with a positive slope and above breakdown, it starts with a linear decreasing, changing to a quadratic dependence at higher voltages; the maximum corresponds to the BD voltage on the horizontal axis. The opposite is for the ILD (light blue dots). To extract the value of the maximum (minimum) of the LD (ILD), a parabolic fit is done on the 10 points around the maximal (minimal) values of the IV curve.

Type4 and type10 matrices

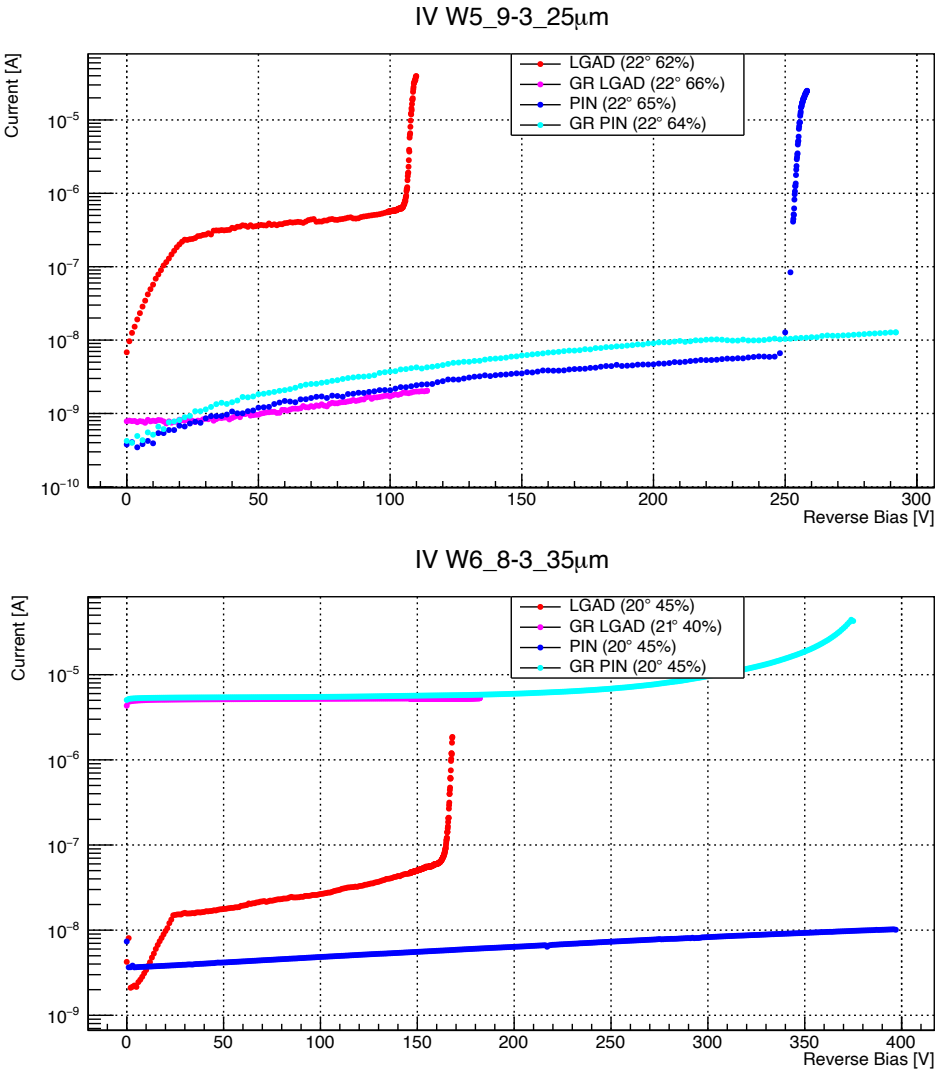

Figure 3.10: Example of measured IV characteristics of PIN-LGAD structures. In each graphic, four different IV characteristics are plotted: LGAD, PIN and the respective guard rings. All the measurements are performed with a 2-needles setup. In the legend the temperature and the humidity at which each curve was measured are reported. The plot on the top is relative to the W5 wafer (25 μm), while the one on the bottom corresponds to W6 wafer (35 μm).

Analogous considerations done for the single LGAD sensors are valid also for the tested matrices. For each wafer thickness, an example of measured IV curves is reported in figures 3.13 and 3.14, for type4 and type10 matrices, respectively. The measurements were done with the 4-needles setup explained before, with a floating pad. Since the pads

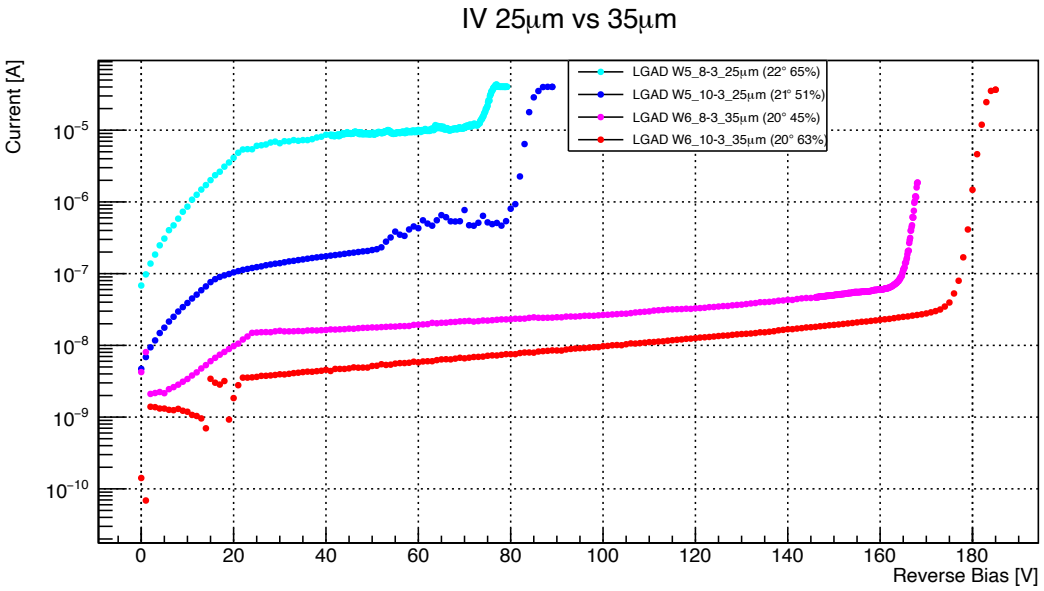

Figure 3.11: Comparison between IV curves of LGAD of 25 μm and 35 μm thicknesses.

			LGAD	GUARDRING
LGAD PIN-LGAD	W6	8-3	**167**	-
		9-3	**233**	-
		10-3	**175**	-
	W5	8-3	**72**	-
		9-3	**108**	-
		10-3	**84**	-

			LEFT-UP	RIGHT-UP	RIGHT-DOWN	LEFT-DOWN	GUARDRING
TYPE4	W6	8-3	**271**	-	**271**	-	-
		9-3	BROKEN				
		10-3	-	-	**249**	-	-
	W5	8-3	**107**	-	-	-	-
		9-3	BROKEN				
		10-3	-	**124**	**124**	**112**	-
TYPE10	W6	8-3	**198**	-	-	-	-
		9-3	**182**	**160**	-	**171**	-
		10-3	**119**	-	-	-	-
	W5	8-3	**278**	BROKEN	**298**	BROKEN	-
		9-3	**111**	**100**	**104**	**119**	**115**
		10-3	**119**	-	**123**	-	-

Table 3.2: Breakdown voltage for all the tested LGAD. The dash corresponds to the LGADs which didn't reach the breakdown, because of the limitation in the total delivered current to the sensor.

were in parallel, the first one that arrived to BD made the current reach the maximum limit that can be supplied to the sensor, stopping the measurement, so that the other

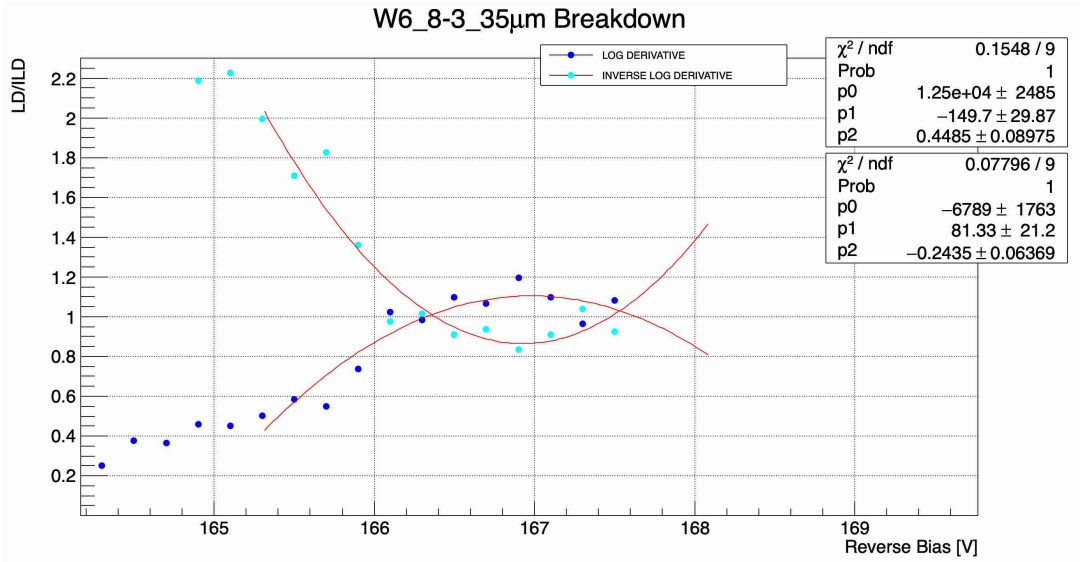

Figure 3.12: Example of logarithmic derivative and inverse logarithmic derivative methods to extract the breakdown voltage from IV curves. The vertical-axis scale in this case is linear.

ones could'n reach this condition. Ideally all the pads have the same BD voltage value, but a tiny spread among the four pads must be considered due to slight differences between pads related to the production uncertainties.

In the case of the matrices, the malfunctioning of some sensors was found and in some case the measurements suffered from the fact that one pad was floating. This problem was less evident in the type10 matrices, where the fact of having a GR between the pads helps to have a more uniform electric field also with a non-powered pad. This is well visible for example in the top plot of figure 3.14. The four pads reaches the breakdown in very similar values of voltage. Also in this case, for both the types and thicknesses, the depletion of the gain layer is reached around 22 V. The higher current of the guard ring in the W6 wafer due to the type inversion is well visible in the plots.

IV of a 25 μm LGAD connected to the board

After the measurements with the probe station one of the 25 μm-thick PIN-LGAD structure was bonded to a board with an amplification of 20, needed to perform all the measurements with the laser setup. The IV curve for this sensor was measured, in order to have a comparison with the previous one and see if the board introduce some effects. A plot with the IV characteristic, measured with the probe station and the one on sensor connected to the board is shown in figure 3.15. The slightly difference in the leakage current is due to the dark conditions in which the measurements were performed, since differently from the probe station setup, the board can be put in box well isolated from external light sources. The full depletion voltage is comparable, while the breakdown

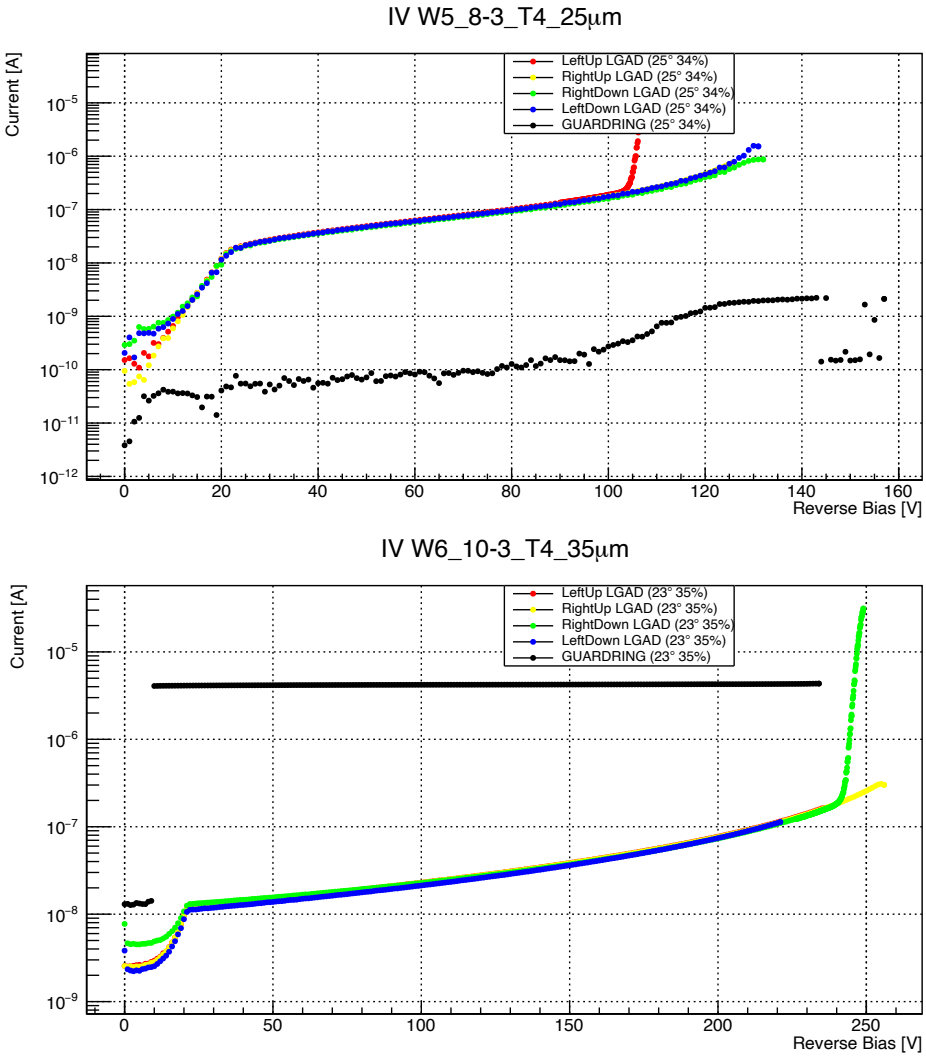

Figure 3.13: Example of measured IV characteristics of type4 matrices. In each graphic, five different IV are plotted: four corresponding to the pads and the black one corresponding to the biasing guard ring (GR). All the measurements were performed with a 4-needles setup. In the legend the temperature and the humidity at which each curve was measured are reported. The plot on the top is relative to the samples with the W5 wafer (25 μm), while the one on the bottom corresponds to W6 wafer (35 μm).

value seems to be a little higher.

50 μm LGADs and comparison with thinner thicknesses

Using the same setup, also the IV characteristics for the two 50 μm-thick LGAD mentioned above, were measured. In this case, the sensors were connected to a board

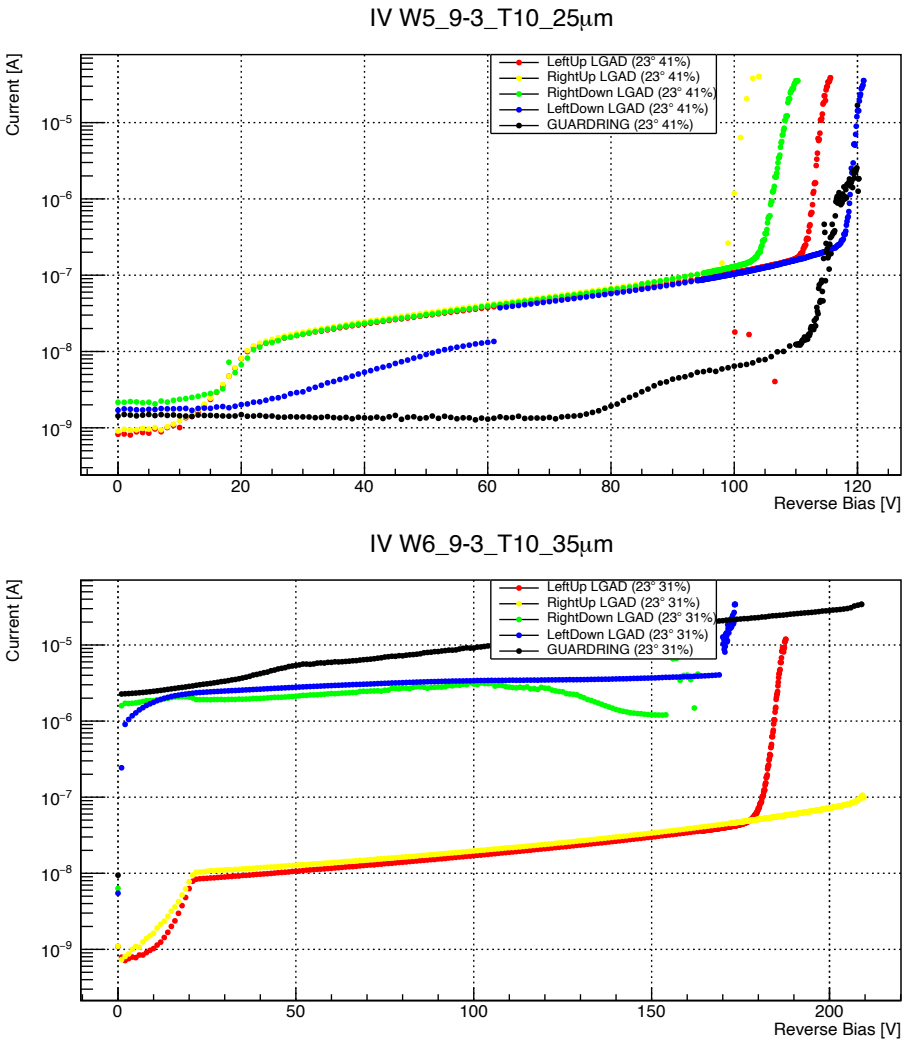

Figure 3.14: Example of measured IV characteristics of type10 matrices. In each graphic, five different IV are plotted: four corresponding to the pads and the black one corresponding to the biasing guard ring (GR). All the measurements were performed with a 4-needles setup. In the legend the temperature and the humidity at which each curve was measured are reported. The plot on the top is relative to the samples with the W5 wafer (25 μm), while the one on the bottom corresponds to W6 wafer (35 μm).

without amplification. The curves are reported in figure 3.16. The value of the current is of the same order of magnitude in the two samples, while the breakdown voltage has very different values, this is not strange since the two sensors belong to two different productions. In this case the change in the slope due to the depletion of the gain layer is lower that the precision of the instrument and so not visible.

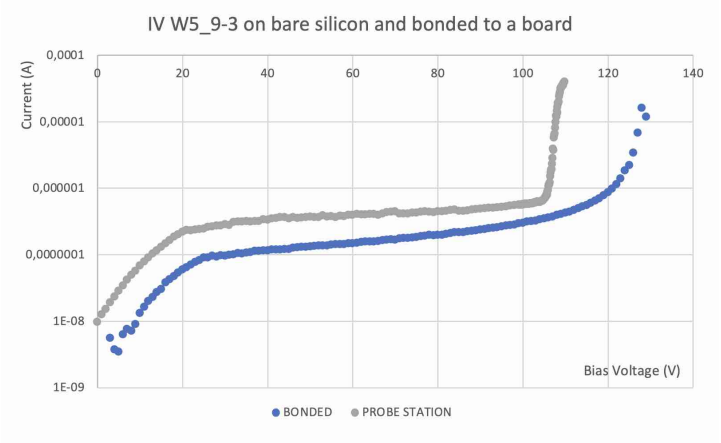

Figure 3.15: Comparison between IV characteristic of the the W5_9-3 LGAD measured on the bare sensor with the probe station and the one on sensor connected to the board.

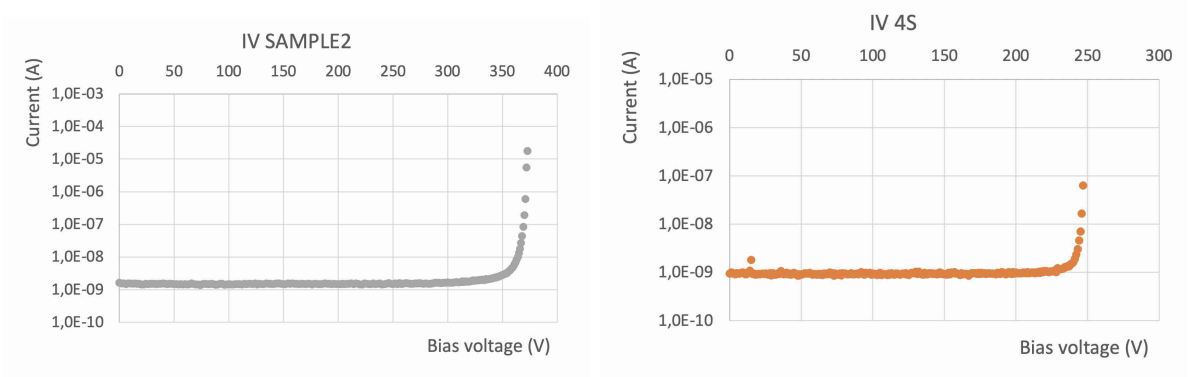

Figure 3.16: IV characteristics of the SAMPLE2 on the left and of the 4S matrix on the right.

A comparison between the measured IV curved for different sensor's thickness, 25, 35 and 50 μm, is shown in figure 3.17. As expected, the breakdown has a strong dependence on sensor thickness: for thicker sensors it is higher. Indeed, as shown in section B.2, a silicon sensor can be treated as a parallel plate capacitor and from the equation (B.20), it is clear that the same electric field is reached at lower voltages for smaller distances therefore, a smaller thickness corresponds to a smaller voltage applied to reach the junction breakdown.

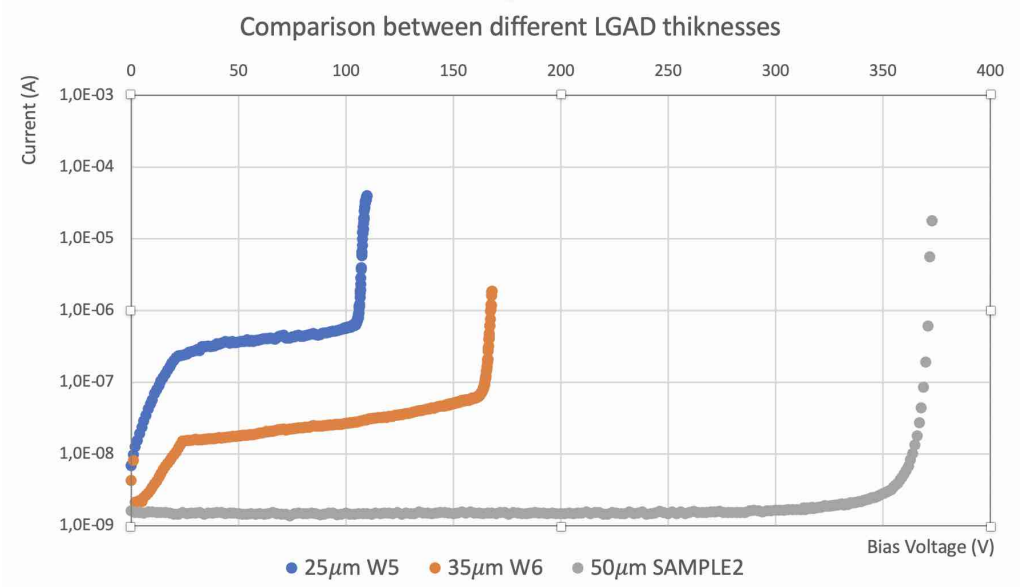

Figure 3.17: IV comparison between LGADs of different thicknesses. The measurements on the 25 and 35 μm-thick sensors are performed on bare silicon, while the SAMPLE2 was connected to a board.

3.2.2 CV characteristic

The CV characteristic is another important measurement for the sensors characterization. The value of the capacitance at different bias voltages can be used to extract the gain layer depletion voltage and the full depletion voltage. In addition, the CV shape is directly connected to the doping profile of the sensor, so a uniformity between sensors of same design is pivotal (when used in a large experiment).

3.2.2.1 Experimental setup

The measurement of the CV characteristics was performed through an impedance analyzer [48]. Also in this case the probe station was used, in order to connect the instrument's probes to the cathode and the anode of the sensors, through a pin on the top, in contact with the pad and the chuck in contact with the backplane. The experimental setup is shown in figure 3.18. In this case just one pin was directly connected to the LGAD, the other two, visible on the right, were used just to mantain the sensor in good contact with the chuck. The same setup, was used with the 50 μm sensors, except for the probe station, since in this case the impedance analyzer's probes were directly connected to the the board.

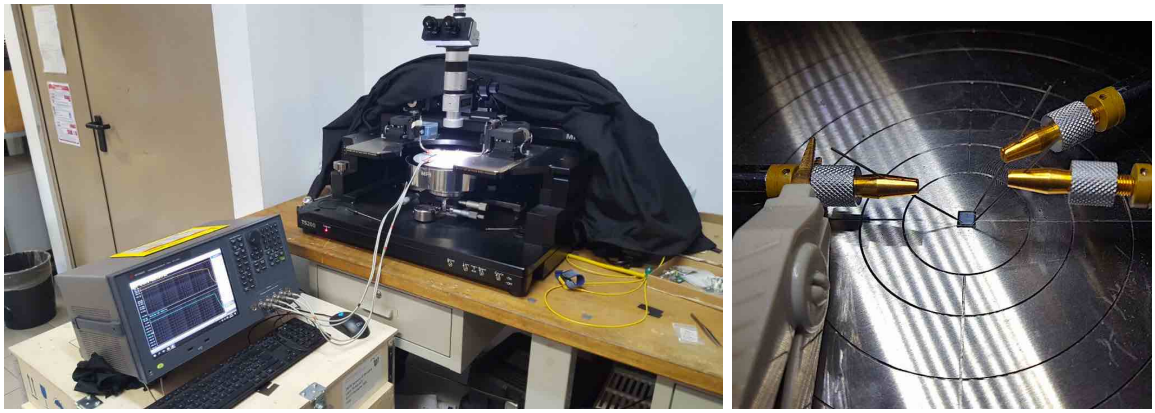

Figure 3.18: Experimental setup for the measurement of the capacitance-voltage characteristics composed by an impedance analyzer and the probe station (left), with a zoom on the sensor positioned on the chuck (right). The pin connected to the grey probe is the only one directly in touch with the LGAD, the other just apply a pressure on the sensor, and are positioned on the edges of the silicon structure.

3.2.2.2 Results

The CV analysis is done only on the 25 μm and 50 μm-thick LGADs, since the type inversion of the W6 wafer makes it impossible to perform this measurement and extract useful information. A first evaluation was done on the single 25 μm-thick LGADs, in order to see if there are differences between sensors belonging to the same wafer. A plot with this comparison is shown in figure 3.19 (left). All the curves have the expected behavior. In particular, two main regions can be identified: the first one, between 0 and $\sim$ 22 V, where the CV decreases slowly, is related to the depletion of the gain layer, and the second one, from $\sim$ 22 V, characterized by a substantial fall-off, is related to the depletion of the lightly doped bulk. The voltage at which the knee appears is the point in which the gain layer depletes (V_{GL}). The shape of the curve from 0 to this value allow to study the uniformity of the gain layer. In the case of the W5, the non-uniformity is very low. A zoom of the curves in the voltage range where the gain layer reaches the depletion, related to the position in which the gain layer ends, is reported in figure 3.19 (right). An offset of 0.4 V of this value is present, corresponding to just a 1.8% of non-uniformity of the doping profile.

After the V_{GL} point, the CV curve reaches an asymptotic behavior to the value of the capacitance of the sensor when it is fully depleted C_{FD}. This capacitance depends only on the sensor thickness and area:

$$C_{FD} = \frac{\epsilon A}{w} \tag{3.3}$$

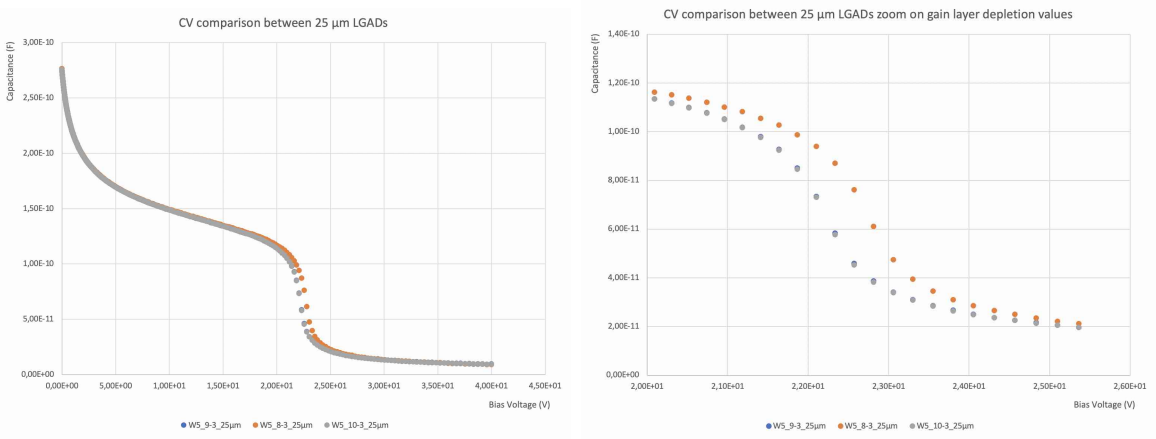

Figure 3.19: CV comparison between three LGAD sensors with the same thickness and area on the left, with a zoom in the voltage range where the gain layer reaches the depletion on the right. The measurements were done with a frequency of 20000 Hz, chosen on the base of past measurement done on other sensors.

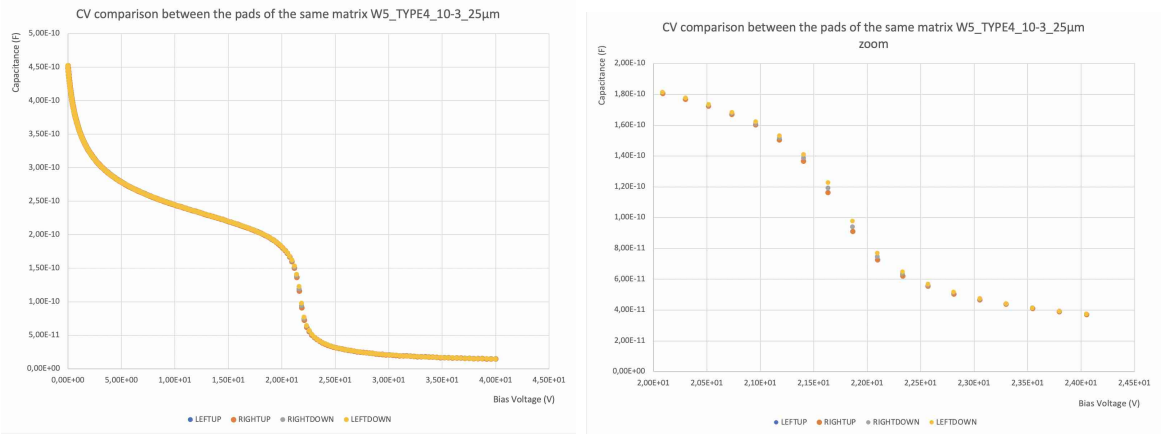

Figure 3.20: CV comparison between the pads of the same matrix W5_TYPE4_10-3_25μm on the left, with a zoom in the voltage range where the gain layer reaches the depletion on the right. The measurements were done with a frequency of 20000 Hz.

where ϵ is the product of the dielectric constant in the vacuum and the one of the silicon, A is the area of the detector, and w is its thickness. For the measured sensors, considering an area is 1×1 mm^2 and a thickness of 25 μm, the expected fully depletion capacitance is $C_{FD} \sim 4.1$ pF. From the figure a value of ~ 9.1 pF is reached, this can be compatible with the fact that the full depletion of the sensors is above 40 V (limit of the used impedance analyzer), so it is not visible from the plot.

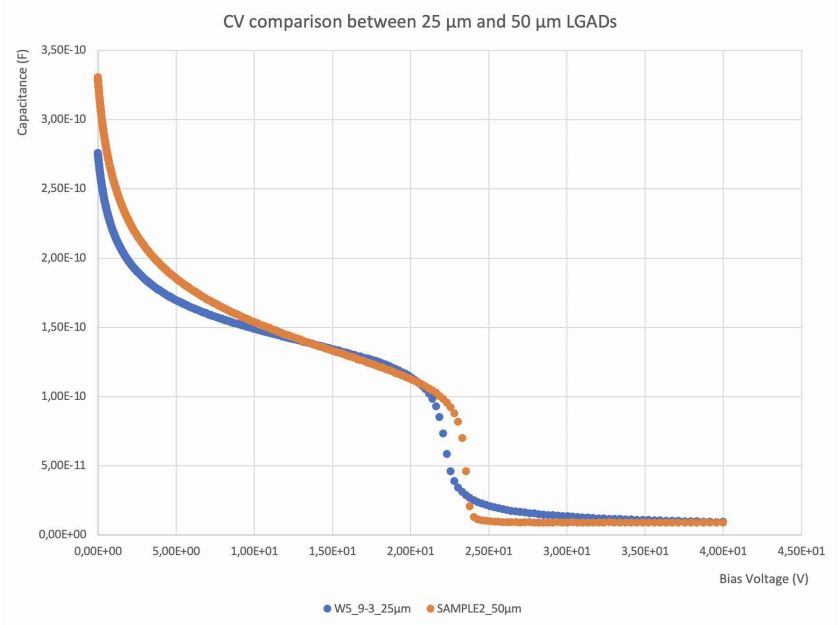

Figure 3.21: CV comparison between LGADs of different thicknesses. The measurements were done with a frequency of 20000 Hz for both the sensors.

Similar considerations were done on the pads of the same matrix. A comparison is reported in figure 3.20 for one of the sensors. As expected the four curves are just superimposed, and also from the zoom on the right it is visible that disuniformities the doping are totally negligible. In this case, because of the bigger area of the pads, an higher C_{FD} is expected, around 6.8 pF, but as before the full depletion is above the voltage range of the plot.

Finally, a comparison between 25 and 50 μm-thick LGADs is shown in figure 3.21. For both the sensor the voltage that corresponds to the depletion of the gain layer is the same. Since the two LGADs have the same area an half full depletion capacitance is expected for the 50 μm one. Contrary to the thinner sensor, the 50 μm LGAD is fully depleted before the 40 V, reaching the asymptotic value, correspondent to the C_{FD} of $\sim$ 2.1 pF, as expected.

3.3 Laser setup measurements

In this chapter all the measurements performed with the laser setup are presented. Preliminary studies were done on the sensors in order to evaluate the light-sensitive areas in terms of efficiency, uniformity of the response and edge effects. Through automatic scans of the sensor, the windows dimension and the diameter of the laser were extracted,

in order to be sure that the whole light of the laser enters the sensor, so that reliable evaluation in the comparison with the PIN can be done. After the evaluation of the gain of each sensor, preliminary studies on the time resolution were done.

3.3.1 Experimental setup

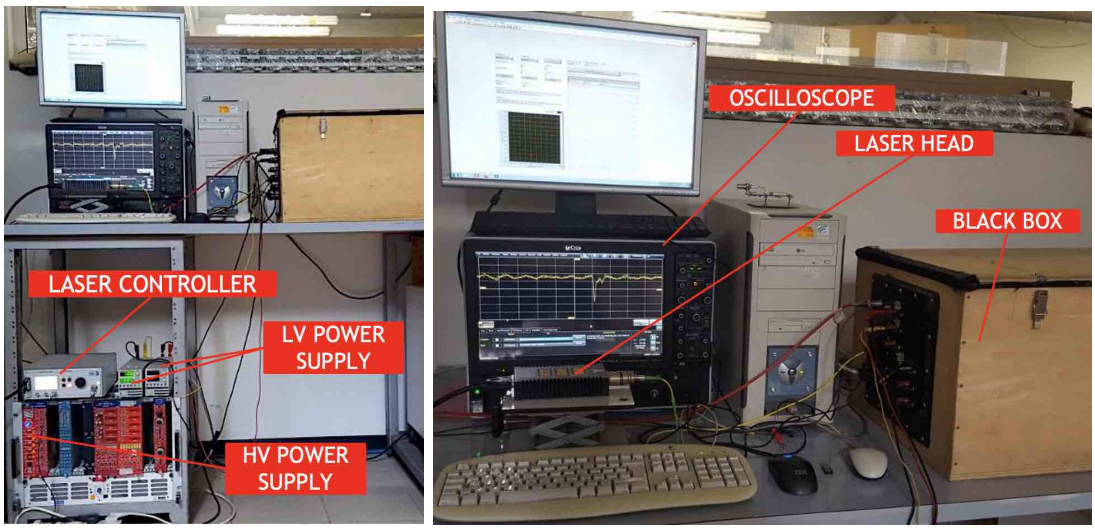

Figure 3.22: Laser measurements setup. On the table, it is possible to distinguish the oscilloscope, the computer with the LabVIEW program used to move the MPS. and the laser head, connected to its controller. The laser light enters the dark-box through the optical fiber (in yellow). All the power supplies are connected to the objects inside the box, by connections on the side in order to minimize the light coming from the outside.

The main elements of the setup are shown in figure 3.22. The light is provided by a picosecond pulsed laser with a wavelength of 1054 nm (PiLas PiL036XSM [49]) controlled by a EIG2000DX controller. The laser head is connected to a 1 meter single-mode optical fiber Thorlabs P3-980A-FC-1 which transmits the infrared photons right inside the black box where the LGAD is placed (figure 3.23).

Before reaching the sensor, the laser light is collimated and focused, by an optical combination of a collimator and a lens (Schafter & Kirchhoff 60FC-T-4-M40-54, Micro Focus Optics 13M-M40-54-S), placed on a manual moving support, which allows to move the two optical objects in the z-direction, with an accuracy of 20 μm. The distance between the lens and the sensor is important to find the correct focus of the micrometric laser spot. The board to which the LGAD is connected, is mounted on a two axes Standa 8MT167-25LS Micrometer Positioning Stages (MPS) [50], controlled by a LabVIEW program, from which it is possible to move the sensor in x and y directions with a

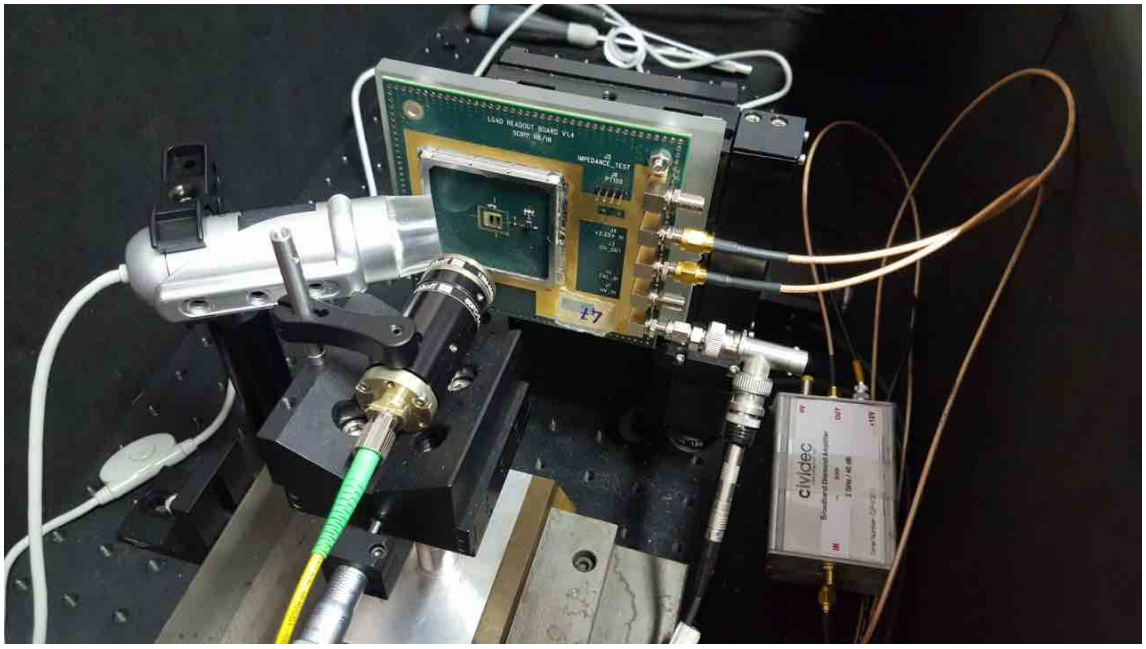

Figure 3.23: Laser setup components positioned inside the box. The board, on which the LGAD is placed, is attached to the MPS. The top and bottom SMU on the right bring an high voltage to the LGAD and low voltage (+ 2.25 V) to the board, while the central one, connects the output channel to a CIVIDEC amplifier, from which the amplified signal is brought outside the box, and arrive to the input channels of the oscilloscope. The single mode optical fiber enters in a micro focus optics placed on the manually controlled micro moving support, which allows movements in the z-direction. A camera is visible on the left, useful to have a first coarse positioning of the laser spot on the sensor.

micrometric precision, to reach the right position in which the spot of the laser is inside the active area of the sensor, or even set up an automatic scan of a given zone. In some cases to find the right point on the x-y plane, a camera (visible in figure) connected to the computer was used. The signal provided by the LGAD is then read out by a Teledyne LeCroy digital oscilloscope Wave-Master SDA 816Zi-A [51]. In order to have measurable signals, an additional amplifier is connected to the output of the board. Different kinds of amplifiers were used: CIVIDEC (visible in the figure, [52]), LEE39 [53] , and a Gali5 [54] The high voltage on the sensor is provided by a CAEN power supply module, while the amplifiers and when is necessary, also the board, are powered by two Z100-8-TDK-LAMBDA [55] power supplies, as shown in the figure.

3.3.2 Preliminary studies

Some preliminary tests can be done on the LGADs using the laser setup. Automatic scans in different zones of the sensors allow to evaluate the light-sensitive areas in terms of efficiency, uniformity of the response and edge effects. Since both sample 4S and new thin LGAD prototypes are metallized on all the surface, except for micrometric windows, it is of primary importance to know the dimensions of the windows, in order to be sure that the spot of the laser is entirely inside the windows, being confident that all the photons enter the silicon and are not reflected by the metallization. This is fundamental for the gain evaluation. Also the diameter of the laser spot can be estimated through an analysis of the scans taken between the active and metallized surfaces.

3.3.2.1 Uniformity of the light sensitive area and edge effects

To check the uniformity of the light-sensitive area and the pads edge effects, scans of the interested zones were performed.

The automatic scan is controlled through a LabVIEW program. After having found the center of the area in which the measurement must be performed, it is possible to choose the steps in which taking data in that area. The program is connected to the MPS, allowing an automatic change of the position and to the oscilloscope, which for each point measures the signal. For each step, all the output values are stored in a file, allowing a comprehensive data analysis.

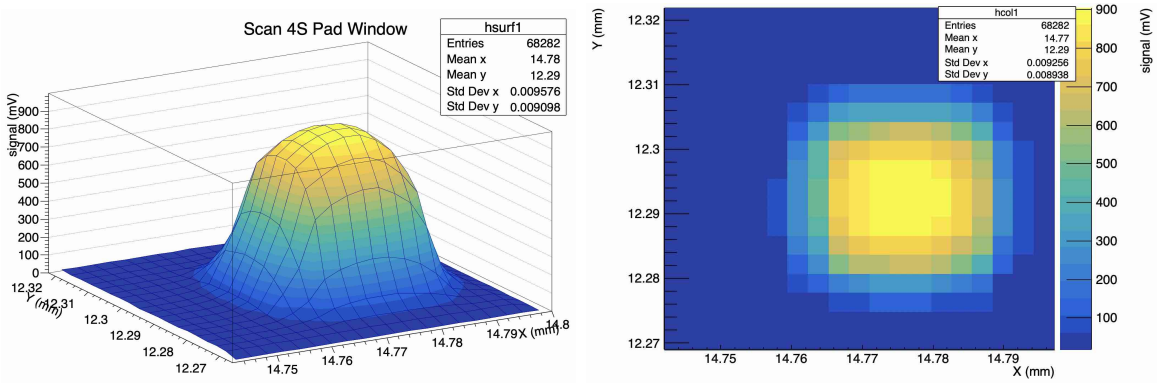

Figure 3.24: Laser scan of the 4S LGAD in the area containing the right-down window of the left-down matrix pad. A tridimensional view of the absolute value of the signals is shown at left and a bi-dimensional zoom on the windows at right. The measurement was performed with x and y steps of 3 μm and the signal was amplified of a factor 150 by a CIVIDEC amplifier.

The first evaluations were done on the 4S LGAD matrix. In this case, each of the four pads has two windows, one in the left-up and the other in the right-down parts.

Moreover, two additional windows are present between the left and right pads of each row. Figure 3.24, shows an example of the scan result of the area around one of the central windows. The scan was performed with x and y steps of 3 μm in the sorrounding area the right-down window of the left-down pad of the matrix. The plot on the left is a tridimensional view of the absolute value of the signals registered by the oscilloscope for each point, where the output was amplified by a factor 150 through a CIVIDEC amplifier, while on the right is shown a bi-dimensional zoom on the windows.

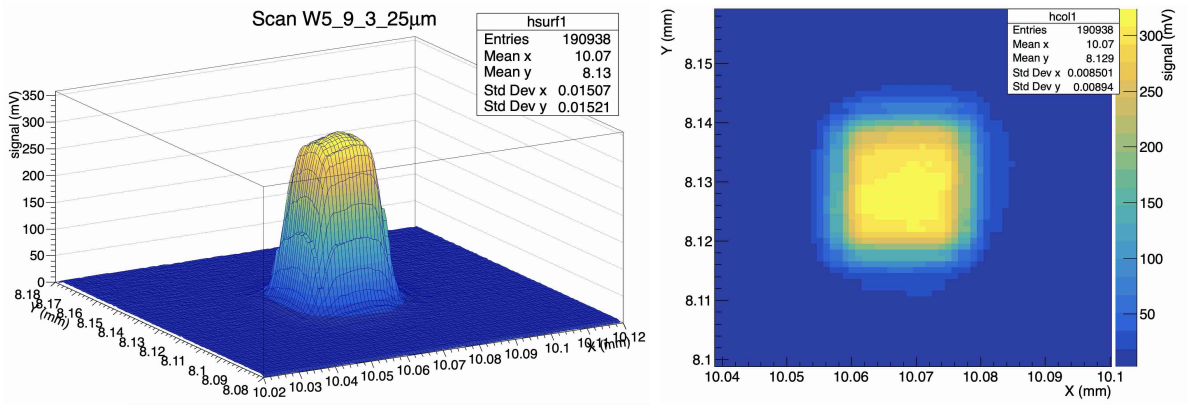

Figure 3.25: Laser scan of the W5_9-3_25μm LGAD in the area containing the central window of the pad. A tridimensional view of the absolute value of the signals is shown at left and a bi-dimensional zoom on the windows at right. The measurement was performed with x and y steps of 1 μm and the signal was amplified of a factor 11.1 given by the LEE39 amplifier and of an additional factor 20 by the board internal amplifier.

From the plots, it is possible to appreciate the transition between the non-metallized zone of the sensor pad and the laser blind area. The signal, passing from one to the other, decreases, until no signal is present, meaning that all the photons are stopped by the metallization. The transition is not sharp because of the finite size of the laser spot. The laser composition has a Gaussian distribution, where the core has the highest number of the photons and the tails are much less populated, so while moving to the covered area, the number of photons that enters the window rapidly decreases. However, in the center there is an area in which the magnitude of the signal is uniform, giving confidence that the dimensions of the laser spot is lower than the ones of the window, so that positioning it in the right point all the photons succeed entering the sensor (quantitative evaluations will be done in the next paragraph). The coordinates of the central point, useful for the gain and time resolution evaluations, are extracted from the plots on the right.

As for the 4S matrix, a scan of the central window of the W5_9-3_25μm prototype is reported in figure 3.25. The scan was performed in this case with smaller steps, of 1 μm on x and y in the central area of the sensor, and the output was amplified by a factor

11.1 through a LEE39 amplifier and by an additional factor 20 due to the board internal amplifier. In this case, having even smaller windows (see section 3.3.2.2), making a scan was of crucial importance to find the right point in which the windows were placed and also to evaluate if the spot of the laser was completely inside the non-covered area.

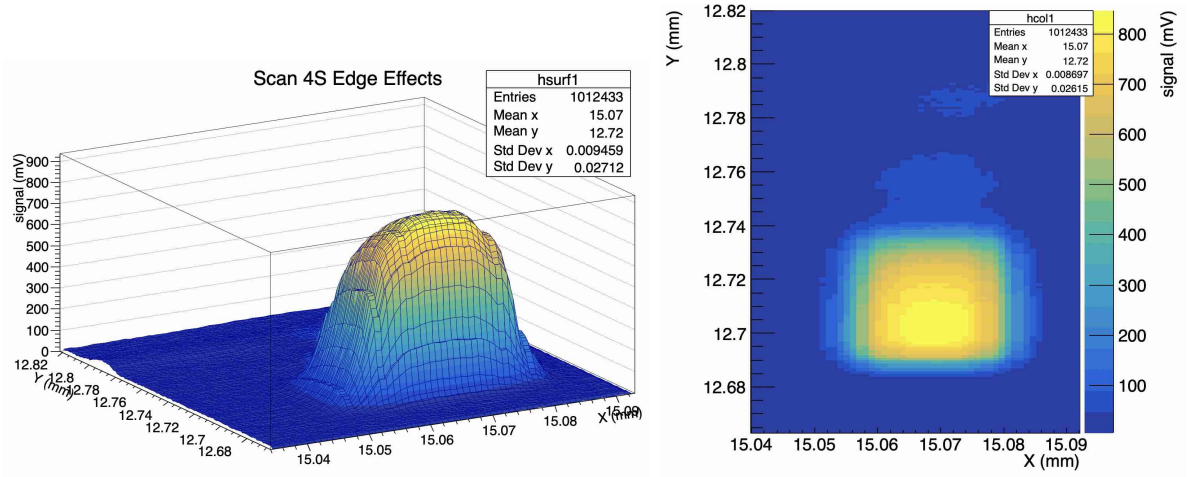

Figure 3.26: Laser scan of the 4S LGAD on the left side area of the inter-pad region between the two adjacent bottom pads. A tridimensional view of the absolute value of the signals is shown at left and a bi-dimensional zoom on the windows at right. The measurement was performed with x and y steps of 1 μm and the signal was amplified of a factor 150 by a CIVIDEC amplifier.

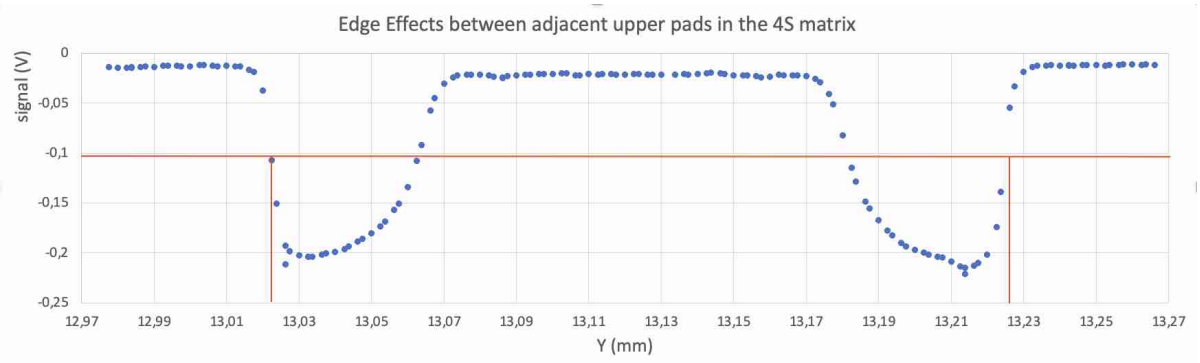

Figure 3.27: Vertical laser scan in the y-direction (with x coordinate fix in the position x = 15.07 mm) on the 4S LGAD in the area containing the inter-pad windows between adjacent pads in the upper row. The measurement was performed with y steps of 2 μm and the signal was not amplified.

An additional scan with a different goal was also done on the 4S matrix, on the left side of the inter-pad (IP) region between the two adjacent bottom pads. This window is appositely present to evaluate the edge effects, the inter-pad dead area. Two plots similar to the previous ones, are shown in figure 3.26. The measurement was performed with x and y steps of 1 μm and the signal was amplified like it was for the internal pad window, of a factor 150 by a CIVIDEC amplifier. In this case, the aperture is not squared, but rectangular. In addition, the signal is not maximum in the center. It has the highest values near the pad and it decreases going in the inter-pad region; some non-uniformities in the outermost part are visible.

Thanks to this window it is also possible to evaluate the dead area between the pads. This evaluation was done looking this time at the inter-pad windows in the upper row. Having the pads bonded together, just one output channel was used. A scan in the y-direction is shown in figure 3.27. The nominal value of the IP gap is defined as the distance between the multiplication region of adjacent pads. This value can be extracted considering the region between adjacent pads where the pulse height is below 50% of that in the central area of a pad [56]. Making this consideration, the extracted dead area results of 120 μm.

3.3.2.2 Determination of the windows dimensions and of the laser spot diameter

As previously said, in order to study the gain and the time resolution of the LGADs, it is necessary to know the exact value of the dimension of the windows and the diameter of the laser spot, when it is in a condition of focus, in order to be sure that all the light is reaching the sensitive area.

These two values can be extracted directly from the scan around the windows. Fixing one of the two coordinates of the scans, considering an infinitesimal spot, the signal on the window (negative) can be seen as a step function, with a negative constant value of the signal in the sensitive area and zero signal in the metallized area. Since the laser is not infinitesimal, but even when perfectly focused, has a certain dimension, the signal at the edges of the windows has a more smooth behavior. In particular, the laser spot, has a circular Gaussian-shaped intensity, with the maximum number of photons in the core and tails less populated. Considering both the behavior, the LGAD signal, passing along the transition zone between the metallization and the not-covered area and going back to the metallization on the other edge of the windows, is expected to follow the following function:

$$Signal = -\frac{A_1}{2}\left[1 + erf(\frac{x - x_{0_1}}{\sqrt{2}\sigma_{G_1}})\right] - \frac{A_2}{2}\left[1 - erf(\frac{x - x_{0_2}}{\sqrt{2}\sigma_{G_2}})\right] + Constant \qquad (3.4)$$

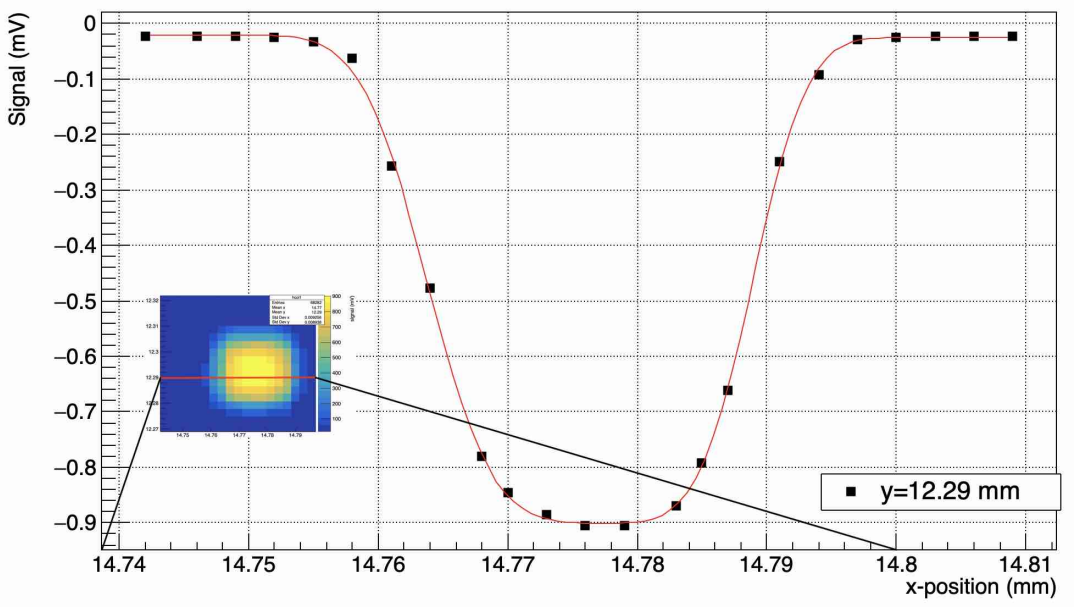

Figure 3.28: Horizontal scan carried out on the 4S LGAD in the area containing the right-down window of the left-down matrix pad with y coordinate fixed at y = 12.29 mm. The points are fitted with the function (3.4), in order to obtain the dimension of the window and the laser spot size. The measurement was performed with x steps of 3 μm and the signal was amplified of a factor 150 by a CIVIDEC amplifier.

This is the sum of two convolutions (error function) of step functions of amplitude A_1 and A_2, correspondent to the transition between metallized and not-covered area and a Gaussians of means x_{0_1} and x_{0_2} and sigmas σ_{G_1} and σ_{G_2}, correspondent to the laser spot intensity distribution. The fits are visible in figure 3.28 and 3.29, respectively for the windows of the 4S and W5_9-3_25μm LGADs, considered for the measurements of the time resolution in the following section. In table 3.3 the sigmas of the laser spot dimensions extracted from each side of the window, fitting the data with the function (3.4) are reported together with the extracted dimensions of the windows.

The size of the spot is considered as the Full Width Half Maximum (FWHM = 2.3548 σ) of the σ_{G_1} and σ_{G_2}. Since LGADs need a big number of photons to produce an appreciable signal, and so they are sensible only to the most intense core of the laser spot, in the limits of the errors, the σ_G can be considered always the same for different laser light intensities. Otherwise, in very intense light conditions the dimensions of the spot extracted by this fit can be different by the actual total spot size, affected by more populated tails of the Gaussian. However, having considered twice the extracted σ_G, and taking the worst case, the spot diameter can be considered with a good confidence level to be lower than 8.5 μm and consequently lower than the dimensions of the windows for

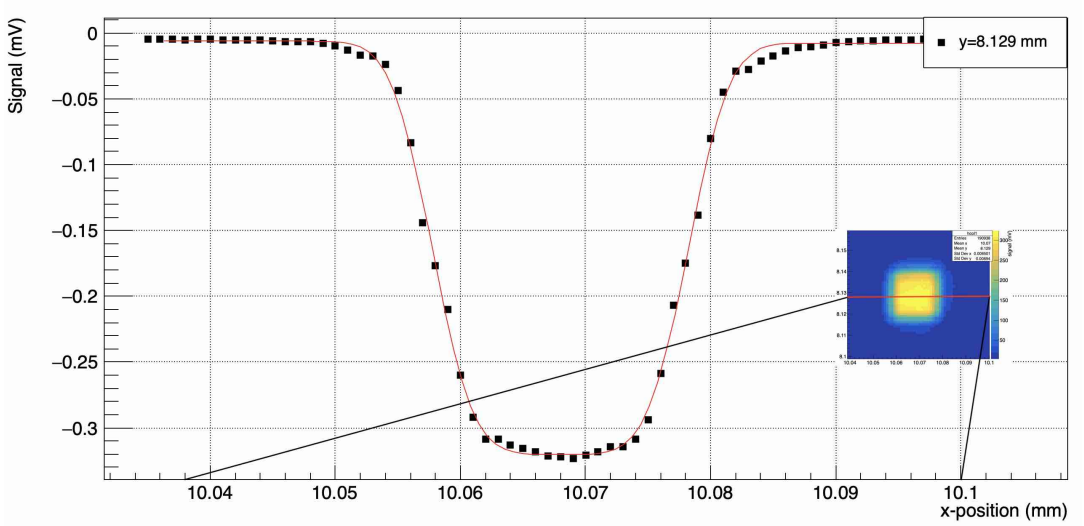

Figure 3.29: Horizontal scan carried out on the W5_9-3_25μm LGAD in the area containing the central window of the pad, with y coordinate fixed at y = 8.129 mm. The points are fitted with the function (3.4), in order to obtain the dimension of the window and the laser spot size. The measurement was performed with x steps of 1 μm and the signal was amplified of a factor 11.1 given by the LEE39 amplifier and of an additional factor 20 by the board internal amplifier.

both the analyzed sensors, allowing to perform all the measurements, being sure that the light totally enters the sensor.

This kind of measurements were not performed on the SAMPLE2 LGAD, since in that case, the non-metallized area is very big in respect to the dimensions of the spot, giving us the certainty to collect all the photons.

3.3.3 Timing performances

The study of the time resolution was performed on three different LGADs: the 50 μm-thick 4S_50μm matrix and SAMPLE2_50μm and the 25μm-thick W5_9-3_25μm. Since the aim is to make these studies simulating the conditions in which the sensors are traversed by a MIP, a laser with an Infra-Red (IR) light (1054 nm) was used. This is because, as seen in the previous chapter, a MIP can traverse all the sensor, producing about 73 electron-hole pairs for μm along its path. IR light can penetrate several tens of μm interacting in the silicon after having traversed a path that each time is different, producing pairs at different depths, simulating in this manner the behavior of a MIP.

In order to get an estimation of the sensor timing capability, the time resolution has been assessed by means of the same laboratory setup described in section 3.3.1. The

	W5_9-3_25μm	**4S**
Window dimension	20.5 $\pm$ 0.1 μm	25.2 $\pm$ 0.2 μm
σ_{G_1}	2.6 $\pm$ 0.1 μm	3.3 $\pm$ 0.1 μm
σ_{G_2}	2.6 $\pm$ 0.1 μm	3.9 $\pm$ 0.1 μm
FWHM($\sigma_{G_{mean}}$)	6.1 $\pm$ 0.2 μm	8.5 $\pm$ 0.2 μm

Table 3.3: Dimensions of the windows and sigmas of the laser spot diameter, for each side, extracted fitting the data with the function (3.4). The total dimension of the spot size is evaluated as twice the mean of the σ_{G_1} and σ_{G_2}.

sensor and the amplifier was in turn changed.

3.3.3.1 Gain evaluation

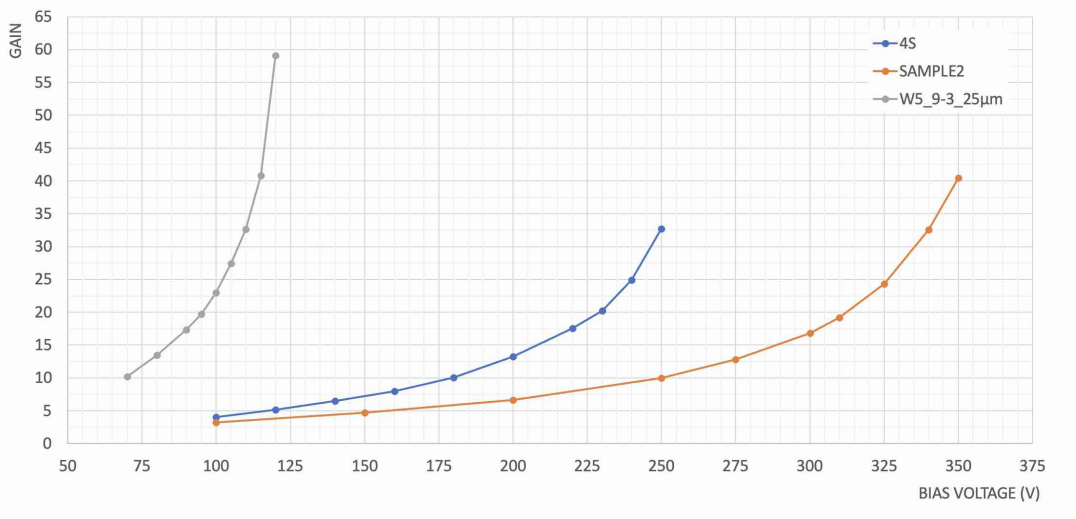

Figure 3.30: Multiplication gain plotted in function of the applied bias voltage, calculated as the ratio between the charge produced by the LGAD sample and that of the reference p-in-n diode for the three considered sensors.

The first measurement that was performed is the gain of the sensors under consideration. The gain of a LGAD can provide many useful information, since it is related to all the other parameters and in particular to the time resolution at the bias voltage applied to the detector. Knowing the relation with this last parameter is important to decide which is the best voltage in which to operate the LGADs.

The evaluation of the gain was performed by taking into account, for each LGAD,

a reference p-in-n diode with the same thickness, but without the multiplication layer. The measurements were done on the LGAD and the PIN with the same light conditions and focusing of the spot. So, for each couple, after having chosen a given frequency and tune of the laser light the measurement was performed on both the elements without changing the parameters, always having the spot well focalized and totally inside the windows, in order to be sure to send on both the same number of photons and obtain reliable values of the gain, not affected by a different amount of light that enters the sensor. This is the reason why the studies on the dimensions of the windows and of the spot laser made in the previous section were so important.

In particular, to obtain the gain for the 50 μm LGADs, the PIN used as reference sensor with the same thickness, but without the gain layer, is the HPK 5S sample. All the measurements were done with the boards connected to the same CIVIDEC amplifier (150 amplification factor), and in a light condition given by the laser at 100 Hz and 0% tune (without attenuation) of the light. While the measurements for the W5_9-3_25μm PIN-LGAD couple were done with the PIN connected to a CIVIDEC amplifier; the only in this case, the LGAD was not connected to amplifiers, only the amplification of the board was present. A multiplication factor of 167 (found with a waveform generator and empirically validated at different bias voltage by measuring the charge with and without the amplifier in the allowed range) given by the CIVIDEC was taken into account in the calculations. Both the sensors were in addition connected to the same board amplifier.

The gain was calculated as the ratio between the charge produced by the LGAD sample and that of the reference p-in-n diode:

$$\text{Gain} = \frac{\text{mean charge of the LGAD}}{\text{mean charge in the reference PIN (without gain)}} \tag{3.5}$$

The mean charge was found as the difference between the area subtended by the signal and the area subtended by the baseline (with a time interval equal to the one used for the signal). In the calculation also the internal impedance of the oscilloscope (R = 50 Ω) and the eventual gain ($G_{amplifier}$) of the amplifier connected to the output of the sensors:

$$\text{Charge} = \frac{A_{signal} - A_{baseline}}{R \cdot G_{amplifier}} \tag{3.6}$$

The gain curves in function of the bias voltage, calculated as explained are reported for the three different sensors in figure 3.30. As visible, the curves show an exponential behavior as approaching the breakdown voltage. While the gain for the 50 μm sensors remains quite low till the reaching of V_{BD}, the one of the W5_9-3_25μm reaches higher values already at lower voltages.

SENSOR	AMPLIFIER	AMPLIFICATION
LGAD 4S_50μm	CIVIDEC	150
LGAD SAMPLE2_50μm	CIVIDEC	150
PIN 5S	CIVIDEC	150
LGAD W5_9-3	LEE39 + BOARD	(11.1±2.2)+(20±0.2)
PIN W5_9-3	CIVIDEC + BOARD	167+(20±0.2)

Table 3.4: Amplifiers connected to the different LGADs and PINs, used during all the laser measurements, with the respective amplification factors.

3.3.3.2 Measurements and data analysis

Setup parameters and data taking

The study of the timing performances was carried out with the laser light intensity tuned to reproduce the energy deposition of a MIP in the detector. This can be done through both the laser controller, which gives the possibility to change the tune, passing from a condition of maximum light intensity, to a fully attenuation or by mechanically moving the optics of the laser head, reducing the amount of light entering the single-mode optical fiber. In particular, the laser was regulated on the sensors in a way that the charge on the PIN results 0.5 fC and 0.2 fC for the 50 and 25 μm-thick ones, respectively, that are the value expected by the passage of a MIP. This regulation was done changing the laser tune, while exploiting the math functions of the oscilloscope, which allowed to do a real time measurement and computation of the value of $A_{signal} - A_{baseline}$ calculated by the formula (3.6), considering the expected charge and the values of the used amplifiers for each sensor. The considered values and the amplifiers, used to perform all the timing measurements and also to calculate the $A_{signal} - A_{baseline}$, are reported in table 3.4.

All the data were taken using the full bandwidth of the oscilloscope, that for the Wave-Master SDA 816Zi-A is of 16GHz, in order to have the possibility to reduce the bandwidth in a second time during the analysis way, by replacing each point of the signal, with the average of N points before and after. The trigger for the timing evaluations is provided by the power supply of the laser.

Before taking the data, the laser was precisely focused. Scans of the windows area, like the ones shown in section 3.3.2.1, were done in order to measure the spot size and the precise coordinates of the center of the windows.

About 15000 events for each chosen voltage value were taken. In particular, through the oscilloscope, the full waveform of the signal for each event was recorded.

Signal cuts

The typical signal of an LGAD is reported in figure 3.31. In this specific example, it is visible that the waveform is relatively fast and short, with a duration of about 1.5

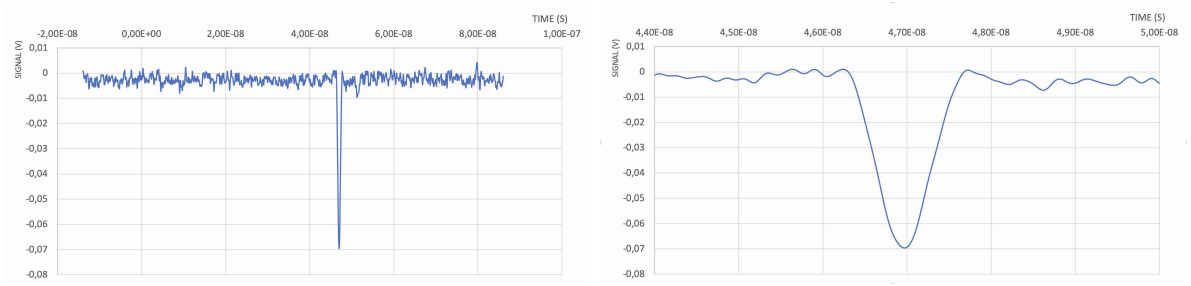

Figure 3.31: Typical waveform of LGAD signal recorded by the oscilloscope (left) and zoom on the signal peak (right). This specific one is the output of W5_9-3_25μm with a bias voltage of 95 V, in the light condition used to simulate a MIP, amplified of a factor 11.1 given by the LEE39 amplifier and of an additional factor 20 by the board internal amplifier.

ns (excluding the second peak about 1 ns after the first one, which is probably related from artifacts of the setup).

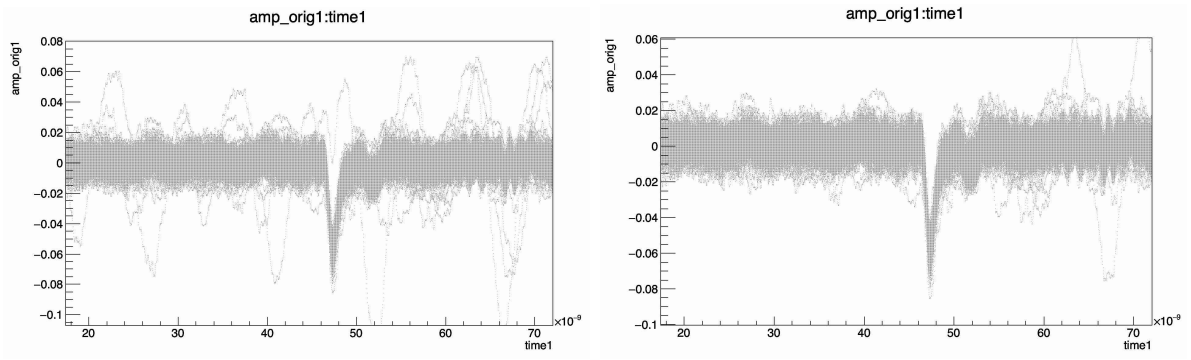

Figure 3.32: Example of a signal selection on the SAMPLE2_50μm LGAD. On the left all the events recorded by the oscilloscope on the base of the trigger condition and on the right the selected events, after the application of the cuts described in the text.

Considering this waveform some cuts on the data were carried out in order to remove all the noise events.

The first cut was performed on the maximum amplitude of the signal. In particular, all the signals that didn't exceeded a minimum threshold, or were higher than a maximum one, (where the two thresholds were selected for each value of the bias voltage, looking at the distribution of the maximum amplitude, for the whole taken waveforms) were excluded. This selection was done in a time window of $\pm$ 0.75 ns, around the maximum amplitude of the signal.

In order to remove also the noise events with an amplitude comparable to the one

of the signal, a second cut was done on the time, asking that the signal reaches a given amolitude threshold after a given time.

Finally, a last cut was done on the noise, to remove in particular the large electronic noise events, removing all the signals that exceeded a given threshold in both the positive and negative amplitudes. In this case, the cut was done for all the values of time, except for the ones inside the previously chosen signal window.

An example of signals surviving the applied cuts is shown in figure 3.32: the plot on the left contains all the events recorded by the oscilloscope on the base of the trigger condition, while the right one contains only the selected events, after the application of the described cuts.

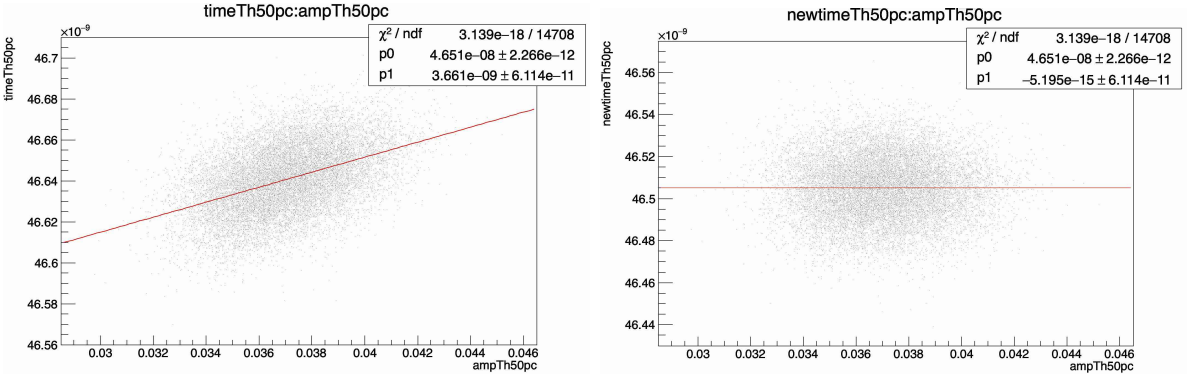

Figure 3.33: Time slewing correction example for the W5_9-3_25μm LGAD. The passage time of the CFD 50% threshold in function of the amplitude of the signal is plotted, before and after the application of the correction. A linear fit of the points, with the relative parameters, is shown.

3.3.3.3 Time resolution

The time resolution was evaluated applying offline the Constant Fraction Discrimination (CFD) technique [57]. This consists in considering the time in which the signal passes a certain threshold given by a percentage of the maximum signal amplitude, which has a Gaussian distribution, so that the time resolution of the detector is the sigma of this Gaussian. In addition, to eventually remove residual correlation between the signal amplitude and the threshold crossing time, the time measurements were corrected for the time slewing effect. Two plots showing the correlation between the charge and time of the W5_9-3_25μm, before and after the time slewing correction, are reported, as an example, in figure 3.33.

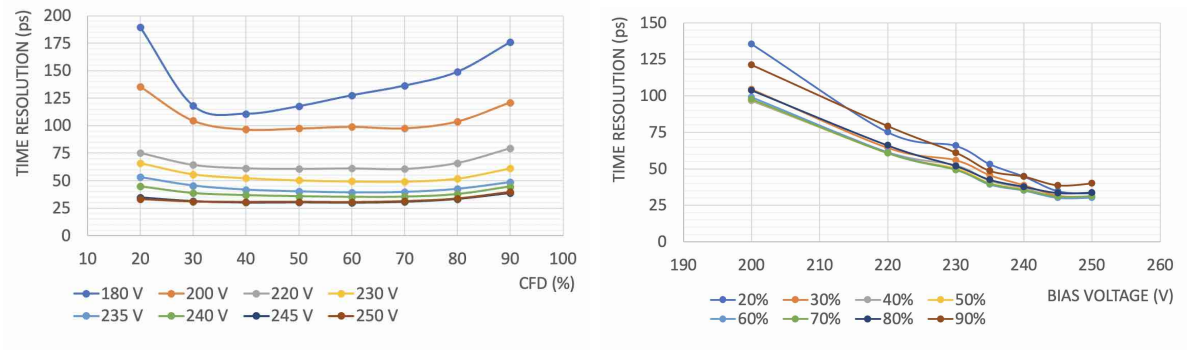

Figure 3.34: Time resolution of 4S_50μm LGAD versus the CFD for different values of applied voltage (left) and time resolution in function of different applied bias voltage, for each CFD value (right). The time resolution improves for higher applied bias voltages and for medium (30-70%) CFD percentages.

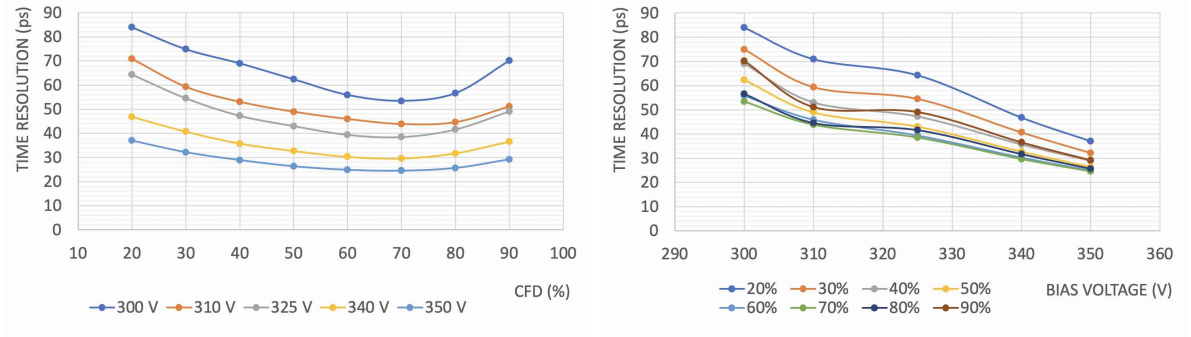

Figure 3.35: Time resolution of SAMPLE2_50μm LGAD versus the CFD for different values of applied voltage (left) and time resolution in function of different applied bias voltage, for each CFD value (right). The time resolution improves for higher applied bias voltages and for medium (30-70%) CFD percentages.

The final time resolution of the three considered LGADs have been studied for several values of the CFD for different applied bias voltage. The fraction was scanned at steps of 10% from 20 to 90% of the amplitude, and the optimal value was then taken.

In figures 3.34 - 3.36 (left) the time resolution versus the CFD for the detectors under test is reported, for different values of applied voltage. At lower and higher values of the CFD the time resolution is worse. In the low region, this is due to the higher contribution of jitter noise, while, at high ones it is related to both jitter and Landau contributions. The worsening at higher CFD is more evident for the 50 μm-thick sensors. This was expected since the Landau noise is larger for thicker detectors.

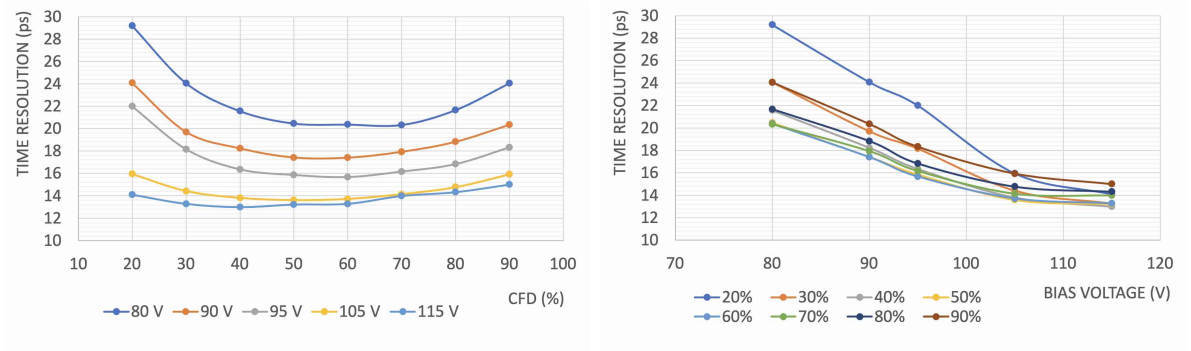

Figure 3.36: Time resolution of W5_9-3_25μm LGAD versus the CFD for different values of applied voltage (left) and time resolution in function of different applied bias voltage, for each CFD value (right). The time resolution improves for higher applied bias voltages and for medium (30-70%) CFD percentages.

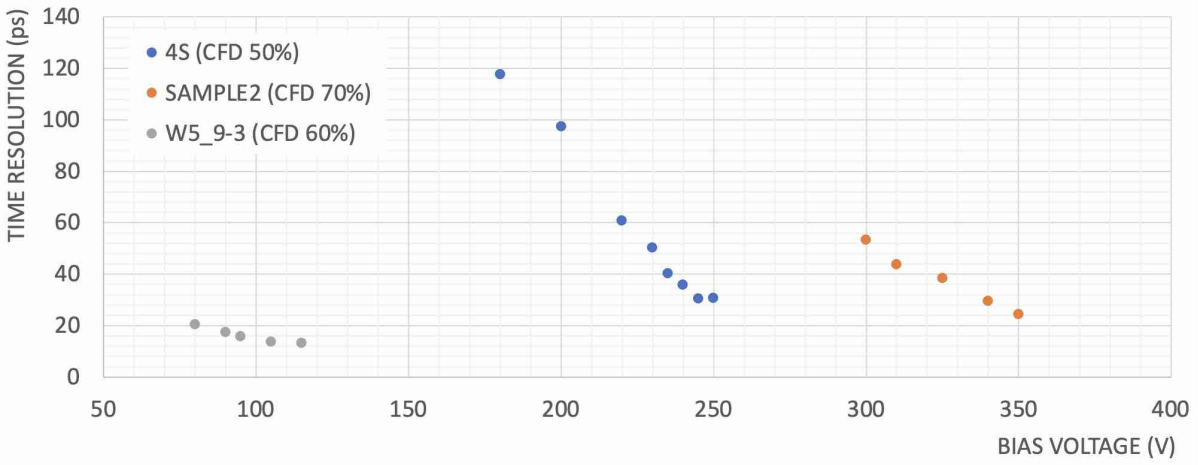

Figure 3.37: Time resolution as a function of different applied bias voltage, choosing the best CFD value for each considered LGAD.

While on the right, the time resolution is plotted as a function of different applied bias voltage, for each CFD value. As expected, for higher voltage, the time resolution improves. This is because to each applied voltage, corresponds a value of the gain, characteristic of each sensor. The time resolution has a strong dependency on the gain. In particular, for the laser measurement the evaluations can be done only for reasonable values of the gain, since at high value the Landau effect, differently to what happens with particles, decreases, resulting in time resolution much better than in the particle case that we want to simulate.

4S_50µm (CFD 50%)		SAMPLE2_50µm (CFD 70%)		W5_9-3_25µm (CFD 60%)	
V_{bias} (V)	σ (ps)	V_{bias} (V)	σ (ps)	V_{bias} (V)	σ (ps)
180	117,7	300	53,4	80	20,4
200	97,4	310	43,8	90	17,4
220	60,7	325	38,5	95	15,7
230	50,3	340	29,6	105	13,7
235	40,2	350	24,5	115	13,3
240	35,8				
245	30,4				
250	30,6				

Table 3.5: Time resolution as a function function of different applied bias voltage, choosing the best CFD value for each considered LGAD.

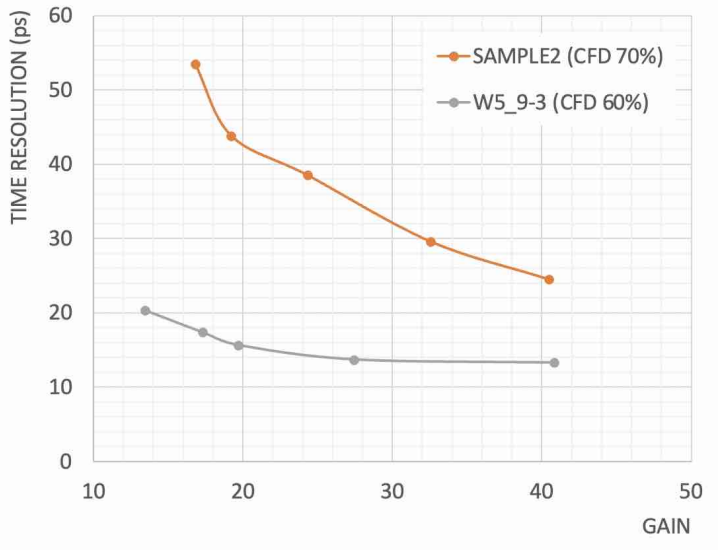

SAMPLE2 (CFD 70%)		W5_9-3_25µm (CFD 60%)	
Gain	σ (ps)	Gain	σ (ps)
16,8	53,4	13,5	20,4
19,2	43,8	17,3	17,4
24,3	38,5	19,7	15,7
32,5	29,6	27,4	13,7
40,5	24,5	40,8	13,3

Figure 3.38: Time resolution comparison between 25 and 50 μm-thick LGADs, as a function of the calculated gain. The resolution improves with the increasing of the gain and the decreasing of the detector thickness.

From these plots, the best CFD value, i.e. the one that minimizes the time resolution, was extracted; as a consequence, for each detector and each applied bias voltage, just one value of time resolution is considered. A comparison between the different sensors is shown in figure 3.37 and the numeric values are reported in table 3.5.

A last comparison between 50 and 25 μm, taking into account, respectively, the SAMPLE2_50μm and the W5_9-3_25μm (produced by the same foundry) is shown in figure 3.38. The time resolution, in this case, is plotted in function of the calculated gain. The resolution largely improves with the increasing of the gain. Moreover, it can

be noticed a better time resolution for thinner detectors, for all the values of the gain.

The measurements on the sensors of the same thickness of 50μm, also having different doping concentrations and appertaining to different productions, showed results that are comparable and in particular both have a resolution better than 50 ps for gains higher than 20, reaching values around 30 ps for a gain 30. The 25 μm LGAD instead, shows a time resolution better than 16 ps already for a gain 20, reaching nearly 13 ps for a gain 30.

Conclusions

In this work, a detailed characterization, and preliminary performances study of the first very thin LGAD prototypes produced by FBK were performed.

A total of 18 sensors with thicknesses of 25 μm and 35 μm were characterized, both single channel and matrices, with different inter-pad design, and compared with sensor with the same design but without a gain layer (PIN). In addition, two 50 μm-thick prototypes were also tested in order to have a comparison with the thinner ones.

The characterization that was performed initially on the bare silicon, using a probe station, included the measurement of the Current-Voltage (IV) and Capacitance-Voltage (CV) curves.

Two important values were extracted from the IV curves: the voltage at which the gain layer depletes, around 22 V for both the thicknesses, and the breakdown voltage, useful to know the range in which the sensor can be operated. A comparison between the measured IV curved for different sensor's thickness, 25, 35 and 50 μm, showed the breakdown has a strong dependence on sensor thickness, being higher for thicker sensors, as foreseen. In the case of the matrices, the IV characteristics gave useful information to evaluate the different inter-pad configurations. The main observation is related to the measurements with a floating pad, which highlighted that the design with the biasing ring internal to the pads makes the sensor reaching a more uniform internal electric field also when not all the pads are powered.

The value of the capacitance at different bias voltages was instead used to extract the gain layer depletion voltage and the full depletion of the sensor and to test the uniformity between sensors with the same design. The CV analysis was done only on the 25 and 50 μm-thick LGADs, since the type-inversion of the W6 wafer makes it impossible to perform this measurement. For both the sensors the depletion of the gain layer is reached at ~ 22 V, as expected from the IV measurement, while the full depletion is reached at lower voltage for the thicker sensors. Comparisons between LGADs of the same thickness, as well as the ones done on the pads of each matrix, showed a totally negligible non-uniformity in the doping profiles.

Following the characterization, preliminary studies were performed thanks to a laser setup. Automatic scans in different zones of the sensors allowed to evaluate the light-sensitive areas in terms of efficiency, uniformity of the response and edge effects. The

dimensions of the windows were extracted for each sensor, in addition to the laser spot size, that was lower than 8.5 μm for all the measurements, giving the confidence that all the light entered the sensor, allowing to do reliable gain and timing evaluation.

Finally, after the measurement of the gain for each sensor, the time resolution was studied for three different LGADs: two 50μm-thick sensor and one 25 μm-thick one. The study of the timing performances was carried out with the laser light intensity tuned to reproduce the energy deposition of a MIP in the detector. The time resolution was evaluated applying the Constant Fraction Discrimination (CFD) technique, obtaining the value for several percentages of the CFD for different applied bias voltage and choosing the best one.

The results for both the 50 μm-thik LGADs are comparable with the ones expected from previous measurements and in particular both shown a resolution better than 50 ps for gains higher than 20, reaching values around 30 ps for a gain 30. The 25 μm-thick LGAD instead, shows a time resolution better than 16 ps already for a gain 20, reaching nearly 13 ps for a gain 30.

Although still preliminary, these results are very promising. If a validation will be provided by the beam tests scheduled at CERN beam facilities in November 2021, where these thin LGAD prototypes will be tested using charged particles, 25 μm-thick sensors could be a very good candidate for the timing layers of ALICE 3 experiment.

Appendix A

Solid state detectors working principle

A.1 Crystals and Electronic Band Model

To be used as particle detectors, semiconductor materials in the form of high-purity crystals are required. Crystals are lattices in which the atoms are organized in a predictable periodic pattern. The primordial cell is the smallest arrangement of atoms that may be repeated to create the whole crystal, and its dimension is determined by the lattice constant that governs the periodicity. While electrons in single atoms have distinct energy levels, atoms placed in a lattice structure can affect each other, causing their electrons' energy levels to divide into states that differ only by a tiny amount of energy owing to mutual interactions. The permitted energy levels are then organized into a valence and a conduction band, separated by a forbidden gap (E_g). The size of this gap is determined by the chemical bonding in the material and for the silicon, at ambient temperature, it has a value of about $E_g \sim 1.12$ eV. This value corresponds to the minimum amount of energy that is necessary to break a covalent bond and excite an electron from the valence to the conduction band.

For a semiconductor, at T = 0 K, the valence band is completely occupied, while the conduction band is empty, so the semiconductor behaves like an insulator, showing no electrical conductivity. At higher temperatures instead, thermal vibrations may break the covalent bond and a valence electron can migrate in the conduction band, leaving a hole in the valence band. This electron-hole pair is then available for conduction. In particular, the concentration of electrons in the conduction band is given by

$$n = \int_{E_c}^{\infty} g_e(E) f(E) dE \tag{A.1}$$

where g_e(E) is the density of the states of the conduction band and E_c is its minimum energy level, while f(E) is the Fermi-Dirac distribution. Both electrons and holes are,

in fact, subjected to the Fermi-Dirac distribution

$$f(E) = \frac{1}{1 + e^{(E-E_F)/kT}} \tag{A.2}$$

with E_F being the Fermi energy, k the Botlzmann constant.

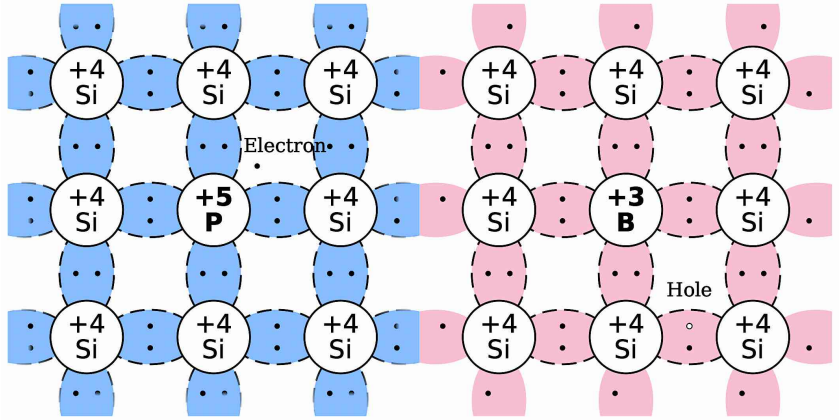

(a) N-type silicon, doped with phosphorus. **(b)** P-type silicon, doped with boron.

Figure A.1: Schematic bond pictures of the lattice structure of (a) n-type silicon with donor (phosphorus) and (b) p-type silicon with acceptor (boron).

In an analogous way the concentration of the holes p is calculated by the integral from zero to the maximum energy level of the valence band:

$$p = \int_0^{E_V} g_h(E) f(E) dE \tag{A.3}$$

being $g_h(E)$ the density of the states in the valence band.

Integrating the equations (A.1) and (A.3) the concentration for electrons and holes results

$$n = 2\left(\frac{m_n kT}{\hbar}\right)^{3/2} e^{-(E_C-E_F)/kT} = N_C e^{-(E_C-E_F)/kT} \tag{A.4}$$

$$p = 2\left(\frac{m_p kT}{\hbar}\right)^{3/2} e^{-(E_F-E_V)/kT} = N_V e^{-(E_F-E_V)/kT} \tag{A.5}$$

where N_C and N_V are the effective density of states in the conduction and in the valence bands. Due to charge conservation the number of electrons and holes, and

therefore their density, is equal. The intrinsic charge carrier density n_i is so related to the densities from the relation [58]:

$$np = {n_i}^2 = N_C N_V e^{-E_g/kT}. \tag{A.6}$$

The conductivity σ and resistivity ρ of a certain material, with a mobility μ_e and μ_h of electrons and holes respectively, is given by:

$$\sigma = \frac{1}{\rho} = e n_i (\mu_e + \mu_h) \tag{A.7}$$

In particular, at room temperature (about 300 K), intrinsic charge carrier density in the silicon, using the (A.6) results of $1.5 \cdot 10^{10}$ cm^{-3} and the intrinsic resistivity, inserting $\mu_e = 1350$ cm^{2}V^{-1}s^{-1} and $\mu_h = 480$ cm^{2}V^{-1}s^{-1} in the (**??**), is of about 230 KΩ cm [59]. This make this semiconductor one of the few only suitable to be operated without cooling and so one of the most used in HEP and by the industries.

In order to detect crossing charged particles, however, it is necessary that the charge deposited in the silicon by ionization is clearly distinguishable from the amount of free carriers originating from thermal effects (noise). Considering, for example, an intrinsic silicon detector of thickness d = 300 μm and area A = 1 cm^2 at the temperature of 300 K, the amount of free carriers due to thermal effects, can be expressed as

$$noise = n_i dA \sim 4.35 \cdot 10^8 \ e^- h^+ pairs \tag{A.8}$$

while the expected signal of a MIP (see section B.1.1), considering its energy loss for path length unit in silicon of $dE/dx = 3.87$ MeV/cm and, the mean energy needed for producing an electron-hole pair in silicon is $I_0 = 3.62$ eV, is

$$\frac{dE/dx \cdot d}{I_0} \sim 3.2 \cdot 10^4 \ e^- h^+ pairs \tag{A.9}$$

which is four orders of magnitude lower than the noise. As a consequence, intrinsic silicon semiconductors cannot be used for particle detection.

In order to reduce the noise, controlled impurities (so called dopants) are artificially incorporated into the silicon lattice (figure A.1), creating additional levels inside the band gap, changing its electric characteristics. This process is called doping. Common doping materials include group-V elements (donors), such as phosphorus, which create shallow levels close to the conduction band as shown in figure A.2 (left), adding an additional valence electron that is quasi-free, that can be easily excited, leaving the phosphorus atom as a positive ion. This material is referred to as n-type silicon, with the majority of the charge carriers being electrons. On the other hand, group-III elements (acceptors) can be used, like boron, which instead add levels close to the valence band, as shown in figure A.2 (right). The majority of the charge carriers are holes and the material is referred to as p-type silicon.

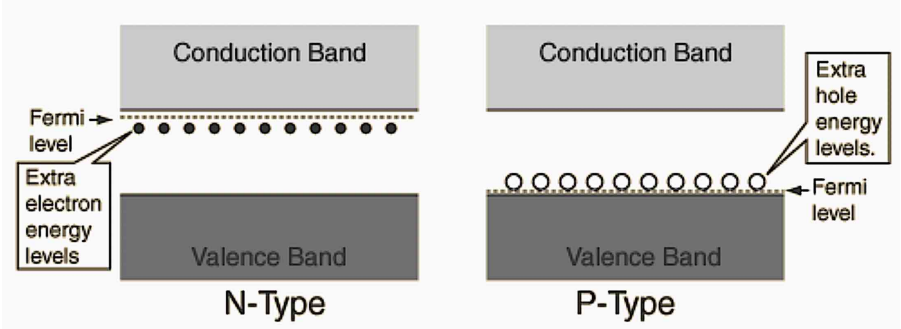

Figure A.2: Band structure modification due to silicon doping. In n-doped silicon, shallow donor levels are introduced close to the conduction band and the Fermi energy shifts up. In p-doped silicon, additional shallow acceptor levels are located close to the valence band and the Fermi energy shifts down.

This results in additional free carriers, which charge is balanced by dopant nuclei. The total sum of positive and negative charges is therefore equal. In particular, calling N_A and N_D, respectively, the acceptors and donors concentrations, the balance can be written as

$$N_D + p = N_A + n \tag{A.10}$$

Combining the equation (A.10) with the (A.6), for a p-type semiconductor, in which $p \gg n$ and $N_D = 0$, the charge carrier density can be written in terms of dopant concentration as

$$p \simeq N_A, \quad n \simeq \frac{n_i^2}{N_A}. \tag{A.11}$$

Analogously in a n-type semiconductor

$$n \simeq N_D, \quad p \simeq \frac{n_i^2}{N_D}. \tag{A.12}$$

So the semiconductor concentration of the majority charge carriers becomes approximately the same as the dopant concentration. As a consequence the current contribution of the minorities can be neglected and the charge carriers densities in the (**??**) can be replaced by the dopant density found in the equations (A.11) and (A.12), resulting in

$$\rho_{p-type} = \frac{1}{eN_A\mu_h} \tag{A.13}$$

$$\rho_{n-type} = \frac{1}{eN_D\mu_e}. \tag{A.14}$$

Also in the case of doped semiconductors the density of the free carriers is too high to make the silicon suitable as particle detector, but combining semiconductors with opposite doping, a region without free charges can be created and exploited.

A.2 The p-n junction

A.2.1 Thermal equilibrium: drift and diffusion

A p-n junction is obtained by joining together a n-type and p-type semiconductors.

At thermal equilibrium, without an applied bias voltage, the charge density, the electric field, and the voltage are shown in figure A.3.

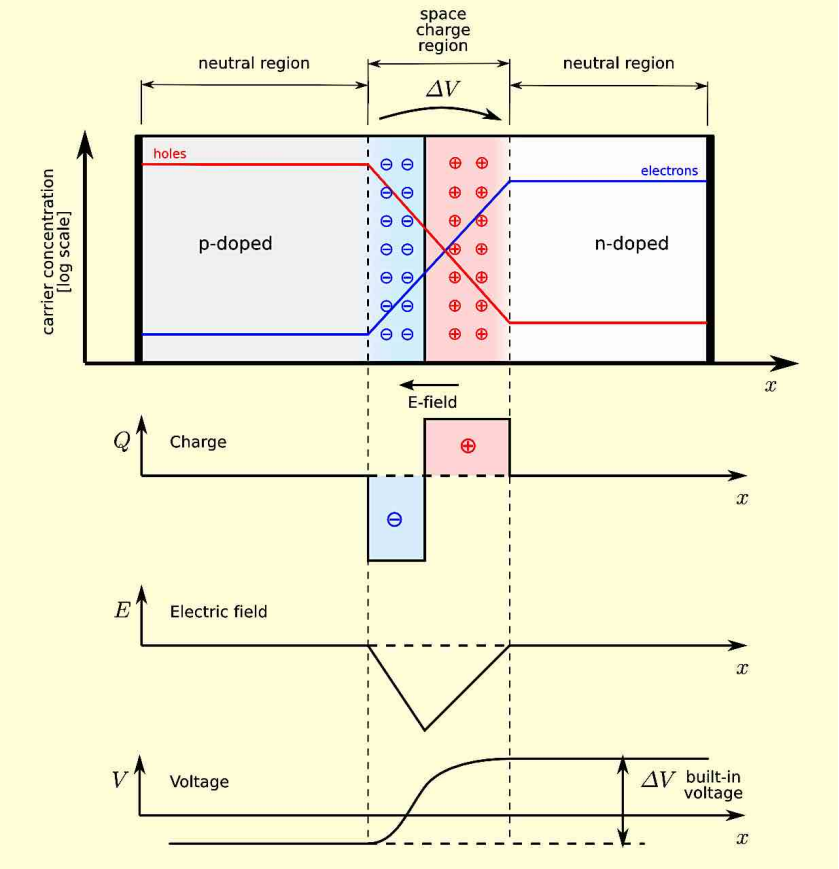

Figure A.3: A p–n junction in thermal equilibrium with no bias voltage applied: the gray regions are neutral charged regions, while the light red and blue zone are, respectively, positively and negatively charged. The plots represents, from the top, the charge density, the electric field, and the voltage.

When the p-type and n-type semiconductor are brought into contact, a diffusion movement of charge carriers takes place due to the different concentrations. Electrons move from the n-side towards the p-side and, analogously, holes move into the opposite direction. Diffusion leaves behind regions with fix charges due to acceptor and donor

ions and subsequently the initial n and p profiles are altered in the proximity of the p-n junction. The current density $\vec{J}_{p,n}$(diff) due to diffusion is

$$\vec{J}_{n,p}(diff) = \pm qD_{n,p}\frac{d\vec{n}_{n,p}}{dx} = \pm qD_{n,p}\vec{\nabla}(n,p) \tag{A.15}$$

where q is the elementary charge, $D_{n,p}$ are the diffusion constants of electrons and holes, respectively, and $\vec{\nabla}(n,p)$ are the gradients of their densities.

The diffusion proceeds until the equilibrium condition is reached. Due to this movement, electrons in the p-side recombine with the holes and the same do the holes with the electrons in the n-side, so that all the free charge carriers vanish. The resulting effect is to build up a net negative space charge on the p-side and a positive one on the n-side of the junction, creating a region where the concentration of holes and electrons is greatly suppressed and the only charges remaining are the fixed ionized donor sites and the filled acceptors. This region, without free charge carriers, is called space charge region or depletion region. This exhibits a very low conduction (high resistivity) in respect to the n-type or p-type materials on either side of the junction.

The potential difference of the accumulated space charge, the so-called built-in voltage V_0, causes an electrical field, which forces a current opposite to the diffusion. This second type of charge transport is called drift. Carriers acquire a velocity that is proportional to the electric field $\vec{E}$:

$$\vec{v}_e = -\mu_n\vec{E} \tag{A.16}$$

$$\vec{v}_h = \mu_p\vec{E} \tag{A.17}$$

being μ_n and μ_p the mobilities of electrons and holes, defined as:

$$\mu_{n,p} = \frac{q\cdot\tau_{n,p}}{m_{n,p}} \tag{A.18}$$

where m_p and m_n are the effective masses of holes and electrons and τ is the mean time interval between two scattering processes with the impurities of the material. This time interval decreases with the rising of the electric field, untill the drift velocity saturates.

Considering that the equilibrium is reached when the current produced by the electric field is equal to the one due to diffusion, it is possible to obtain the total current density for electrons and holes:

$$\vec{J}_n = \vec{J}_n(diff) + \vec{J}_n(drift) = qD_n\vec{\nabla}n - q\mu_n n\vec{E} \tag{A.19}$$

$$\vec{J}_p = \vec{J}_p(diff) + \vec{J}_p(drift) = -qD_p\vec{\nabla}n + q\mu_p p\vec{E} \tag{A.20}$$

A.2.2 Application of an external voltage

P-n junctions used in radiation detection application are worked with the application of an external voltage. This because the width of the depletion region can be modified by the application of an external voltage and large depletion regions are necessary for detecting the passage of particles crossing semiconductor-based detectors. While in equilibrium condition, the width depends only on the build-in voltage V_0 (figure A.4 (a)), which results from the initial doping concentration, when an external voltage is applied, the size of the depletion region W_d [60] is described by the equation

$$W_d = \sqrt{\frac{2\epsilon_0\epsilon_{Si}}{e}\left(\frac{N_A + N_D}{N_A N_D}(V_0 - V_{bias})\right)} \tag{A.21}$$

where V_{bias} is the applied voltage in the forward direction and ϵ_{Si} the permittivity of silicon.

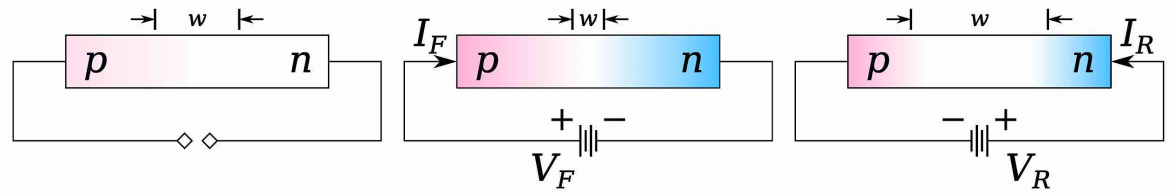

(a) Thermal-equilibrium condition. **(b)** Forward-bias condition. **(c)** Reverse-bias condition.

Figure A.4: Schematic representation of the depletion region width of a p-n junction under the three different biasing conditions.

In forward-bias condition, a positive (negative) bias voltage is applied to the p-side (n-side), the built-in voltage is reduced and the depletion zone is shrunk. In reverse-bias condition, a negative (positive) bias voltage is applied to the p-side (n-side), the built-in voltage is increased and the depletion zone is enlarged. The two different biasing conditions are shown in figure A.4 (b) and figure A.4 (c).

A semiconductor device is always operated reverse-biased to enlarge the depletion zone and with a fully depletion. The bias voltage V_{dep} required to fully deplete a sensor of given thickness d, can be found setting $W_d = d$ in the equation (A.21):

$$-V_{dep} = \frac{e}{2\epsilon_0\epsilon_{Si}}\left(\frac{N_A N_D}{N_A + N_D}\right) d^2 - V_0 \tag{A.22}$$

Appendix B

Silicon detectors

A silicon detector consists of a reverse biased p-n junction, typically formed by an heavily doped p^+ electrode connected to the negative voltage, and an heavily doped n^+ electrode, connected to the positive one. This second one is needed to allow the ohmic contact for the polarization of the device. The two electrodes are separated by a lightly doped n^- bulk, which is the active region of the detector. A sufficient reverse bias is applied to fully deplete the detector. A simple sketch of a silicon detector is shown in figure B.1.

The working principle of a silicon detector is the same of an ionization chamber: the passage of ionizing radiation through the depleted region excites electrons into the conduction band, causing the generation of electron-holes pairs, which start to drift towards the respective electrodes, following the electric field's lines. The movement of the charges induces a current on the electrodes, that gives rise to a measurable pulse, proportional to the number of pairs generated and, subsequently, to energy lost by the particle in the material. The signal stops when all charge carriers have reached their respective collection electrodes.

Compared with the other radiation detectors based on ionization in gas, semiconductor detectors have unique properties that make them very suitable for this purpose. Firstly their very low energy gap leads to the creation of a larger number of charge carriers per unit energy loss of the ionizing particle to be detected. In particular, the average energy needed to create an electron-hole pair in silicon is $\sim$ 3.6 eV, one order of magnitude smaller than the ionization energy of gases ($\sim$ 30 eV) [58]. In addition, the high material density of semiconductors ($\sim$ 2.33 g/cm^3 for silicon) leads to a large energy loss per traversed length of the ionizing particle (around 390 eV/μm for a MIP), allowing to build thin detectors that can still produce measurable signals. This higher material density does not prevent electrons and holes to move almost freely in semiconductors. This leads to a rapid ($\sim$ 10 ns) charge collection and makes these detectors really suitable in high-intensity environments. Because of these features silicon detectors are being the most used devices in a very large range of applications.

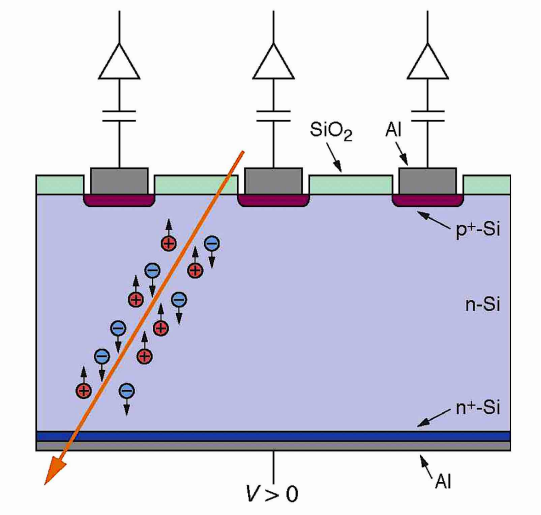

Figure B.1: Sketch of an p-on-n pad diode. When the particle passes in the material, generates electrons and holes that drift towards electrodes, giving rise to the signal.

B.1 Radiation interaction with silicon

Particle detector operating mode strongly depends on the mechanisms in which the radiation interacts with the material composing the device. When a radiation beam passes through the silicon, it may be absorbed, scattered or it may pass straight through, without any interaction. The processes of absorption and scattering can be described in terms of interactions between particles; in fact particles of the radiation flux strike atoms of the medium and are either stopped, when they lose all their energy inside it, or scattered, when they are deflected from the incident direction. The interaction results in full or partial transfer of incident radiation energy to electrons or nuclei of constituent atoms, or to charged particle products of nuclear reactions.

Radiations can be classified in directly and indirectly ionizing beam. Charged particles (such as fast electrons and heavy particles), for which energy loss can occur gradually, and uncharged radiations (like photons or neutrons), that lose all their energy in a single collision, are examples of the first and the second group, respectively. In order to understand how to use silicon as a detector material, in the following paragraphs, the phenomena at the base of the passage of particles through matter are reported.

B.1.1 Heavy charged particles

When an heavy-charged particle ($Mc^2 >> m_e c^2$) enters in a material with a velocity $v = \beta c$, it interacts with the atoms of the medium through Coulomb scatterings with

the orbital electrons, loosing part of its energy. This energy can cause excitation, i.e. displacement of the electrons to higher energy levels and, in the case of an high energy loss, also ionization. The electrons released in the process can in some cases give rise to subsequent secondary ionizations (δ rays) closed to the primary track.

The maximum energy (W_{max}) that a charged particle of mass M can lose in a single collision is

$$W_{max} = \frac{2m_e\beta^2c^2\gamma^2}{1 + \frac{2\gamma m_e}{M} + \left(\frac{m_e}{M}\right)^2} \tag{B.1}$$

that for M>>2m$_e\gamma$ becomes

$$W_{max} \simeq 2m_e\beta^2c^2\gamma^2. \tag{B.2}$$

Since this value is much lower than the typical energy of an incident particle, the loss of energy happens in different steps, during which the particle velocity subsequently decreases its velocity, until it stops or escapes from the material.

The mean energy loss of charged particles with a mass M>m$_\mu$ for unit path length and unity density, called mass stopping power, can be well described by the Bethe-Bloch formula:

$$\left\langle -\frac{dE}{dx} \right\rangle \frac{1}{\rho} = Kz^2\frac{Z}{A}\frac{1}{\beta^2}\left(\frac{1}{2}\ln\frac{2m_ec^2\beta^2\gamma^2W_{max}}{I^2} - \beta^2 - \frac{\delta(\beta\gamma)}{2}\right)[MeVcm^2/g] \tag{B.3}$$

where K = 4πN$_A$r$_e^2$m$_e$c^2 with N$_A$ is the Avogadro's number, r$_e$ is the classical electron radius and, m$_e$c^2 is the rest mass of the electron, Z is the atomic number, A is the atomic mass, I is the mean ionization energy of the medium. γ is the Lorentz factor of the incident charged particle and β, its velocity. This formula is valid in the range $0.1 < \beta\gamma < 1000$; outside these values, other forces (weak and strong) overcome the electromagnetic interaction. The behaviour of the mass stopping power is shown in figure B.2 for positive muons.

As visible, from the plot, at low energy the curve is governed by a factor $1/\beta^2$, in addition at very lower energies also shell corrections must be taken into account, given by the fact that the particle velocity becomes comparable to orbital velocity of the bound electron and so, the assumption that the electron is stationary with respect to the incident particle is no longer valid. While at higher energies the curve is characterized by a logarithmic rise and for these values ($\beta\gamma$ >4) radiative effects begin to be important. In this range, two independent mechanisms have to be taken into account; the rise due to the relativistic flattening and extension of the particle's electric field and the density correction $\delta(\beta\gamma)$ which, on the contrary, partially cancel the rise at high energies because, rather than producing ionization at greater distances, the field polarizes the medium along the particle's path and shielding the long-range interactions. A minimum

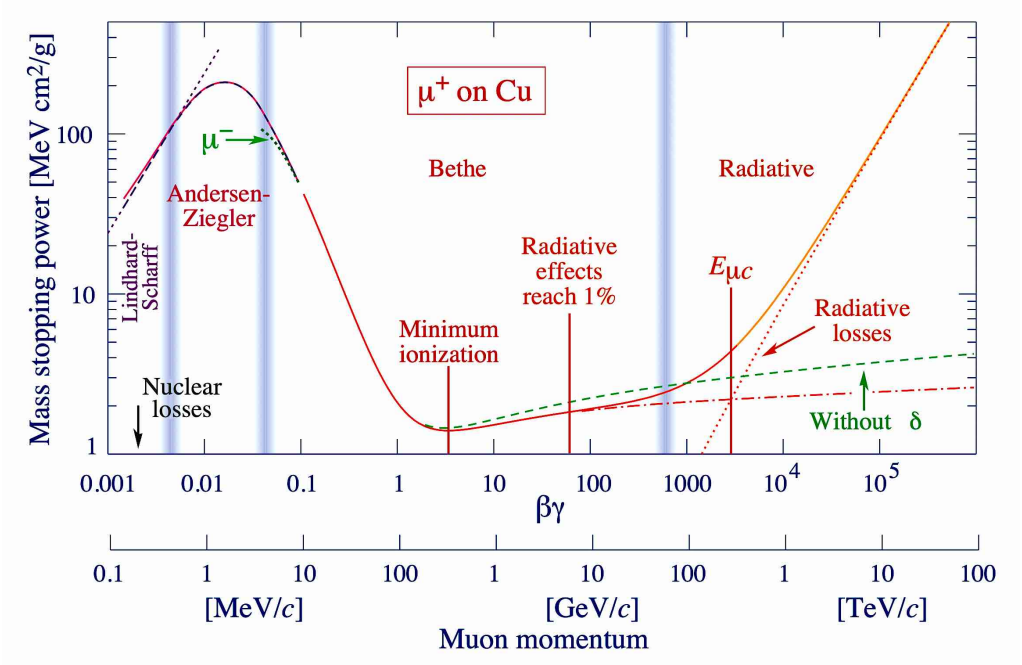

Figure B.2: Mass stopping power for positive muons in copper as a function of $\beta\gamma = p/Mc$. Solid curves indicate the total stopping power. Data below the break at $\beta\gamma \sim 0.1$ are taken from [62] assuming only β dependence, and data at higher energies are from [63]. Vertical bands indicate boundaries between different approximations discussed in the text. The short dotted lines labeled μ^- illustrate the dependence of stopping power on projectile charge at very low energies, called Barkas effect [64]. Conversion from $\beta\gamma$ to momentum is reported below the plot.

,

is reached at $\beta\gamma \sim$ 3-4. This value is almost the same for different materials, if we consider particles with the same charge. A particle whose energy loss is at the minimum of the Bethe-Bloch function is referred to as Minimum Ionizing Particle (MIP). These particles lose a small fraction of their energy traveling through the material and can be considered MIP during all the interaction. Their avarage stopping power in silicon is of about 1.66 MeV·cm^2/g.

Considering that the energy lost by particle passing through the material gets invested in creating electron-hole pairs, and that the mean energy needed to remove one electron from the atom creating a pair is a property of the material, being for the silicon $W_{Si} \sim$ 3.6 eV at room temperature, it is possible to obtain the number of pairs generated:

$$n = \frac{\Delta E}{W_{Si}} \tag{B.4}$$

where the energy ΔE can be obtained multiplying the (B.3) for the thickness and the density of the detector. It follows that a MIP creates $\sim 1.1 \cdot 10^2$ pairs per μm of traversed silicon.

B.1.2 Electrons and positrons

Like other charged particles, electrons and positrons lose energy via ionization due to Coulomb interaction with the orbital electrons. However in this case, because of their small masses, equal to the ones of the orbital electrons, the interaction causes a greater amount of energy loss and a bigger deviation in respect to their original path, so that the approximation of the charged particles to be undeflected is no longer valid. In addition, for electrons the collisions are in this case between identical particles and so, also indistinguishability must be taken into account. For these reasons the Bethe-Bloch (B.3) formula takes the form of

$$\left\langle -\frac{dE}{dx} \right\rangle = K\frac{Z}{A}\frac{1}{\beta^2}\left(\ln\frac{m_e c^2\beta^2\gamma^2 W_{max}}{2I^2} + f(\gamma)\right) \tag{B.5}$$

Where $f(\gamma)$ is a function that depends on the velocity of the electrons and positrons.

Differently from heavy-charged particles, for the electrons, due to the small mass, also electromagnetic radiation (Bremsstrahlung) arising from the interaction with the Coulomb field of a nucleus and the subsequent curvature of the electron trajectory and the emission of a photon, must be taken into account:

$$-\frac{dE}{dx} \propto z^2\frac{Z^2}{A}\ln\frac{183}{Z^{1/3}}\frac{E}{m^2}. \tag{B.6}$$

Due to the proportionality to the term $\frac{E}{m^2}$, the energy loss by Bremsstrahlung is relevant only for particles with a small mass, like electrons and positrons, or for ultra-relativistic energy particles with an intermediate mass, like muons.

In the formula, also the quadratic dependence on Z^2 appears indicating that the radiative energy loss is more significant in materials with an high atomic number. For this reason, it is usually introduced a quantity that depends on the material, called radiation length X_0 (g/cm^2), defined as the distance over which the particle loses 1/e ($\sim$ 37%) of its energy, so that the radiative term can be written as

$$-\left(\frac{dE}{dx}\right)_{brem} \propto \frac{E}{X_0} \tag{B.7}$$

where E is the energy of the incident particle.

The total energy loss for electrons is then the sum of two contributions:

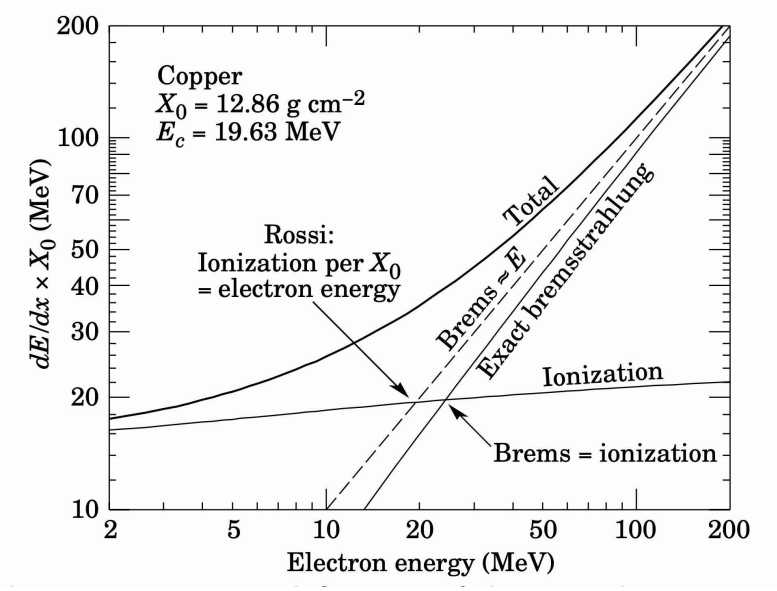

Figure B.3: Fractional energy loss per radiation length in copper as a function of electron energy. Ionization and Bremsstrahlung energy loss are plotted, together with the total one. The energy value in which the lines corresponding to the two mechanisms cross each other is called critical energy.

$$\frac{dE}{dx} = \left(\frac{dE}{dx}\right)_{ion} + \left(\frac{dE}{dx}\right)_{brem}. \tag{B.8}$$

The value of the energy for which the two terms are equal, is called critical energy (E_c), and in solids it is approximately

$$E_c \sim \frac{(610)MeV}{Z + 1.24} \tag{B.9}$$

resulting around 40 MeV in silicon (Z = 14).

As shown in figure B.3, when the energy is below this value, ionization energy loss dominates, while radiative loss for the electrons becomes significant when the energies increase over the critical energy value.

B.1.3 Photons

The behavior of photons in matter is completely different from that of charged particles. In fact the photon's lack of an electric charge makes impossible inelastic collisions with atomic electrons. Indeed, photons lose all their energy inside the material, giving rise to a secondary charged particle.

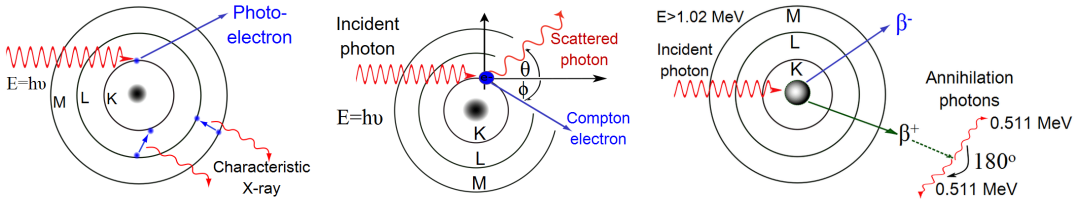

Figure B.4: From the left: illustration of photoelectric effect, Compton scattering and pair production.

In particular, depending on its energy the photon can interacts through three different mechanisms (figure B.4): photoelectric effect, Compton scattering and pair production.

Photoelectric effect

Photoelectric effect is dominant for low energies, in the range 500 KeV $<$ E_γ $<$ ionization energy. The photon is absorbed by a bounded atom of the material, disappearing and giving as products the atomic nucleus recoils, which conserves the momentum and a photo-electron with energy

$$E = h\nu - E_{binding} \tag{B.10}$$

With hν the photon energy and $E_{binding}$ the binding energy of the electron. The cross-section is

$$\sigma_{p.e.} \propto \frac{Z^{4-5}}{h\nu^{3.5}} \tag{B.11}$$

Compton scattering

Compton scattering happens for energies $E_\gamma \sim 1$ MeV. It is the only process in which the photon doesn't disappear at the end of the interaction. In particular, it is scattered and deviated from the original direction of an angle θ. Considering hν and hν' the energy of the photon before and after the collision

$$\frac{h\nu'}{h\nu} = \frac{1}{1 + h\nu(1 - cos\theta)} \tag{B.12}$$

And the cross-section results

$$\sigma_{Compton} \propto Z \tag{B.13}$$

Pair production

Pair production is dominant for higher energies and, in particular, since it consists on the transformation of a photon into an electron-positron pair, it has a threshold given by

$$h\nu > 2m_e c^2 \sim 1.022 MeV \tag{B.14}$$

The emitted positron quickly annihilate into two new photons. The cross-section is

$$\sigma_{nuc} \propto Z^2 \tag{B.15}$$

As a consequence of such kind of interactions, a photon interacting with a target disappears completely from the incident beam. Moreover, due to the smallest cross section of all this kind of reactions, *gamma*-ray are much more penetrating than charged particles. The attenuation of the incident beam is exponential with the thickness of the absorbing medium:

$$I(x) = I_0 e^{-x\mu_l} \tag{B.16}$$

where μ_l is the linear attenuation coefficient, I_0 is the incident beam intensity and x is the thickness. As a consequence, the total cross section can be written as

$$\sigma_{tot} = \frac{\mu_l}{\eta} \tag{B.17}$$

where η is the number of atoms per unit of mass. The total cross section, with the different components, is shown in figure B.5.

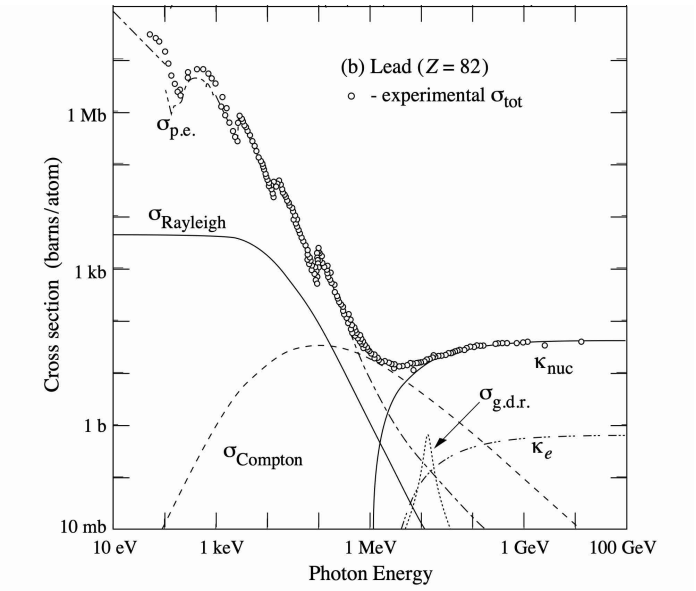

Figure B.5: Photon total cross sections as a function of energy in carbon and lead, showing the contributions of different processes [65].

B.2 Signal formation

Silicon sensors, as radiation detectors, use the depletion zone at the junction as the active detection region. As seen before, charged particles transfer their energy to matter, inducing excitation or ionization of the atoms and thus creating electron-hole pairs. In an undepleted silicon sensors these charge carriers would recombine, preventing the collection by the respective electrodes. Electron-hole pairs created in the depletion zone, instead, do not recombine and if an external reverse-bias voltage is applied, they drift towards the cathode and the anode (figure B.1). The movement of the positive and negative charges induces a current on the electrodes, producing a measurable signal [66, 67].

The instantaneous current and the charge Q induced on a given electrode by n carriers with charge q with a velocity $\vec{v}$ are predicted by the Shockley-Ramo theorem [68, 69, 70]:

$$i(t) = -(nq)\vec{v} \cdot \vec{E}_w(x) \tag{B.18}$$

$$Q = -qV_w(x) \tag{B.19}$$

where $\vec{E}_w(x)$ and $V_w(x)$ are, respectively, the weighting field and weighting potential, namely the electric potential and field that in an instantaneous position x, given a unitary voltage on the electrode for which the induced charge is calculated and null voltage on the other.

Considering, for example, a parallel plate detector with two infinite plates, separated by a distance d, the weighting field results:

$$\vec{E}_w(x) = -\frac{1}{d}\vec{e}_x \tag{B.20}$$

Where $\vec{e}_x$ is the unitary vector along the x direction.

The induction, and subsequently, the signal, stops when all the carriers reach the collecting electrodes. The pulse is then fully developed. Calling t_c the charge collection time, that, for silicon, is of the order of ns, the total collected charge results in the end:

$$Q = \int_0^{t_c} i(t)dt \tag{B.21}$$

Bibliography

[1] ALICE Collaboration, K. Aamodt et al., "The ALICE experiment at the CERN LHC", JINST 3 (2008) S08002.

[2] arXiv:1812.06772v2 [hep-ph] 25 Feb 2019

[3] A next-generation LHC heavy-ion experiment, D. Adamová et al., arXiv:1902.01211

[4] A. Andronic et al. Eur. Phys. J. C76 (2016) no. 3, 107, arXiv:1506.03981 [nucl-ex].

[5] A. Beraudo et al. arXiv:1803.03824 [nucl-th].

[6] R. J. Fries, V. Greco, and P. Sorensen Ann.Rev.Nucl.Part.Sci. 58 (2008) 177–205, arXiv:0807.4939 [nucl-th].

[7] ALICE Collaboration, S. Acharya et al. JHEP 04 (2018) 108, arXiv:1712.09581 [nucl-ex].

[8] S.Plumari, V.Minissale, S.K.Das,G.Coci, and V.GrecoEur.Phys.J.C78(2018) no.4,348,arXiv:1712.00730 [hep-ph].

[9] A.Andronic,P.Braun-Munzinger,K.Redlich,andJ.StachelPhys.Lett.B659(2008)149–155,arXiv:0708.1488 [nucl-th].

[10] J. Zhao, H. He, and P. Zhuang, "Searching for Ξ_{cc} in Relativistic Heavy Ion Collisions," Phys. Lett., vol. B771, pp. 349–353, 2017.

[11] H. He, Y. Liu, and P. Zhuang, "Ω_{ccc} production in high energy nuclear collisions," Phys. Lett., vol. B746, pp. 59–63, 2015.

[12] R. Aaij et al., "Observation of the doubly charmed baryon Ξ_{++}," Phys. Rev. cc Lett., vol. 119, p. 112001, Sep 2017

[13] ALICE Collaboration, B. Abelev et al. Phys. Rev. Lett. 109 (2012) 072301, arXiv:1202.1383 [hep-ex].

[14] ALICE Collaboration, J. Adam et al. Phys. Lett. B766 (2017) 212–224, arXiv:1606.08197 [nucl-ex].

[15] P. Braun-Munzinger and J. Stachel, "(Non)thermal aspects of charmonium production and a new look at J/Ψ suppression," Phys. Lett., vol. B490, pp. 196–202, 2000.

[16] R. L. Thews, M. Schroedter, and J. Rafelski, "Enhanced J/Ψ production in deconfined quark matter," Phys. Rev., vol. C63, p. 054905, 2001.

[17] https://arxiv.org/pdf/1304.2309.pdf figure10

[18] J. Adam et al., "Direct photon production in Pb-Pb collisions at $\sqrt{s_{NN}} = 2.76$ TeV," Phys. Lett., vol. B754, pp. 235–248, 2016.

[19] V. Lysov, S. Pasterski, and A. Strominger, "Low's Subleading Soft Theorem as a Symmetry of QED," Phys. Rev. Lett., vol. 113, no. 11, p. 111601, 2014.

[20] F. Bloch and A. Nordsieck, "Note on the Radiation Field of the electron," Phys. Rev., vol. 52, pp. 54–59, 1937.

[21] F.E.Low,"Bremsstrahlung of very low-energy quanta in elementaryparticle collisions," Phys. Rev., vol. 110, pp. 974–977, 1958.

[22] V. Monaco et al., JINST 12 (2017) C12056 doi:https://doi.org/10.1088/1748-0221/12/12/C12056.

[23] R. Sacchi et al. Med. Phys., 42 (2015) 3581-3582, doi: https: //doi.org/10.1118/1.4925480.

[24] N. Cartiglia et al., NIM A 924 (2019) 350-354. doi: https://doi.org/10.1016/j.nima.2018.09.157

[25] https://doi.org/10.1088/1361-6560/ab7b2d

[26] P. Gasik at al. Nuclear Physics A 982 (2019) 943–946

[27] T. Kugathasanet al., Nucl. Inst. Meth. A Vol. 979, Nov. 2020, https://doi.org/10.1016/j.nima.2020.164461

[28] L. Pancheri et al., IEEE Tran. Electron Dev., Vol. 67, No. 6, June 2020. doi: 10.1109/TED.2020.2985639

[29] W. Snoeys et al., NIM A 871 (2017) 90 – 96. doi:https://doi.org/10.1016/j.nima.2017.07.046

[30] H. F. W. Sadrozinski, A. Seiden, and N. Cartiglia. 4-Dimensional Tracking with Ultra-Fast Silicon Detectors. 2017. arXiv: 1704.08666 [physics.ins-det].

[31] A. G. Chynoweth, Phys. Rev. 109, 1537 (1958).

[32] P. Fernandez-Martinez, D. Flores, S. Hidalgo, V. Greco, A. Merlos, G. Pellegrini, D. Quirion, "Design and Fabrication of an Optimum Peripheral Region for Low Gain Avalanche Detectors", Nucl. Instrum. Methods Phys. Res. A 821, pp. 93–100, 2016, DOI: 10.1016/j.nima.2016.03.049.

[33] H. F. W. Sadrozinski, A. Seiden, and N. Cartiglia, "4-Dimensional Tracking with Ultra-Fast Silicon Detectors, 2017," arXiv:1704.08666 [physics.ins-det].

[34] Hartmut F-W Sadrozinski et al 2018 Rep. Prog. Phys. 81 026101

[35] Landau noise contribution to the time resolution as a function of the CFD value for different detector thicknesses.

[36] M. Noy, "The GigaTracker", RD50 workshop, Torino, June 2016, https://agenda.infn.it/conferenceDisplay.py?confId=11109

[37] arXiv:1705.08830 [physics.acc-ph]

[38] R. Yohay, Precision timing for the high luminosity upgrade of CMS, in: PoS 028, Pixel, 2017, URL https://pos.sissa.it/309/028/pdf.

[39] S.J. Hong, et al., SiPM-PET with a short optical fiber bundle for simultaneous PET-MR imaging, Physics in Medicine and Biology 57 (2012) 3869–3883.

[40] R. Sacchi et al. Med. Phys., 42 (2015) 3581-3582, doi: https://doi.org/10.1118/1.4925480.

[41] Krimmer, J. et al. NIM A, 878 (2018) 58–73 doi:10.1016/j.nima.2017.07.063.

[42] Golnik, F. et al. Phys. Med. Biol.,59 (2014) 5399–5422 doi: 10.1088/0031-9155/59/18/5399

[43] S. Marcatili, J. et al. Phys. Med. Biol., (2020) doi: 10.1088/1361-6560/ab7a6c

[44] https://wikihost.nscl.msu.edu/protondetector/lib/exe/fetch.php?media=n1470_-rev19.pdf

[45] https://download.tek.com/manual/6487-901-01(B-Mar2011)(Ref).pdf

[46] LabVIEWTM User Manual, National Instruments, 2003.

[47] arXiv:1605.01692v1 [physics.ins-det] 4 May 2016

[48] https://www.keysight.com/it/en/assets/7018-04256/data-sheets/5991-3890.pdf

[49] https://contentnktphotonics.s3-eu-central-1.amazonaws.com/Datasheets/PILAS/ALS_Pilas_DX.pdf?1632838010

[50] https://pdf.directindustry.com/pdf/standa/manual-translation-rotation-stages/35170-558253.html

[51] https://docs.rs-online.com/035e/0900766b8127e31c.pdf

[52] https://cividec.at/electronics-C2-HV.html

[53] https://datasheetspdf.com/pdf-file/64399/Mini-Circuits/LEE-39/1

[54] https://datasheetspdf.com/pdf-file/590418/Mini-Circuits/GALI5/1

[55] https://eu.mouser.com/datasheet/2/400/z_plus_e_low_voltage_10v_to_100v-2581128.pdf

[56] https://doi.org/10.1016/j.nima.2020.164379

[57] McDonald W.J. Gedcke D.A. Design of the constant fraction of pulse height trigger for optimum time resolution. Nuc. Inst. and Meth., 58:253–260, 1968.

[58] G. Lutz. Semiconductor Radiation Detectors: Device Physics. Springer Berlin Heidelberg, 2007. ISBN 978-3-540-71678-5

[59] Fabjan C.W. and Herwig S. Particle Physics Reference Library, Volume 2: Detectors for Particles and Radiation. Springer, Gewerbestrasse 11, 6330 Cham, Switzerland, 2020.

[60] S. M. Sze and M.-K. Lee. Semiconductor Devices: Physics and Technology. John Wiley Sons, New York, 3rd edition, 2012. ISBN 978-0470-53794-7.

[61] P.A. Zyla et al. Particle Data Group. 2020.

[62] Stopping Powers and Ranges for Protons and Alpha Particles, ICRU Report No. 49 (1993);

[63] D.E. Groom, N.V. Mokhov, and S.I. Striganov, Muon stopping-power and range tables: 10 MeV–100 TeV, Atomic Data and Nuclear Data Tables 78, 183–356 (2001).

[64] W. H. Barkas, W. Birnbaum and F. M. Smith, Phys. Rev. 101, 778 (1956).

[65] Data from J.H. Hubbell, H. Gimm, and I. overbo, J. Phys. Chem. Ref. Data 9, 1023 (1980); parameters for g.d.r. from A. Veyssiere et al., Nucl. Phys. A159, 561 (1970).

[66] G. F. Knoll, Radiation Detection and Measurement, 3rd ed. John Wiley and Sons, New York, 2000. http://www.slac.stanford.edu/ spires/find/books/www?cl=QCD915:K55:2000.

[67] W. Shockley, "Currents to conductors induced by a moving point charge," Journal of Applied Physics 9 no. 10, (1938) 635–636. http://dx.doi.org/10.1063/1.1710367.

[68] Z. He, "Review of the Shockley-Ramo theorem and its application in semiconductor gamma-ray detectors," Nuclear Instruments and Methods in Physics Research Section A 463 no. 1, (2001) 250 – 267. http://www.sciencedirect.com/science/article/pii/ S0168900201002236.

[69] J. C. W. Song and L. S. Levitov, "Shockley-ramo theorem and long-range photocurrent response in gapless materials," Phys. Rev. B 90 (Aug, 2014) 075415. https://link.aps.org/doi/10.1103/PhysRevB.90.075415.

[70] A. Alberigi Quaranta, M. Martini, and G. Ottaviani, "The pulse shape and the timing problem in solid state detectors - a review paper," IEEE Trans. Nucl. Sci. 16N2 (1969) 35–61.